Modeling the effect of dissolved gas on the bubble layer along a vertical gas-evolving electrode

I.R.C. Krikke

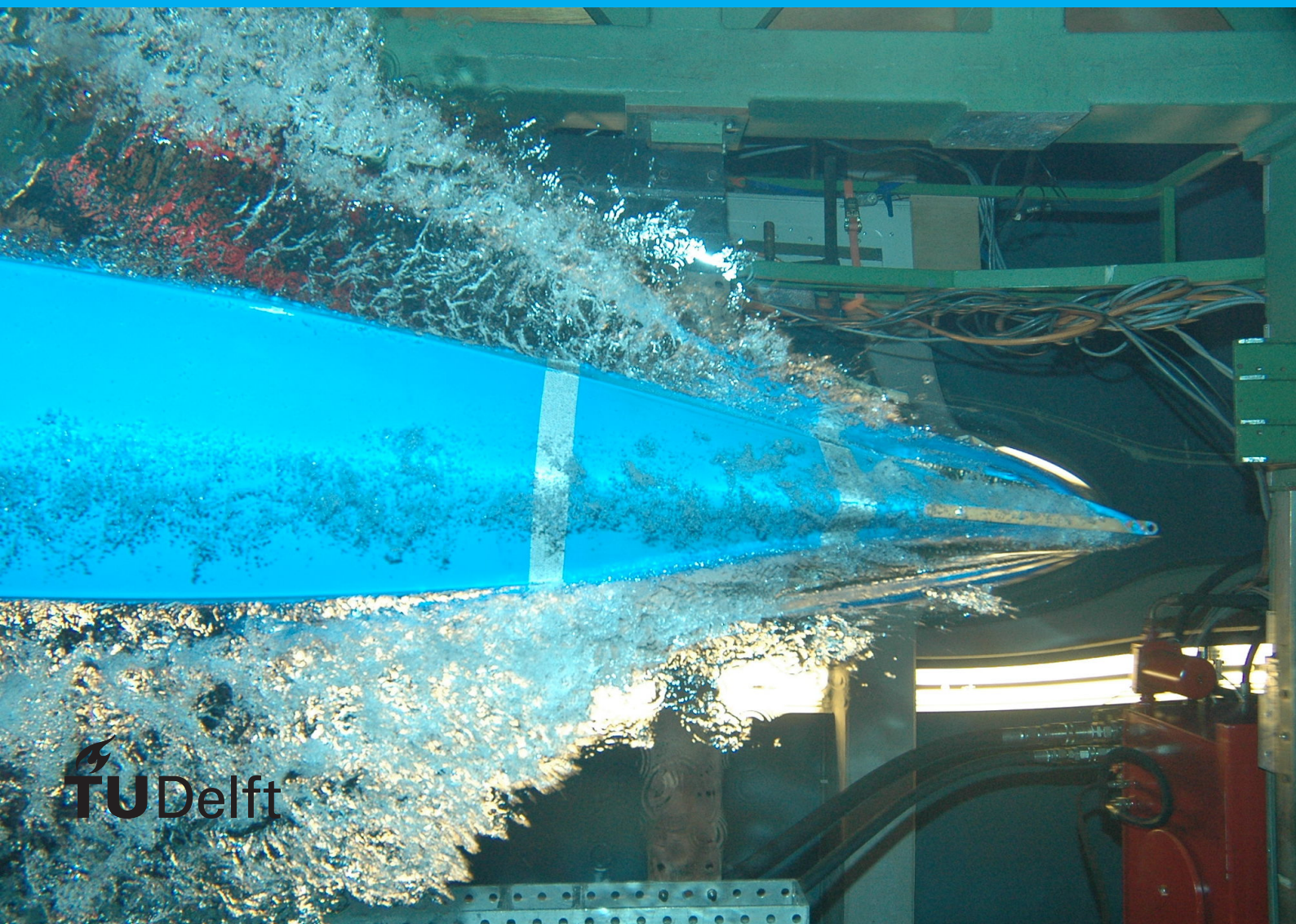

Modeling the effect of dissolved gas on the bubble layer along a vertical gas-evolving electrode

by

I.R.C. Krikke

to obtain the degree of Master of Science
at the Delft University of Technology,
to be defended publicly on Friday October 15, 2021 at 10:00 AM.

Student number:	4169034	
Project duration:	August 15, 2020 – October 15, 2021	
Thesis committee:	Dr. ir. J.W. Haverkort„	TU Delft, supervisor
	Dr. ir. W. P. Breugem,	TU Delft
	Dr. ir. L. Botto,	TU Delft

TU Delft

Abstract

During water electrolysis for the production of hydrogen and oxygen, many bubbles are formed at the electrodes. The presence of these bubbles causes a number of side effects such as a significant increase in the total cell resistance (e.g., electrical circuit resistances, transport related resistances, and electrochemical reaction resistances). The efficiency of water electrolysis is therefore closely related to the presence of bubbles in the electrolyte.

In this work, the focus is on the numerical modeling of the evolution of the bubble layer in a vertical channel with gas-evolving electrodes on either side of the channel. One of the problems is the growth of rising bubbles along the electrode, which affects the shape and thickness of the bubble layer. This bubble growth depends on four main phenomena, e.g., bubble coalescence, change in hydrostatic pressure, presence of water vapor, and mass transfer of dissolved gas. Of these, the mass transfer of dissolved gas contributes the most to bubble growth. Accounting for this growth can be crucial to the computational effort to accurately simulate the bubble plume shape and thickness.

By coupling a multi-phase flow model to the transport of dilute species, the bubble layer could be simulated. The simulation results were compared with experimental data, which showed that including mass transfer in the simulations could accurately simulate the bubble layer (in shape and thickness) over a wide range of different operating conditions.

Contents

Nomenclature

Chemical and dimensionless symbols

HO^-	Hydroxide
H_2	Hydrogen
KOH	Potassium hydroxide
O_2	Oxygen
Re	Reynolds number
Sc	Schmidt number
Sh	Sherwood number

List of common symbols

α	Volume fraction gas
δ_b	Bubble layer thickness
δ_N	Nernst diffusion layer thickness
$\dot{\gamma}$	Shear rate
$\mathbf{F}$	Volume force
$\mathbf{g}$	Gravity vector
$\mathbf{U}$	Superficial velocity
$\mathbf{u}$	Interstitial velocity
$\mathbf{U}_r$	Relative velocity gas phase
μ	Dynamic viscosity
ν	Kinematic viscosity
ρ	Density
τ	Shear stress
a	Interfacial area per volume
b	Molality of the salt
C_∞	Concentration in the bulk
C_{lift}	Lift coefficient
C_b	Gas-liquid interfacial concentration
C_D	Drag coefficient
C_e	Concentration at electrode surface
C_s	Saturation concentration

D	Diffusion coefficient
F	Faraday's constant
f_G	gas evolution efficiency
F_x	Force acting on bubble in the x-direction
F_y	Force acting on bubble in the y-direction
H_0	Henry's constant for pure water
H_{Salt}	Henry's constant for salt solution
I	Current
j	Current density
k	Mass transfer coefficient
k_{Salt}	Constant of Sechenov
M	Molecular weight
M_{lg}	Mass transfer rate
n	Number of moles
N_D	Total dissolved gas flux
N_E	Flux towards the bulk
N_G	Gaseous phase at the electrode
P	Pressure
R	Resistance
$R_{\mathrm{universal}}$	Gas constant
R_b	Bubble radius
T	Temperature
U	Voltage
V	Volume

Subscripts

g	Gas
$Hdiff$	Hydrodynamic self-diffusion
i	Species
l	Liquid
$Saff$	Saffman's lift velocity
$Sdiff$	Shear-induced diffusion
$Smig$	Shear-induced migration
$Stokes$	Stokes' flux

1 Introduction

1.1. Introduction

The consumption of fossil fuels is responsible for the emissions of harmful greenhouse gases linked to global climate change. Also, global oil and gas reserves will be exhausted by the middle of the 21st century. This will lead to scarcity and jeopardize future energy needs. A more desirable scenario is to keep these reserves in the ground, which prevents unnecessary emissions of harmful greenhouse gases. Therefore, dependence on fossil fuels is not sustainable. Since scientific and public awareness of these problems has increased, political debate and policy-making has shifted and moved to a more sustainable way to satisfy the energy demands, e.g., the European Union has adopted a new climate and energy plan which includes delivering a minimum of 27% share of renewable energy consumption by 2030 [9]. An agreement has been reached that a clean sustainable and renewable resource based energy system is needed. However, the transition to renewable energy sources, especially the ones dedicated to electric generation (i.e., wind and solar energy) gives rise to new challenges. A few of these challenges are storing and utilization of surplus energy, energy supply reliability and location specificity. Hydrogen production systems can help to overcome these challenges. Since converting renewable electrical energy into hydrogen via water electrolysis is a potential option. Hydrogen is a clean energy carrier, the most abundant element in the universe, has the highest energy per unit mass and can be easily stored. Therefore, hydrogen is considered one of the best alternatives to fossil fuels to ensure global stability and sustainability. Hydrogen production is often limited to small-scale operations. However, efforts are being made to improve the efficiency of water electrolysis.

1.2. Problem statement

Hydrogen is being produced from various renewable and non-renewable energy resources. Currently, 96% of the global hydrogen production comes from non-renewable energy resources (e.g., steam reforming of methane, oil reforming, and coal gasification) [38]. The usage of these fossil fuels produces low purity hydrogen along with high concentrations of harmful greenhouse gases [15]. An environmentally friendly way to produce hydrogen is via water electrolysis. Hydrogen produced by electrolysis has a few advantages such as high purity and simplicity of the system. Currently, only 4% of global hydrogen is produced by the electrolysis of water [27]. Reducing capital and operating costs is key to the widespread use of water electrolysis. However, improvements are required regarding the efficiency of water electrolysis. There are several resistance barriers in water electrolysis causing low efficiencies (e.g., electrical circuit resistances, transport related resistances, and electrochemical reaction resistances). Transport related resistances are significant in alkaline electrolyzers forcing it to operate at relatively low current density. There are two main reasons why resistance occurs. First, the

formation of hydrogen gas bubbles and oxygen gas bubbles in the electrolyte, which causes the electric resistance in the electrolyte to increase. Operating at higher current densities will only exacerbate this effect. The second effect is the growing bubbles on the surface of the electrode. These bubbles will screen off reactants that require to be transported to the electrodes. This effect is also known as bubble screening and will decrease the active area of the electrode [3]. Although the screening layer is fairly small, the effect it has on the efficiency of water electrolysis is notable. To reduce these negative effects of the bubbles on the energy efficiency, several process intensification methods have been developed and are listed below:

- Ultrasound [62].
- Lorentz force [64].
- Centrifugal force [8].
- Forced electrolyte flow [34].

These process intensification methods will intensify multiphase separation. The common denominator of these processes is the reduction of the average bubble residence time. To understand the impact of the bubbles on the performance of the electrolyzer, these intensification techniques are studied.

1.3. Research questions

The following research questions have been developed:

- Is the electrolyte in the vicinity of the electrode supersaturated with dissolved gas? If so, how far does this supersaturation extend, and to what degree?
- Will the bubble continue to grow once released from the electrode? If so, how much growth can be expected once it is released?
- How does bubble growth affect the shape of the bubble plume?
- Does the size of the bubble affect the position of the bubble relative to the electrode?

1.4. Document structure

This thesis consists of six chapters. The first chapter is the introduction, in which the problem statement and the research questions are discussed. The following chapters are structured as follows:

- Chapter 2 contains the basic principles of water electrolysis, the mass transfer of dissolved gas and the influence of bubbles in the electrolyte. Also the numerical models will be discussed.
- Chapter 3 describes the models used, including the computational geometries, the assumptions made, and a comparison between the different models are made.
- Chapter 4 presents and analyzes the results of the project, these results are then compared with the experimental data available.
- Chapter 5 sums up the main conclusions of the study.
- Chapter 6 several recommendations are made.

2

Theory

2.1. Fundamentals of water electrolysis

Water electrolysis is an electrochemical process used to split water molecules into hydrogen gas and oxygen gas. The basic water electrolysis unit includes an anode, a cathode, a diaphragm, a power supply and an electrolyte, as illustrated in figure 2.1.

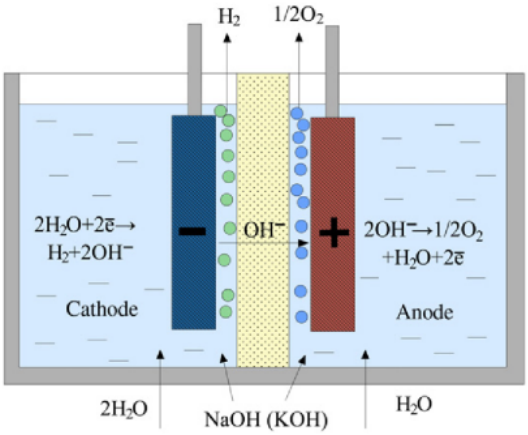

Figure 2.1: Schematic diagram of a traditional alkaline electrolysis cell [33]. The yellow region between the electrode is the diaphragm. Nowadays the zero gap cell design (no gap between the electrodes and the separator) is chosen over the traditional design [39].

The electrodes are generally made from nickel based alloys, which are low in cost, have a good electric conductivity and have high catalytic activity [21]. The electrodes are immersed in an electrolyte. An electrolyte is a substance that, when dissolved in a solvent, allows the conduction of ions. In alkaline electrolyzers, potassium hydroxide solution is mainly used with water as a solvent. Between the electrodes, a diaphragm is placed. A diaphragm is a micro-porous material with the average pore sizes of less than 1 µm, allowing the transport of water, dissolved species, ions between the anode and the cathode compartments, and the separation of gases [11]. Both electrodes are connected to an external power supply. In order for the reaction to take place a potential difference between the two electrodes is required. When operating, hydroxide ions are formed at the cathode by the reduction of liquid water into gaseous hydrogen, as stated by equation (2.1). The hydroxyl ions migrate through the electrolyte towards the anode where they are oxidized into oxygen and water, as shown in equation (2.2).

$$\text{Cathode}: 2H_2O(l) + 2e^- \rightleftharpoons 2H_{2(g)} + 2OH^- \tag{2.1}$$

$$\text{Anode} : 2\text{OH}^- \rightleftharpoons \frac{1}{2}\text{O}_2(g) + \text{H}_2\text{O}(l) + 2\text{e}^- \tag{2.2}$$

The overall reaction of the alkaline electrolysis cell is shown in equation (2.3).

$$\text{Overall reaction} : 2\text{H}_2\text{O(l)} \rightleftharpoons O_2(g) + 2\text{H}_2(g) \tag{2.3}$$

2.1.1. Cell configuration

The efficiency of water electrolysis is closely related to the presence of bubbles in the electrolyte. In industrial applications, gas generating electrodes are therefore oriented in a vertical position, this will prevent the accumulation of bubbles. The formation of bubbles causes multiple side effects. First, the bubbles accelerate the electrolyte flow in the vicinity of the electrode, which improves the mass transport of dissolved gas. Second, bubbles act as moving electrical insulators, affecting the current density distribution and increasing the resistance across the electrolyzer [19]. To mitigate this side effect, several cell designs have been developed that allow efficient removal of gas bubbles [25]. Another way to reduce the gas fraction is to increase the pressure or circulate the electrolyte. The latter option is used in most industrial electrolyzers, shown in figure 2.2a. However, circulating the electrolyte in industrial applications is used to dissipate the heat rather than the bubbles. This cell configuration is called the forced convection design, the electrolyte is circulated using an external pump. The second design is the convection induced circulation and is shown in figure 2.2b. Here flow and mass transfer can be imposed by electrochemically producing bubbles at an electrode surface. The last design is the no net flow configuration, shown in figure 2.2c. The electrolyte undergoes an upward flow imposed by the bubbles. However, the free surface prevents the liquid from creating a net flow. Once the liquid reaches the free surface, it will move downwards near the central part of the cell and form two recirculation loops. This setup is not used in industry but is often used to better characterize the fundamental aspects of the flow, i.e., the spreading of the bubble plume [19].

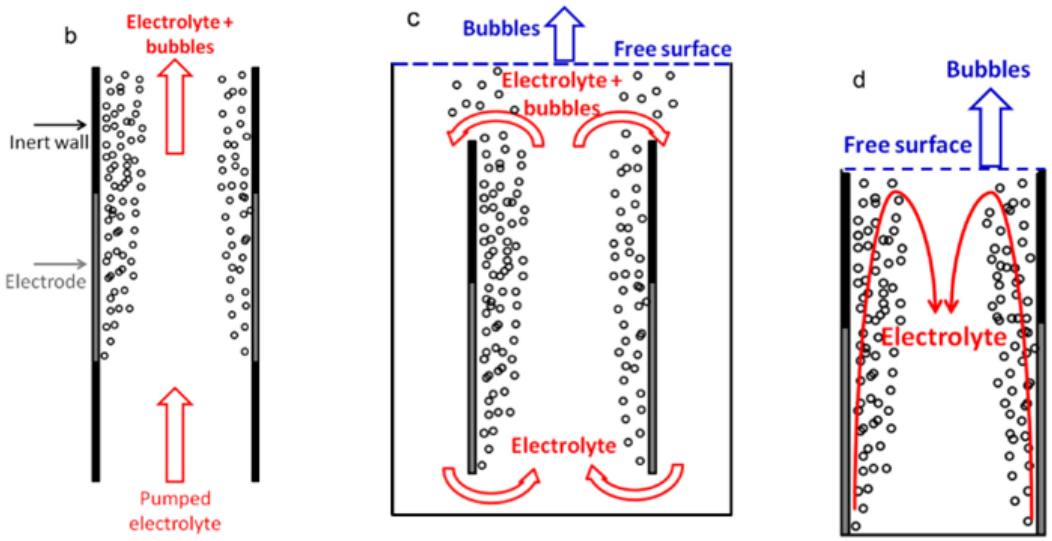

(a) Forced convection design (b) Convection induced design (c) No net flow design

Figure 2.2: Different configurations of vertical electrolyzers. [19]

2.1.2. Resistances in an electrolysis cell

As stated before an electrochemical reaction requires a sufficient electrical energy supply. This energy supply needs to overcome the reversible cell voltage as well as energy losses due to resistances. These resistances include electrical resistance of the circuit, activation losses, reduction of electrode surface due to partial coverage by gas bubbles and ionic transfer losses within the electrolyte solution. Figure 2.3 shows the resistance as an electrical circuit analogy.

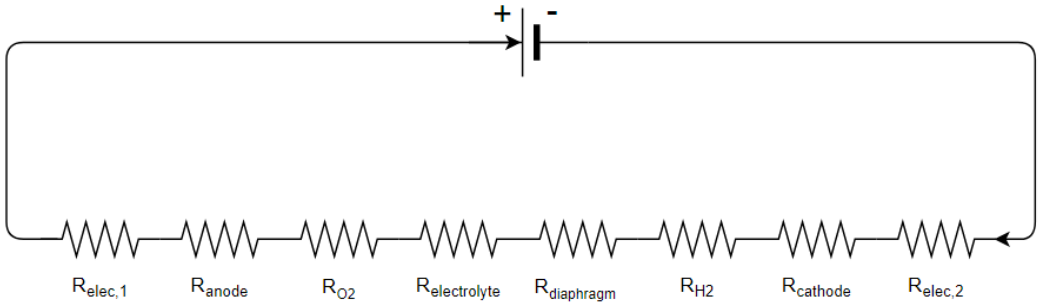

Figure 2.3: Resistances in the water electrolysis system through an electrical circuit analogy.

The first resistance on the left is $R_{elec,1}$ and is the external electrical circuit resistance at the anode, which includes the wiring and connections. The second resistance is the R_{anode} and indicates the losses due to the overpotential of the oxygen evolution reaction. R_{O2} expresses the resistance due to partial coverage of the anode by the oxygen bubbles. The resistances coming from the electrolyte and diaphragm are noted as $R_{electrolyte}$ and $R_{diaphragm}$. R_{H2} specifies the resistance due to partial coverage of cathode by the hydrogen bubbles. Next is the $R_{cathode}$ caused by the overpotential for the hydrogen evolution reaction. The electrical resistance on the cathode side is noted as $R_{elec,2}$. The total resistance of an electrolysis cell can be written as equation (2.4).

$$R_{Total} = R_{elec,1} + R_{anode} + R_{O2} + R_{electrolyte} + R_{diaphragm} + R_{H2} + R_{cathode} + R_{elec,2} \tag{2.4}$$

These resistances can be categorized into three groups. The first group is the electrical resistances, the second group is the transport resistances and the last group includes the reaction resistances [66].

- Electrical resistances: represent the losses in an electrolytic cell that occur mainly at the electrodes, electrical wires, and metal-metal joints. Optimization of the cell design can reduce the electrical resistance. The electrical resistance can be calculated with Ohm's law, shown in equation (2.5). Ohm's law is defined as the ratio of the voltage over the current. $R_{elec,1}$ and $R_{elec,2}$ belong to this category.

$$R_{circuit} = \frac{U}{I} \tag{2.5}$$

- Transport related resistances: are physical resistances such as bubble screening of the electrodes, bubbles present in the electrolyte. Also, resistances due to ionic transfer in the electrolyte belong to this category. Utilizing process intensification methods, transport related resistances are minimized, which is essential to make water electrolysis profitable. R_{O2}, $R_{electrolyte}$, $R_{diaphragm}$ and R_{H2} are considered as transport resistances.
- Electrochemical reaction resistances: are resistances due to the overpotentials required to overcome the activation losses, low activity, and degradation of the electrode surfaces. Applying nickel based alloys for the electrodes will decrease electrochemical reaction resistances. R_{anode} and $R_{cathode}$ belong to the reaction resistances.

Transport related resistances and reaction resistances, such as gas bubbles covering the electrode surfaces, gas bubbles present in the electrolyte, and overpotential of hydrogen and oxygen evolution are dependent on the current density. Another transport related resistance can be attributed to the dissolved hydrogen and oxygen gas in the electrolyte, which causes an increase in overpotential. This is also dependent on the current density, as shown by Shibata et al. [46]. The resistance through the diaphragm and wiring is fairly constant as the current density increases.

2.2. Mass transfer

During electrolysis, the electrolyte in the vicinity of the electrodes quickly becomes enriched with dissolved gases, which locally reaches supersaturation. This has been experimentally proven and reported [47], [45]. Shibata et al. conducted these experiments, he used a solution that contains 1 molar of sulphuric acid at room temperature and atmospheric pressure. The results of these experiments are shown in figure 2.4. The supersaturation of hydrogen has a limiting value at $11.6 \cdot 10^{-2}$ mol/l for currents exceeding about 300 A/m^2 , which is well over 100-fold of the saturation value [47]. Vogt et al. corrected these results by including the effect of OH^- [53]. Because of these corrections, the concentration found by Vogt differs from that of Shibata, especially at higher current densities. The supersaturation of oxygen exhibited a limiting value of $9.0 \cdot 10^{-2}$ mol/l for currents exceeding about 200 A/m^2, which is about 70-fold of the saturation value [45]. The results regarding the hydrogen side are shown in figure 2.4a and the results regarding the oxygen side are shown in figure 2.4b. Such high supersaturation can be attributed to the extremely low gas solubility, the low diffusivity of gases in liquids, combined with the very high production rate of hydrogen/oxygen, making it difficult for the dissolved gases to escape, resulting in an accumulation of dissolved gasses.

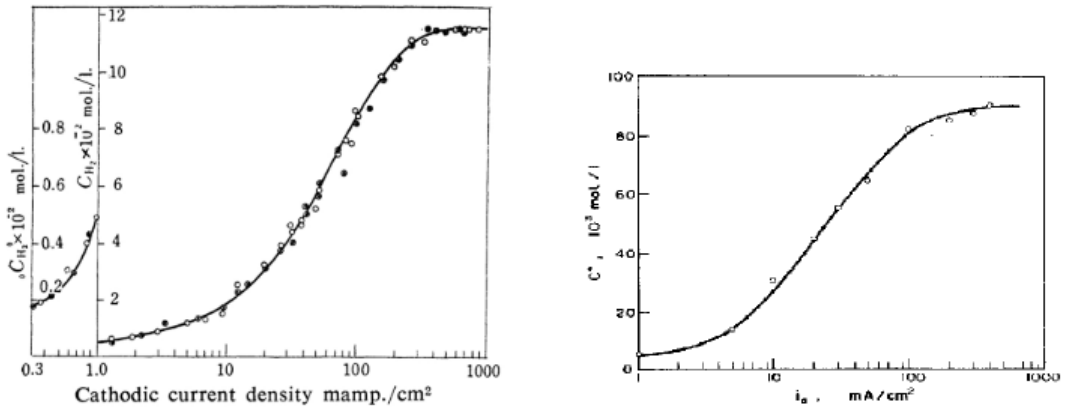

(a) The concentration of hydrogen near the hydrogen-evolving smooth platinum cathode. [47]

(b) The concentration of oxygen near the oxygen-evolving smooth platinum anode. [45]

Figure 2.4: The concentration of dissolved gas as a function of the current density in a 1 molar sulfuric acid solution.

Furthermore, the surface state of the electrode is important in the supersaturation levels, as demonstrated in an experiment performed by Shibata et al. [46]. In this experiment, it has been shown that the supersaturation is significantly higher when using a smooth electrode surface compared to a rough electrode surface. The results of this experiment are shown in figure 2.5. Here the overpotential caused by the presence of dissolved hydrogen gas is plotted against the current density, which is indicated with the white dots. Noticeable is the difference in overpotential for the different surface conditions of the electrode. From this, we can conclude that the concentration of dissolved gas adjacent to the electrode surface is dependent on the surface condition of the electrode.

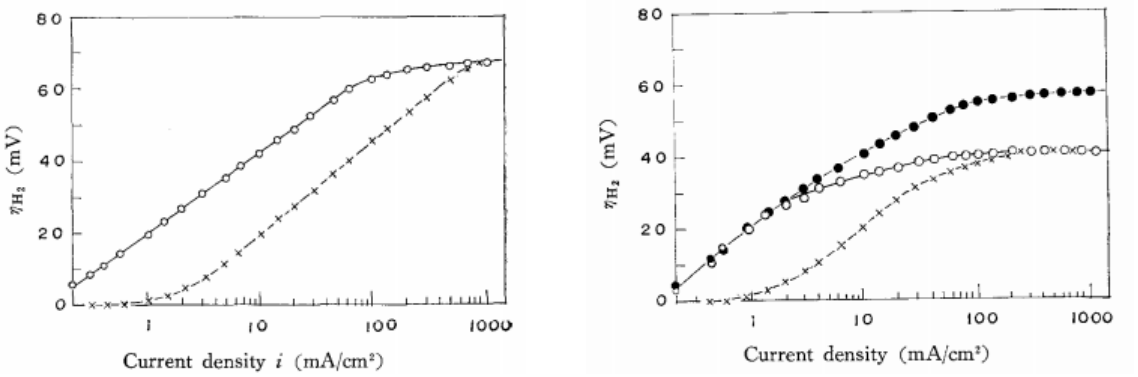

(a) The overpotential for a smooth platinum cathode. (b) The overpotential for a roughened platinum cathode.

Figure 2.5: The overpotential due to dissolved hydrogen as a function of current density in a 0.5 molar sulfuric acid solution. The experiments were performed with and without agitation of the electrolyte, indicated by the crosses and circles, respectively. The black dots the overpotential when the roughened platinum cathode is heated. [46]

Figure 2.4 shows the area adjacent to the electrode is oversaturated. However, only a fraction of the initially completely dissolved gas is desorbed by the gas bubbles adhering to the wall. This is called the gas evolution efficiency and is an important operation parameter in the behavior of gas evolving electrodes [54]. The remaining part of the dissolved gas is eventually desorbed by the bubbles present in the electrolyte. The gas evolution efficiency, f_g, can be determined by using equation (2.6).

$$f_G = \frac{N_G}{N_D} = 1 - \frac{N_E}{N_D} \tag{2.6}$$

The total dissolved gas flux, N_D, composes of a flux towards the bulk, N_E, and a flux transformed into the gaseous phase at the electrode, N_G. As illustrated in figure 2.6.

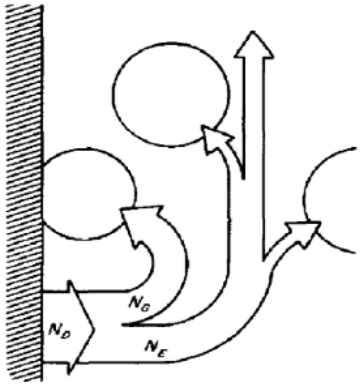

Figure 2.6: Transport mechanisms of dissolved gas from the electrode. [61]

Experimental investigations of bubble growth were conducted by Glas and Westwater [16]. The experiments were performed at room temperature in 0.5 M sulfuric acid solution. Based on the experimental bubble growth data obtained by Glas and Westwater, a follow-up study was done by Vogt, he was able to calculate the gas evolution efficiency [61]. The results are plotted in figure 2.7a. The gas evolution efficiency, f_G, is always well below 100%. However, there is a lot of scatter as investigations of bubble growth behavior are challenging. A more recent study by Haug et al. also reported gas efficiencies well below 100%. The results are shown in figure 2.7b. Therefore, it is reasonable to assume that the bubble continues to grow after it is released from the electrode.

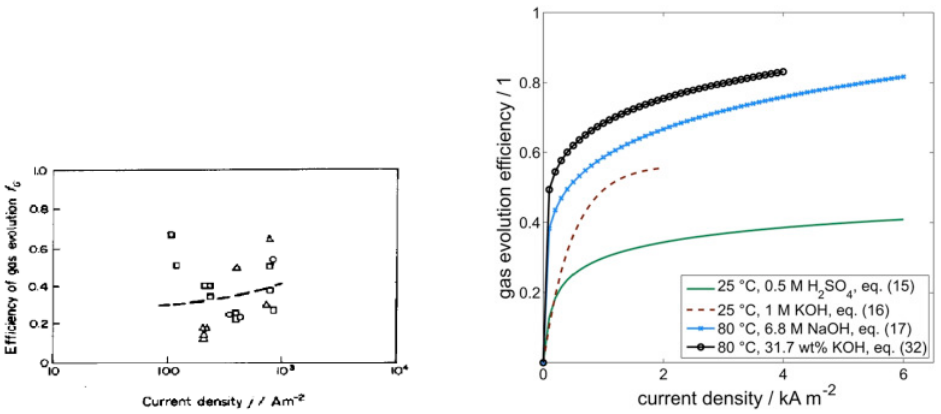

(a) Efficiency of gas evolution based on experimental data provided by Glas and Westwater [60].

(b) Efficiency of hydrogen evolution under various operating conditions. It should be noted that the lines are not data points, but power-law and exponential fits. [17]

Figure 2.7: Efficiency of gas evolution

Not all the dissolved gas goes directly into the gas phase, therefore mass transfer of dissolved gas occurs. Vogt et al. studied this phenomenon. According to his research, several mechanisms are involved in the desorption of dissolved gas [58]. These mechanisms are listed below and have been schematically illustrated in figure 2.8.

- N_1 is the mass transfer to the concentration boundary layer, δ_n, adjacent to the electrode.
- N_2 is the mass transfer of dissolved gas to the bubble layer, δ_b, near the electrode.
- N_3 is the mass transfer of dissolved gas to the region above the electrode.
- N_4 is the desorption of dissolved gas at the electrolyte surface. This is only present when operating at low current densities. In steady-state operation, most of the dissolved gas goes into the gas phase.
- N_5 is the unsteady term, $\frac{dc}{dt}$, which remains in the solution. In steady-state, this term disappears.

The overall mass balance shown in equation (2.7). For a detailed explanation about the different types of desorption systems, see Vogt [58].

$$N = N_1 + N_2 + N_3 + N_4 + N_5 \tag{2.7}$$

Where δ_N is the Nernst diffusion layer thickness and δ_b is the bubble layer thickness. In figure 2.8, the Nernst diffusion layer is indicated to be thinner than the bubble layer. It is assumed that the reaction rate is sufficient and therefore the thickness of the Nernst diffusion layer is quite thin. Also, the Nernst diffusion layer consists of ions that are attracted to the electrode resulting in a very thin layer.

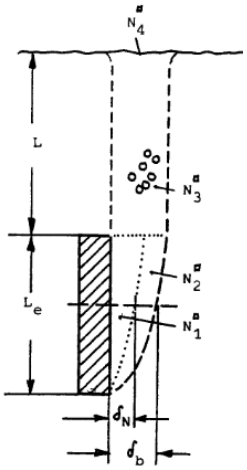

Figure 2.8: Schematic illustration of a gas evolving electrode including the different liquid-gas mass transfer fluxes. [58]

Figure 2.9 shows a schematic profile of the concentration of dissolved gas near the electrode [58]. The concentration of dissolved gas at the interface between the electrode and the electrolyte is labeled as C_e. Next, the concentration of the bulk is labeled as C_∞, which is larger than the gas-liquid interfacial concentration C_b. The bulk concentration is estimated to be higher than the saturation level. Since experiments have shown that the bulk of the electrolyte is significantly supersaturated when operating under industrial conditions [57]. However, this supersaturation is quite a bit lower than the supersaturation at the interface between the electrode and the electrolyte. Finally, the concentration at the surface of the bubble is C_s, which is the saturation concentration. As shown in figure 2.9, the concentration at the gas-liquid interface (C_b) is slightly higher than the saturation concentration (C_s). This is because of the curvature of the bubble [55].

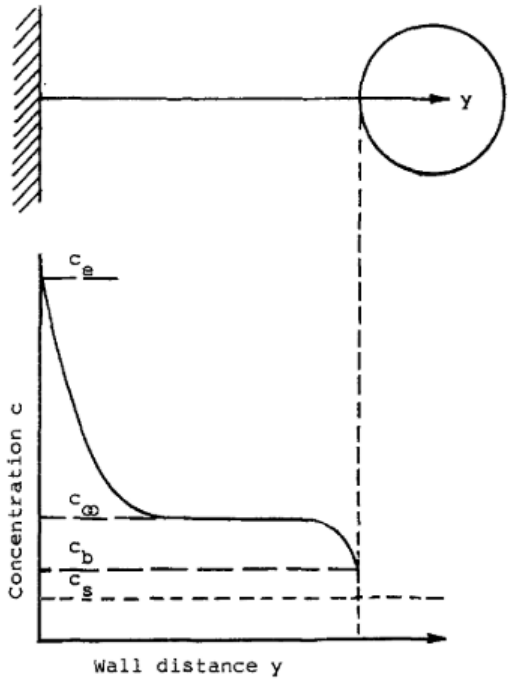

Figure 2.9: Schematic profile of the concentration of dissolved gas between an electrode and a bubble. [58]

2.3. Influence of bubbles

The formation of bubbles in water electrolysis is a widely observed process. The cell voltage for water electrolysis is considerably higher than the thermodynamic decomposition voltage due to a high overpotential. In addition to the high overpotentials, the resistance from the presence of gas bubbles in the electrolyte and at the electrode surfaces contributes to high energy consumption. Typical efficiencies for water electrolyzers are about 60%, which is a major drawback [40]. Therefore, it is important to better understand the influence of gas bubbles on cell performance.

2.3.1. Bubble Coverage

The fraction of a gas evolving electrode surface covered by adhering bubbles is called the bubble coverage and was introduced by Venczel [50]. The bubble coverage is influenced by several factors, e.g., the current density, the condition of the electrode surface and the nature of the gas [13]. Adhering gas bubbles exert multiple effects on the electrochemical process. First, the bubbles adhering to the electrode insulate a fraction of the surface making it inactive. However, this effect may be small due to the small contact angle, which is often the case with electrolytes and electrodes such as clean platinum. Additionally, the bubble coverage also affects the local current density. Therefore, the energy demand of the cell is affected. Second, the mass transfer of the reagent to the electrode and the dissolved gas from the electrode is affected by the adherent bubbles. Since mass transfer (of ions and dissolved gas) is limited to the active part of the electrode, this will result in a lower mass transfer coefficient. However, bubbles growing at and detaching from the electrode induce micro-convection in the boundary layer, resulting in an improvement of mass transfer [59]. Moreover, the area covered by the bubbles also influences the gas-liquid interface, which affects the rate of dissolved gas contributing to bubble growth. Therefore, the area covered by adhering bubbles is essential for assessing the operational behavior of gas evolving electrodes. To reduce these effects (energy losses, bubbles making part of the electrode inactive, etc.), different techniques can be implemented, such as increasing the pressure [24], applying an ultrasonic field [62], using a forced electrolyte flow [3], etc. An example of such an experiment was conducted by Balzer et al. [3]. This experiment was performed with vertical gas evolving electrodes, under a forced upward electrolyte flow. The results of this experiment are shown in figure 2.10.

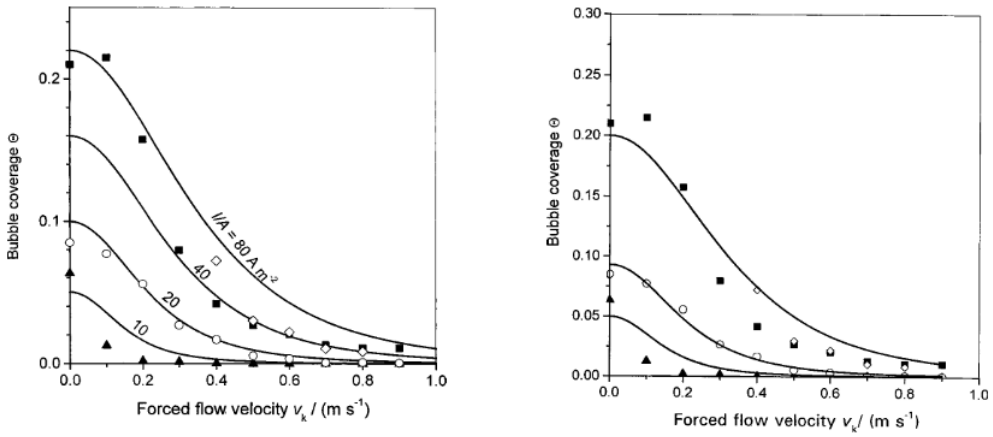

(a) Bubble coverage hydrogen-evolving cathode. (b) Bubble coverage hydrogen-evolving anode.

Figure 2.10: Bubble coverage on a copper electrode as a function of flow velocity in a 1 molar potassium hydroxide solution. The solid black lines are bases on an empirical formula. [3]

The experimental data show a substantial decrease in bubble coverage for relatively high velocities. Therefore, it is beneficial to operate a cell with a forced flow or design the cell in such a way that the

gas bubbles induce a flow.

2.3.2. Bubble departure diameter

Bubble detachment is the process of a bubble unpinning from a surface. This process has been studied extensively in theoretical and experimental studies [36], [26], [67], [49]. The region where these bubbles detach from the electrode surface is called the adherence region. There are two systems in which these bubbles detach from the electrode surface [22]. In the first system, a gas bubble releases smoothly from the electrode surface. This is probably due to the growth of the bubbles, where the buoyancy force exceeds the force that causes the bubbles to stick to the electrode. In the second system, the bubbles burst out of the adherence region into the bulk of the electrolyte. Janssen et al. attributed bubbles bursting out of the adherence region to the coalescence of bubbles [22]. Several steps are involved in bubble formation on the electrodes such as, nucleation, growth, and departure. These steps determine both the residence time and the diameter of the gas bubbles, which influence the resistance. One of the most influential effects of resistance is the gas bubble departure diameter. It is important to fully understand gas bubble behavior in order to reduce the resistance of gas bubble formation on the electrode. Zhang et al. [67] studied the behavior of electrolytic gas bubbles and their effect on the cell voltage. In this study, a force balance analysis was used to predict the critical diameter for the departure of gas bubbles. Figure 2.11 shows the forces acting on the gas bubble. These forces are the buoyancy force, the interfacial tension force, the drag force, and the lift force.

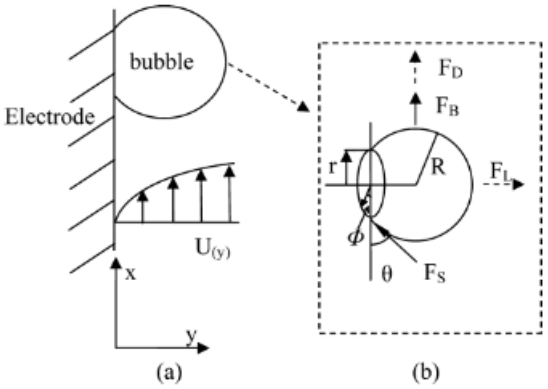

Figure 2.11: Schematic representation of a gas bubble on an electrode surface with the corresponding forces acting on the bubble. [67]

The forces acting on a gas bubble can be decomposed into components along the x and y-axis. The gas bubble sticks on the electrode if both ΣF_x and ΣF_y are equal to zero. If one of these conditions fails, the gas bubble will depart and detaches from the electrode. Zhang et al. reported that the force balance consists of three terms: the buoyancy force, the interfacial tension force, and the drag force. When the flow is stagnant, the drag force is assumed be equal to zero (In reality, the drag force will never equal zero due to the movement of nearby bubbles causing natural convection). Therefore, introducing an electrolyte flow will reduce the critical diameter of departure and improve efficiency. This phenomenon was also reported by Landolt [28].

An experiment performed by Ibl et al. observed the bubble departure radius depends on the type of electrode [20]. He noted that the bubble departure radius on a platinum electrode is larger compared to a copper electrode. He concluded that the difference was due to the number of nucleation sites that affect the growth of the bubble. Also, the wettability of the electrode material differs, which corresponds to the bubble's adhesion forces to the surface.

Jansen studied the effect of current density and the departing bubble size [23]. He reported an increase in bubble departure radius with current density. However, Venczel reported a decrease in

bubble size with current density [49]. So, there remains some disagreement in the literature regarding the effect of current density on the departing bubble size.

The electrode material, electrolyte conditions, and surface roughness are all important factors in the bubble departure radius [6], [5]. On smooth electrode surfaces, the bubble radius tends to increase [32]. In the case of a rough electrode surface, the contact angle of the base bubble changes, which may affect the bubble departure radius.

2.3.3. Bubble size in the flow direction

In addition to the losses, the formation of bubbles also creates additional modeling difficulties besides that of simulating two-phase flow. One of the problems is the bubble size. This can be crucial for the computational effort to accurately simulate the shape of the bubble plume, for example. Most simulations use a mono-disperse bubble size on the electrode surface. In reality, there is a wide range of bubble sizes, as illustrated in figure 2.12. Two things stand out here, i.e., that no bubbles were measured smaller than 45 μm and the peak that can be seen at 126 μm. Bubbles smaller than 45 μm were too difficult to identify and were excluded from distribution. The peak seen at 126 μm is due to the coalescence of bubbles.

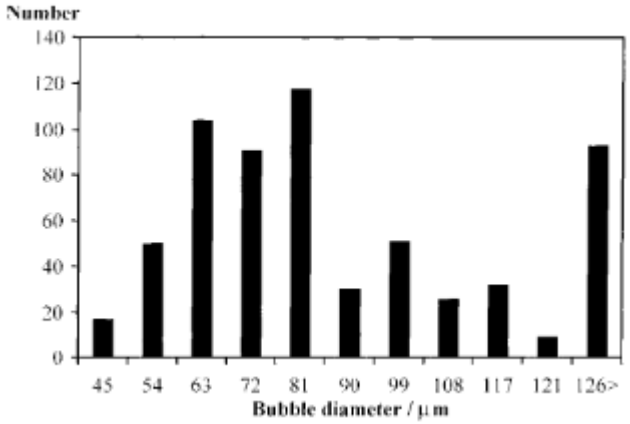

Figure 2.12: Bubble size distribution just above the electrode in a 50 g/L sodium sulfate solution operated at a current density of 2000 A/m^2. The cathode consists of a coated titanium electrode. [5]

The characteristics of bubble size distribution depend on several parameters, such as surface conditions, electrolyte solution, the concentration of dissolved gas, etc. Various experimental studies [5], [19], [1] have shown four major phenomena that may change the bubble size:

- Bubble coalescence
- Change in hydrostatic pressure
- Water vapor
- Mass transfer of dissolved gas

Flow visualizations have shown bubble coalescence only occurs close to the electrode surface [19]. However, due to the high ionic strength of electrolyte solutions, coalescence is limited. Therefore, coalescence is generally neglected in numerical models. The change in hydrostatic pressure exerted on the bubbles during their ascent is insignificant unless the height of the cell exceeds several meters or operates at very low pressure. This can be demonstrated by means of the ideal gas law:

$$pV = nRT \tag{2.8}$$

According to the ideal gas law, the volume increases by about 10% for every meter a bubble rises. Since the vertical channels used in the experiments are usually well below a meter, the volume increase due to the change in hydrostatic pressure is quite limited. The presence of water vapor could increase the size of the bubbles. According to Zarghami et al., the mole fraction of water vapor in the gas phase is approximately 0.26 (in an alkaline solution at 353 Kelvin) [65]. The influence of the presence of water vapor on the bubble size can be shown by combining the ideal gas law and Amagat's law of partial volumes:

$$V_{\text{mixture}} = \frac{(n_a + n_b)RT}{p_{\text{mixture}}} \tag{2.9}$$

Next, divide the volume of water vapor by the volume of the gas mixture. This results in the following equation:

$$x_i = \frac{V_i}{V_{\text{mixture}}} \tag{2.10}$$

From this, it becomes clear that the mole fraction, x_i, is equal to the volume fraction. This indicates that water vapor can take up a significant portion of the bubble growth. However, the mole fraction of water vapor was obtained from an experiment conducted at a temperature of 353 Kelvin, which is fairly close to the boiling point of water. In experiments conducted at room temperature, the mole fraction of water vapor will likely be lower. Another hypothesis for the increase in bubble diameter is the mass transfer of dissolved gas. As reported in different studies [60], [5], [1], [56], mass transfer can cause significant changes in the bubble diameter. Nonetheless, bubble growth through mass transfer is generally neglected in numerical models. Multiple experimental studies [5], [6], [32], [19] have shown an increase in mean bubble diameter in the direction of flow along the electrode surface. Furthermore, it was observed that the bubble diameter increases from the electrode surface to the bulk region [5], [6], [32], [19]. Figure 2.14 shows the results of the experiments conducted by Boissonneau. He observed a significant increase in the hydrogen bubble diameter between point A (bottom electrode) and point B (top electrode). Another experiment performed by Hreiz, measured the mean bubble size of oxygen bubbles along the height of the electrode, these results are shown in figure 2.13a. The last experiment was performed by Lumanauw, shown in figure 2.13b. He also observed a notable increase in mean bubble size. From the experiments mentioned above, several statements can be made. The first statement clearly shows that bubble growth is significant in all experiments. From figure 2.13 a second statement can be made namely, when a bubble reaches a certain size, it stops growing. Since bubble dispersion is proportional to bubble size, it might indicate that the bubble has left the dissolved gas layer and therefore has stopped growing. Another explanation could be that above a certain height the dissolved gas concentration decreases to such an extent that growth is no longer or hardly possible. Since the dispersion of bubbles is proportional to bubble size, it is important to take this into account when performing the simulations.

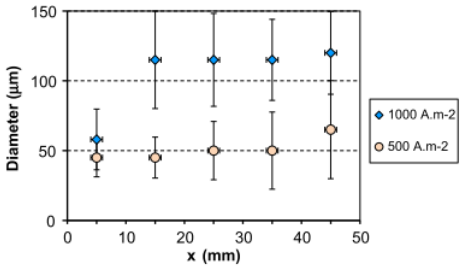

(a) The mean oxygen bubble diameter in a 0.5 molar sodium hydroxide solution. [19]

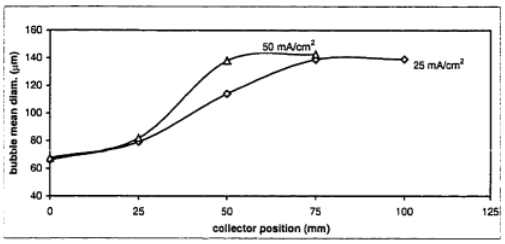

(b) The mean hydrogen bubble diameter in a 1 molar potassium carbonate solution. [32]

Figure 2.13: The mean bubble diameter as a function of height.

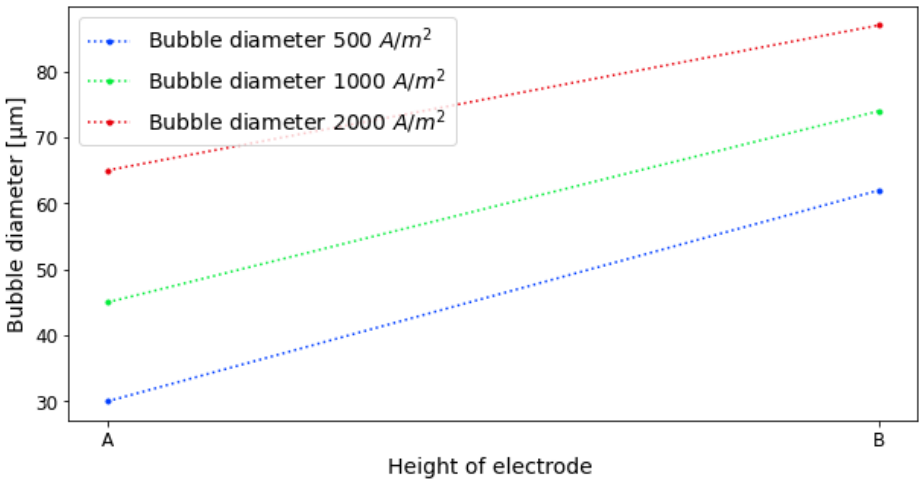

Figure 2.14: The mean hydrogen bubble diameter on the titanium electrode for three different current densities in a 50 g/L sodium sulfate solution. [5]

Parameter	Properties	Dimensions
p	Pressure	$\frac{kg}{m \cdot s^2}$
V	Volume	m^3
n	Number of moles	
$R_{\text{universal}}$	Universal gas constant	$\frac{kg \cdot m^2}{s^2 \cdot K \cdot mol}$
T	Temperature	K
x_i	Mole fraction species i	

Table 2.1: Parameters used in ideal gas law.

2.3.4. Bubble layer

The two-phase flow in electrolyzers has been extensively studied [18], [5], [42], [31]. It has been reported that bubbly flows consist of three regions: adherence, bubble diffusion, and bulk region [5]. In the adherence region, the bubbles are attached to or very close to the electrode surface, which has a thickness equal to the mean bubble diameter. In the bubble diffusion region, the bubbles are very concentrated. The concentration of dissolved gas in the diffusion layer is several times greater than that of the saturation level, hence bubble growth was observed. In the bulk region, only large, dispersed bubbles are observed. These bubbles arrived there through coalescence from the electrode surface [22]. This region is considered to have supersaturation at or near the level of the bulk solution since no significant bubble growth was observed. The different regions in the bubble layer are illustrated in figure 2.15.

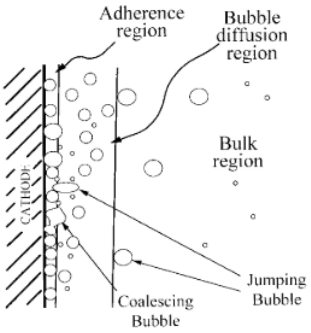

Figure 2.15: Schematic representation of the three regions in a bubble layer. [5]

The shape and thickness of a bubble layer depend on several parameters, e.g., the current density, flow rate, nature of the gas, height of the electrode, etc. Unfortunately, very little experimental data is available on bubble plume thickness. Some of the available data is shown below and in the appendix A.2. Figure 2.16 illustrates the development of the hydrogen bubble layer along the height of the electrode from multiple experiments. The data shown in figure 2.16 was collected from experiments performed by Baczyzmalski et al. [2], Pang et al. [37] and Weier et al. [64]. These experiments were conducted with a no flow configuration and at a current density of 100 to 200 A/m^2. Data shown in figure 2.16 indicates clearly that the thickness of the bubble layer corresponds reasonably well with the different experiments. Different experiments differ slightly from each other is due to the slightly different conditions and measurement errors.

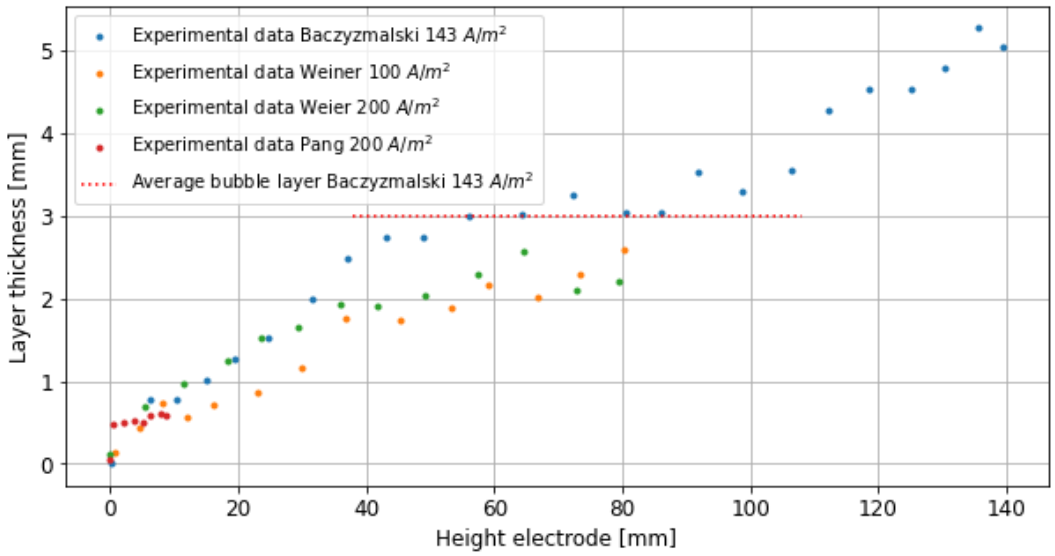

Figure 2.16: Hydrogen bubble layer thickness along the height of the electrode for various experiments. The configuration of the cell corresponds to the configuration shown in figure 2.2c.

Figure 2.17 shows the data from figure 2.16 on a log-log scale. Where the black dashed line indicates a reference line to determine the shape of the plume. As can be seen in the figure below, most of the data points are in line with the black dashed line, with the exception of the data made available by Pang et al. This might be due to the small scale on which Pang et al. conducted his experiments. An overview of the bubble layers of different experiments is available in appendix A.2.

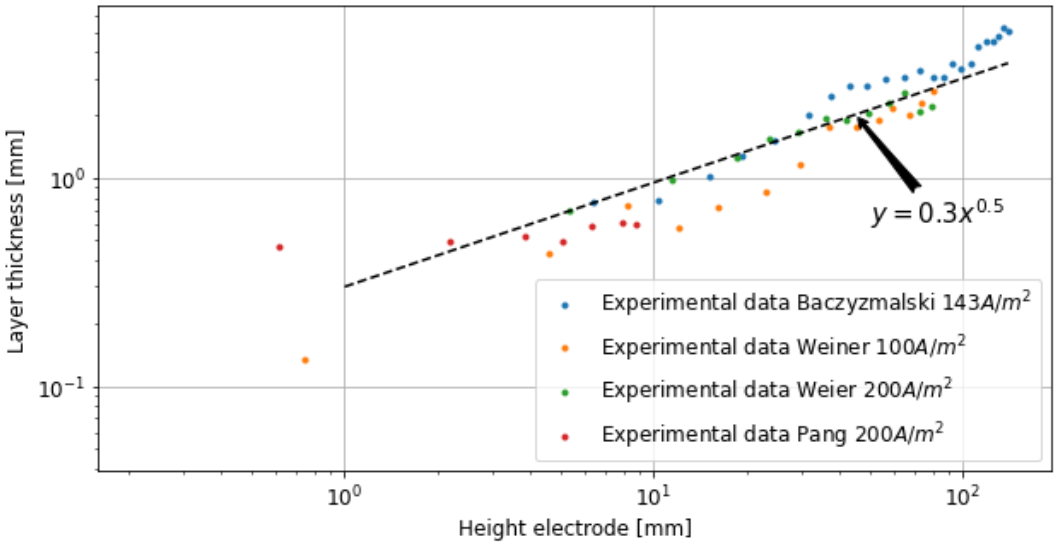

Figure 2.17: Bubble layer thickness along the height of the electrode on a log-log plot.

Pang et al. conducted experiments operating at 200 A/m^2 over a wide range of Reynolds numbers [37]. Figure 2.18 shows five images of different Reynolds numbers during electrolysis. As shown in the images, electrolyte flow affects the thickness of the bubble layer. When the flow rate increases the bubbles have less time to disperse, resulting in a very narrow bubble layer. However, increasing the Reynolds number beyond the critical Re $\approx$ 1200 causes the bubble layer to increase again, probably due to flow transitioning into turbulent conditions.

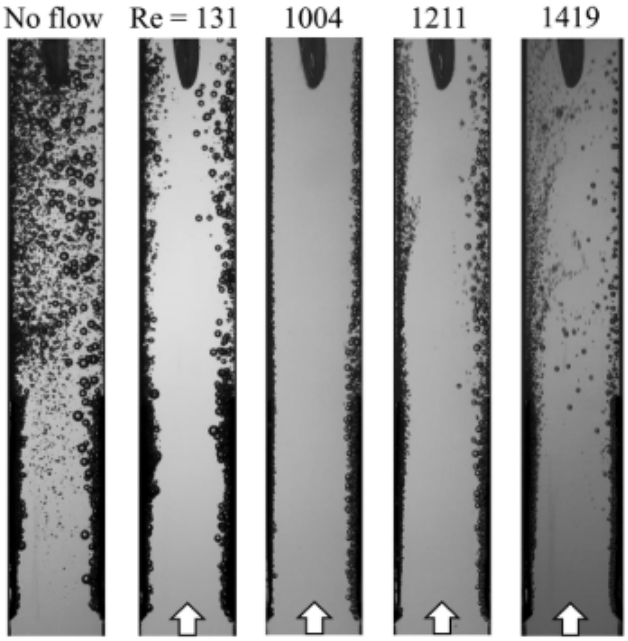

Figure 2.18: Representative still images of the bubble plume in a 0.5 molar sulfuric acid solution at various Reynolds numbers operated at a current density of 200 A/m^2. [37]

Pang has shown that increasing the flow rate reduces the thickness of the bubble plume, Lee et al. observed the same phenomenon [31]. The results of the experiments performed by Lee are shown in figure 2.19. When increasing the current density, the thickness of the plume also increases. This is because the gas production is proportional to the current density. At a higher current density, more bubbles are present, causing the bubbles to push each other away, resulting in a thicker bubble plume.

Although the thickness increases with current density, the shape of the plume remains the same. When plotting the curves from the figures below on a log-log plot, the shape of the bubble plume emerges. The shape of the bubble plume can be described with equation (2.11).

$$y = Ax^b \tag{2.11}$$

As shown in figure 2.19, the power required to fit the shape of the bubble plume is for oxygen side 0.5 and for hydrogen side 0.8.

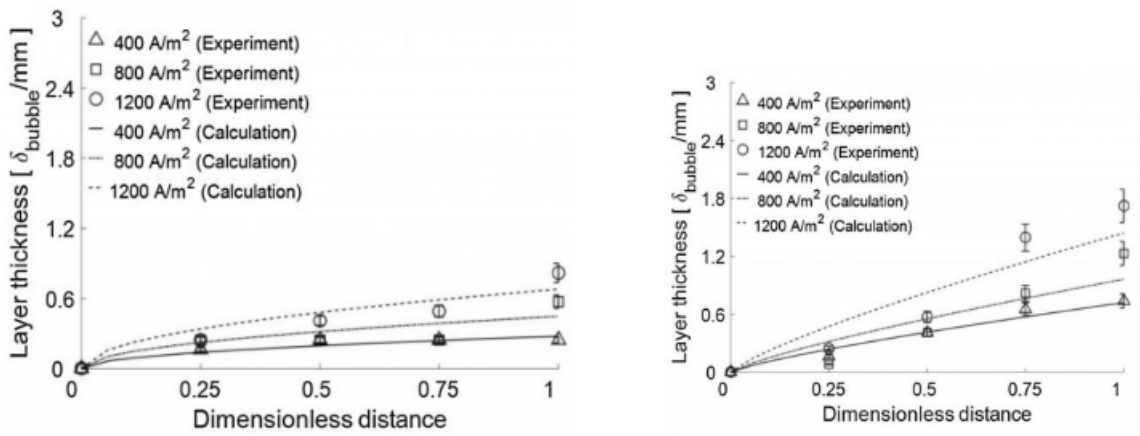

(a) Bubble layer thickness oxygen side.

(b) Bubble layer thickness hydrogen side.

Figure 2.19: Bubble layer thickness along the height of the electrode for various current densities in a potassium hydroxide solution (0.833 wt %) with an Ir/Ru alloy (Iridium-Ruthenium) for the electrodes. The experiment was performed in a vertical channel using a forced flow (Re = 900, 0.18 m/s). [31]

Bongenaar et al. derived an expression for the bubble layer thickness using experimental data [7]. This study concluded that the bubble layer depends on the following parameters: current density, j, height of the electrode, h, and the velocity of the liquid, v_l. The bubble layer thickness is fitted with:

$$\delta \approx j^{c_1} v_l^{c_2} h^{c_3} \tag{2.12}$$

Parameter	Properties	Exponent	Value
j	Current density	c_1	0.1
v	Liquid velocity	c_2	-0.2
h	Height of electrode	c_3	0.3

Table 2.2: Approximation bubble layer thickness.

2.3.5. Gas fraction

Regarding gas fraction near the electrode surface, only limited experimental data is available. However, some studies provide some insights into the gas fraction near the electrode. An example is a study performed by Riegel et al. In this study, the gas fraction of hydrogen bubbles in an aqueous solution was determined [42]. These measurements were performed in a 1 molar potassium hydroxide solution at a mean velocity of 0.69 m/s and a temperature of 50 ℃. Figure 2.20a shows the gas fraction for different current densities as a function of the cathode distance. The gas fraction decreases with increasing cathode distance and increasing the current density results in a higher gas fraction.

Another experiment performed by Bongenaar et al. examined the gas distribution in the electrolysis cell [7]. These experiments were also performed in a 1 molar potassium hydroxide solution at a forced electrolyte flow (0.3 m/s). Figure 2.20b shows the gas fraction versus the distance from the electrode. As would be expected, the gas fraction in the electrolyte increases with increasing height. The width of the bubble layer adjacent to the electrode is dependent on the height in the electrolytic cell.

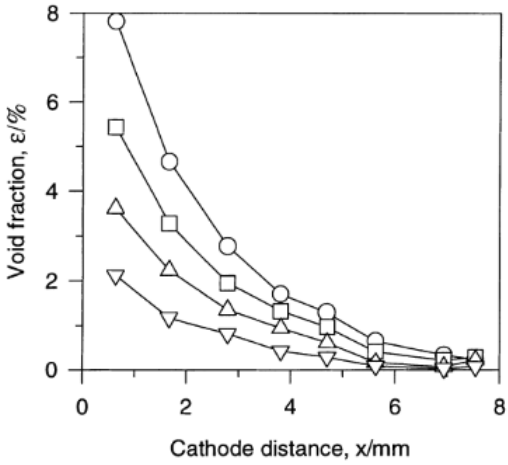

(a) Gas fraction at various current densities ((○) 6250, (□) 3250, (△) 1500 and (▽) 500 A/m^2) in a 1 molar potassium hydroxide solution. The void fraction was determined by measuring the electrical resistance. [42]

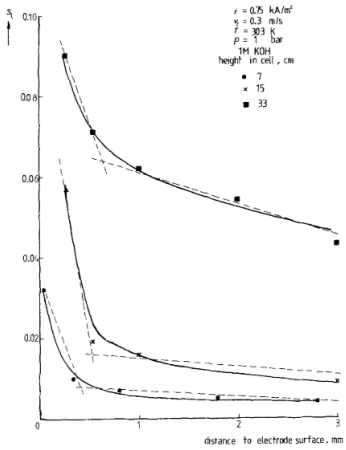

(b) The gas fraction at various heights in the cell (7cm, 15cm, 33cm), in a 1 molar potassium hydroxide solution at a current density of 750 A/m^2. The void fraction was determined by the illumination of the bubbles. [7]

Figure 2.20: Gas fraction as a function of distance to the electrode surface. Both experiments were performed in a gap configuration with a diaphragm.

The experiments mentioned in figure 2.20 were conducted in the turbulent regime. For the gas fraction in the laminar regime, no experimental data is available. There are simulation results, although they have not been validated [63], [30]. Figure 2.21 shows the gas fraction in the laminar regime. The gas fraction can reach 0.35, which is significantly higher in comparison with the experiments performed in the turbulent regime.

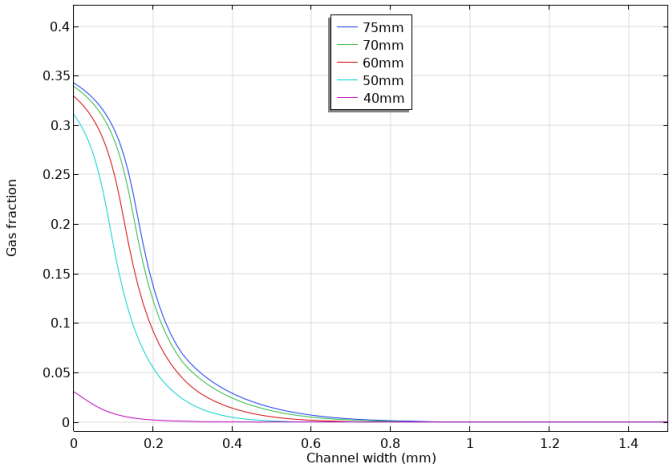

Figure 2.21: Simulation result for the gas fraction based on the experiment performed by Boissonneau. The simulation was performed at a current density of 1000 A/m^2.

2.3.6. Bubble growth

During electrolysis, gases are being produced at both electrodes. Some of the produced gases will dissolve into the electrolyte. Due to the low solubility of gases in a liquid, the adjacent liquid will quickly become supersaturated. If the supersaturation exceeds the required value, nucleation occurs and bubbles begin to form [51]. After nucleation, the bubble grows rapidly on the electrode surface since the supersaturation factor in the vicinity of the electrode is high. The bubble attached to the electrode is stationary. However, the fluid around it is in motion, also the growth itself introduces advective transport. Figure 2.22 shows an average bubble growth in the adherence region. Also, shown in figure 2.22 the bubble growth depends on the current density.

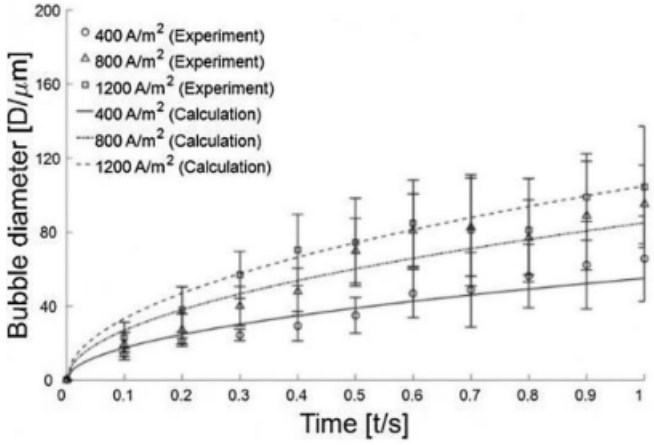

Figure 2.22: Oxygen bubble growth in the adherence region as a function of time for various current densities in a potassium hydroxide solution (0.833 wt %) with an Ir/Ru alloy (Iridium-Ruthenium) for the electrodes. The experiment was performed in a vertical channel using a forced flow (Re = 900, 0.18 m/s). However, the Reynolds number was assumed to be almost zero in the adherence region. [31]

Once the bubble reaches the critical diameter, the bubble will detach from the electrode and move through the oversaturated electrolyte. Here the bubble grows by diffusion and convection. The growth of gas bubbles in water electrolysis is an important subject in bubble dynamics. In water electrolysis, many bubbles are present in the electrolyte. As a result, each bubble is influenced by its nearby neighbors, which makes it a rather complicated problem to solve. A more simple problem, is the growth of a single bubble during electrolysis. In literature, bubble growth in supersaturated solutions has been investigated. Two important theoretical papers are those by Epstein–Plesset [14] and Scriven [44]. Based on the work of Epstein–Plesset and Scriven, Vachaparambil et al. [48] made a numerical approach of a rising bubble in a supersaturated solution. The numerical model considers a two-dimensional growing bubble and can be described by equation (2.13).

$$\frac{dR_b}{dt} = \frac{M_i}{\rho_g} k(C_i - C_s) \tag{2.13}$$

The mass transfer coefficient, k, is based on the Sherwood number. Some examples of Sherwood numbers reported in the literature are listed in table 2.3. Modeling mass transfer based on Sherwood number can lead to large errors as these correlations are dependent on the local velocity. The Reynolds number is based on the slip velocity of the bubble in question.

Sh correlation	Flow scenario	
Sh = 2	Re = 0 flow around a spherical bubble	[52]
Sh = $2 + 0.6515\sqrt{\mathrm{ReSc}}$	Re « 1 Flow around a bubble	[4]
Sh = $2 + 0.6\sqrt{\mathrm{Re}}\mathrm{Sc}^{0.33}$	2< Re < 200 flow around a droplet	[41]

Table 2.3: Sherwood number for different operating conditions.

The mass transport coefficient for lower Reynolds numbers can be determined with equation (2.14).

$$k = \frac{D}{2R_b}\mathrm{Sh} = \frac{D}{2R_b}(2 + 0.6515\sqrt{\mathrm{ReSc}}) \tag{2.14}$$

The mass transport coefficient for higher Reynolds numbers can be be determined with equation (2.15).

$$k = \frac{D}{2R_b}\mathrm{Sh} = \frac{D}{2R_b}(2 + 0.6\sqrt{\mathrm{Re}}\mathrm{Sc}^{0.33}) \tag{2.15}$$

Neglecting the convection term, Re = 0, the equation for the mass transfer coefficient can be written as (2.16).

$$k = \frac{D}{2R_b}\mathrm{Sh} = \frac{D}{R_b} \tag{2.16}$$

Parameter	Properties	Dimensions
M_i	Molecular weight of species	$\frac{kg}{mol}$
Sc	Schmidt number	
Re	Reynolds number	
c_i	Concentration of species	$\frac{mol}{m^3}$
c_s	Saturation gas concentration	$\frac{mol}{m^3}$
R_b	Bubble radius	m
D	Diffusion coefficient	$\frac{m^2}{s}$
ρ_g	Density gas	$\frac{kg}{m^3}$
k	Mass transfer coefficient	$\frac{m}{s}$

Table 2.4: Parameters used in the calculation of the bubble radius.

2.3.7. Motion of bubbles

Volume forces or slip velocities can be used to describe the relative motion of the dispersed phase. Volume forces are used in the Euler-Euler model and the slip velocities are used in the simplified Euler-Euler models. However, this thesis mainly uses the simplified Euler-Euler model, the so-called

Bubbly flow model (only available in COMSOL). Therefore, only the slip velocities are treated. The slip velocities below are derived from the sedimenting of spherical rigid particles on an inclined surface. Dahlkild [12] adapted this model to describe the relative motion of bubbles. Although, it neglects several phenomena, such as the formation of bubbles, bubble coalescence and bubble break off. It does provide a good approximation to represent the behavior of bubbles. The motion of the dispersed phase relative to the liquid and can be written as given in equation (2.17). This is called the relative superficial slip velocity. By dividing the relative superficial slip velocity by $\alpha(1-\alpha)$ we end up with the interstitial slip velocities (real slip velocities), the derivation of this can be found in appendix A.3.

$$\mathbf{U}_r = \mathbf{U}_{Stokes} + \mathbf{U}_{Saff} + \mathbf{U}_{Hdiff} + \mathbf{U}_{Sdiff} + \mathbf{U}_{Mig} \tag{2.17}$$

The first term $\mathbf{U}_{Stokes}$ is the Stokes flux which results from a balance between buoyancy and drag forces and can be determined using equation (2.18).

$$\mathbf{U}_{Stokes} = \alpha f(\alpha) v_{Stokes} \mathbf{e}_x \tag{2.18}$$

The $f(\alpha)$ term is the hindering function induced by neighboring bubbles and was formulated by Nicolai [35]:

$$f(\alpha) = (1-\alpha)^5 \tag{2.19}$$

The Stokes velocity, v_{Stokes}, describes the terminal rise velocity of a single particle of radius r_b. Where g is the gravitational constant and ν_l is the kinematic viscosity. The Stokes velocity can be calculated using equation (2.20). The stokes velocity is only valid if the Reynolds number is equal to or less than one.

$$v_{Stokes} = \frac{2gR_b^2}{9\nu_l} \tag{2.20}$$

The second term $\mathbf{U}_{Saff}$ is a lift flux resulting from the rotation of (small) particles in a sheared flow. Where $\dot{\gamma}$ is the shear rate term for a flow between vertical plates. The lift flux can be described as follows:

$$\mathbf{U}_{Saff} = -\alpha f(\alpha) v_{Stokes} sgn(\dot{\gamma}) \frac{6.46}{6\pi} \sqrt{\frac{R_b^2 |\dot{\gamma}|}{\nu_l}} \mathbf{e}_y \tag{2.21}$$

The third term $\mathbf{U}_{Hdiff}$ is the hydrodynamic self-diffusion. This describes the irregular path of bubbles in a plume. Where $\mathbf{D}$ stands for the non-isotropic dimensionless dispersion coefficient, which was empirical determined by Nicolai [35]. The non-isotropic dimensionless dispersion coefficient is a 2x2 matrix, shown in (2.23). When determining the matrix vector product (closely related to the dot product), we get a slip velocity in the horizontal and vertical direction. The hydrodynamic self-diffusion can be calculated using the following equation:

$$\mathbf{U}_{Hdiff} = -R_b v_{Stokes} f(\alpha) \mathbf{D} \nabla \alpha \tag{2.22}$$

$$\mathbf{D} = \begin{bmatrix} 8 & 0 \\ 0 & 1 \end{bmatrix} \tag{2.23}$$

The last two terms describe the increase of collision frequency. The second to last term is the shear-induced diffusion, $\mathbf{U}_{Sdiff}$, and can be calculated using equation (2.24). $\beta(\alpha)$ is a non-dimensional coefficient.

$$\mathbf{U}_{Sdiff} = -R_b^2|\dot{\gamma}|\beta(\alpha)\nabla\alpha \tag{2.24}$$

$$\beta(\alpha) = \frac{1}{3}\alpha^2(1 + 0.5\exp(8.8\alpha)) \tag{2.25}$$

The last term is the shear-induced migration, $\mathbf{U}_{Mig}$, and is shown in equation (2.26). Here $\kappa(\alpha)$ is a non-dimensional coefficient.

$$\mathbf{U}_{Mig} = -R_b^2|\dot{\gamma}|\frac{\kappa(\alpha)}{\tau}\nabla\tau \tag{2.26}$$

$$\kappa(\alpha) = 0.6\alpha^2 \tag{2.27}$$

The above equations((2.17) - (2.27)) can be found in the paper by Schillings et al. [43].

$\mathbf{U}$ = Is the superficial velocity and is used in most papers.

$\mathbf{u}$ = Is the interstitial velocity and is used in COMSOL to describe fluid motion.

Parameter	Properties	Dimensions
α	Volume fraction gas	
$\kappa(\alpha)$	Non-dimensional shear-induced migration coefficient	
$\beta(\alpha)$	Non-dimensional shear-induced diffusion coefficient	
$\mathbf{D}$	Non-dimensional hydrodynamic diffusion coefficient	
$\mathbf{e}_x$	Unit vector along the electrode	
$\mathbf{e}_y$	Unit vector perpendicular to the electrode	
ν_l	Kinematic viscosity	$\frac{m}{s^2}$
g	Gravity constant	$\frac{m}{s^2}$
τ	Shear stress	Pa
$\dot{\gamma}$	Shear rate	s^{-1}
$\mathbf{U}$	Superficial velocity	$\frac{m}{s}$
$\mathbf{u}$	Interstitial velocity	$\frac{m}{s}$
R_b	Bubble radius	m

Table 2.5: Parameters used in the slip velocities.

2.4. Numerical model

2.4.1. Bubbly flow model

In water electrolyzers gas-liquid flows are of great interest since the distribution of gas throughout the electrolyte influences the amount of electrical energy required to produce hydrogen. Computational Fluid Dynamics (CFD) is used to get a better understanding of this phenomenon. Two main approaches could be taken using CFD, i.e., the Eulerian and Lagrangian approach. Both approaches are characterized by specific advantages and disadvantages. In this thesis, only the Eulerian method is used. The two-fluid Euler-Euler model describes the dynamics of each of the phases, using momentum balance equations and continuity equations. However, a couple of simplifications can be made, relying on the following assumptions [10]:

- "*The gas density is negligible compared to the liquid density. Therefore, the gas density is neglected in the momentum equation.*"
- "*The motion of the gas bubbles relative to the liquid is determined by a balance between viscous drag and pressure forces.*"
- "*The two phases share the same pressure field.*"

"*Based on these assumptions, the momentum and continuity equations for the two phases can be combined and a gas phase transport equation is kept in order to track the volume fraction of the bubbles*" [10]. The simplified model is called the Bubbly flow model (name of the model used by COMSOL). The momentum equation reads:

$$(1-\alpha)\rho_l[\frac{\partial \mathbf{u}_l}{\partial t} + \mathbf{u}_l \cdot \nabla \mathbf{u}_l] = -\nabla P + \nabla \cdot [(1-\alpha)\mu_l \mathbf{K}] + (1-\alpha)\rho_l \mathbf{g} + \mathbf{F} \tag{2.28}$$

Where $\mathbf{K}$ is the stress tensor, shown in equation (2.29).

$$\mathbf{K} = \nabla \mathbf{u}_l + \nabla \mathbf{u}_l^T - \frac{2}{3}(\nabla \cdot \mathbf{u}_l)\mathbf{I} \tag{2.29}$$

The continuity equation is shown in equation (2.30). In contrast to the momentum equation, the density of the gas is included in the continuity equation.

$$\frac{\partial}{\partial t}(\rho_l(1-\alpha) + \rho_g \alpha) + \nabla \cdot (\rho_l(1-\alpha)\mathbf{u}_l + \rho_g \alpha \mathbf{u}_g) = 0 \tag{2.30}$$

The velocity of the gas consists of three terms, i.e., the liquid velocity, the slip velocity, and the drift velocity. The slip velocities are described in section 2.3.7.

$$\mathbf{u}_g = \mathbf{u}_l + \mathbf{u}_{\text{slip}} + \mathbf{u}_{\text{drift}} \tag{2.31}$$

With the above equations and with the right boundary conditions, the momentum and continuity equation can be calculated.

Parameter	Properties	Dimensions
$\mathbf{u}_l$	velocity vector liquid	$\frac{m}{s}$
$\mathbf{u}_g$	velocity vector gas	$\frac{m}{s}$
$\mathbf{u}_{\text{slip}}$	velocity vector slip	$\frac{m}{s}$
$\mathbf{u}_{\text{drift}}$	velocity vector drift	$\frac{m}{s}$
P	Pressure	$\frac{kg}{m \cdot s^2}$
α	Volume fraction gas	
ρ_l	Density liquid	$\frac{kg}{m^3}$
$\mathbf{g}$	Gravity vector	$\frac{m}{s^2}$
$\mathbf{F}$	Volume force	$\frac{N}{m^3}$
μ_l	Dynamic viscosity liquid	$Pa \cdot s$

Table 2.6: Parameters used in the Bubbly flow model.

2.4.2. Transport of diluted species

Another additional phenomenon is that the layer in the proximity of the electrodes becomes supersaturated with dissolved gas. This layer of dissolved gas will influence the size of the bubbles and thus the behavior of the bubbles. To take this effect into account, transport or diluted species is used. This will allow me to calculate the concentration field of a dilute solute in a solvent. The transport of dilute species models the transport of species by the convection-diffusion equation, which is shown in equation (2.32). Two types of driving forces are at work here, transport by diffusion and transport by convection. The transport by diffusion is determined with Fick's law, and the transport by convection is coupled to the flow field calculated by the Bubble flow model.

$$\frac{\partial c_i}{\partial t} - D\nabla^2 c_i + \mathbf{u} \cdot \nabla c_i = -\frac{M_{lg}}{M_i} \tag{2.32}$$

The mass transfer rate (sink term) from liquid to gas is included.

$$M_{lg} = k(c_i - c_s)M_i a \tag{2.33}$$

Henry's law gives the equilibrium concentration c_s of a gas dissolved in a liquid, this is shown in equation (2.34) [10]. The constant used in Henry's law depends on the composition of the solution. Therefore, the solubility of oxygen in an electrolyte (aqueous KOH solution) is different from that in water [29]. This is corrected with the Sechenov equation, which relates the concentration of the salt solution to that of pure water. The Sechenov equation can be found in appendix A.1.

$$c_s = \frac{P}{H_{\text{salt}}} \tag{2.34}$$

The mass transfer coefficient is determined by empirical relationships mentioned in section 2.3.6. By coupling the convection-diffusion equation to the equation from the bubble flow model, the concentration field of dissolved gas can be determined.

Parameter	Properties	Dimensions
$\mathbf{u}$	Velocity vector	$\frac{m}{s}$
D	Diffusion coefficient	$\frac{m^2}{s}$
c_i	Concentration of species	$\frac{mol}{m^3}$
M_i	Molecular weight of species	$\frac{kg}{mol}$
H_{salt}	Henry's constant	$\frac{Pa \cdot m^3}{mol}$
c_s	Saturation gas concentration	$\frac{mol}{m^3}$
k	Mass transfer coefficient	$\frac{m}{s}$
M_{lg}	Mass transfer rate	$\frac{kg}{m^3 \cdot s}$
P	Pressure	$\frac{kg}{m \cdot s^2}$
a	Interfacial area per volume	$\frac{m^2}{m^3}$

Table 2.7: Parameters used in the transport of diluted species model.

3

Modeling

In this chapter, the modeling of a vertical channel is briefly discussed. First, the geometries used are introduced. Next, the assumptions and boundary conditions corresponding to the geometries are explained. This is also done for the transport of diluted species. Subsequently, a comparison is made between the Bubbly flow, Mixture, and Euler-Euler model. These results are compared with the experimental data from Boissonneau et al. [5]. Finally, the mesh dependency study is discussed.

3.1. Geometry channel

Three different computational geometries are used in this thesis. These are based on experimental setups. The different computational geometries are shown in figure 3.1, it should be noted that these geometries are not drawn to scale. The first geometry is identical to the simulation performed by Schillings et al. [43]. He based his simulation on the experiment of Boissoneau et al. [5] and is shown in figure 3.1a. The second geometry is equal to the experiment performed by Hreiz et al. [19] and is shown in figure 3.1b. The third geometry is comparable to the experiment performed by Lee et al. [31] and is shown in figure 3.1c. Each geometry is briefly introduced below:

- The first geometry is used to compare the different models (e.g., Bubbly flow model, Mixture model, and Euler-Euler model). It is also used to verify slip velocities mentioned in chapter 2.3.7. This is done by comparing the simulated velocity profiles with the experimental velocity profiles reported by Boissoneau et al. They conducted the experiments using a natural circulation of the electrolyte. Schillings mimicked this by imposing a small electrolyte inlet flow. This will allow the use of a vertical channel, shown in figure 3.1a. The inlet of the channel, where no gas evolution occurs, was included to allow the flow to develop without bubble interference.

- The second geometry is used to visualize bubble behavior like bubble growth, velocity, and particle pathlines. The bubble growth and particle pathlines are used to identify the concentration of dissolved gas. The concentration of dissolved gas found in the experiment is used to verify the concentration field of dissolved gas calculated by COMSOL. This experiment was also performed in a vertical channel, shown in figure 3.1b, also called a no net flow design (definition by Hreiz et al. [19]). The free surface prevents the liquid from creating a net flow. However, the bubbles can escape at the free surface. On both sides of the channel, oxygen evolution takes place, the hydrogen evolving electrodes are placed outside of the vertical channel. This will lead to inhomogeneous current distributions, as ions must travel a longer path to the top of the electrode.

- The third geometry is used to verify the bubble layer simulated by COMSOL. The experiment was again performed in a vertical channel, shown in figure 3.1c. The third geometry is a forced convection design (definition by Hreiz et al. [19]).

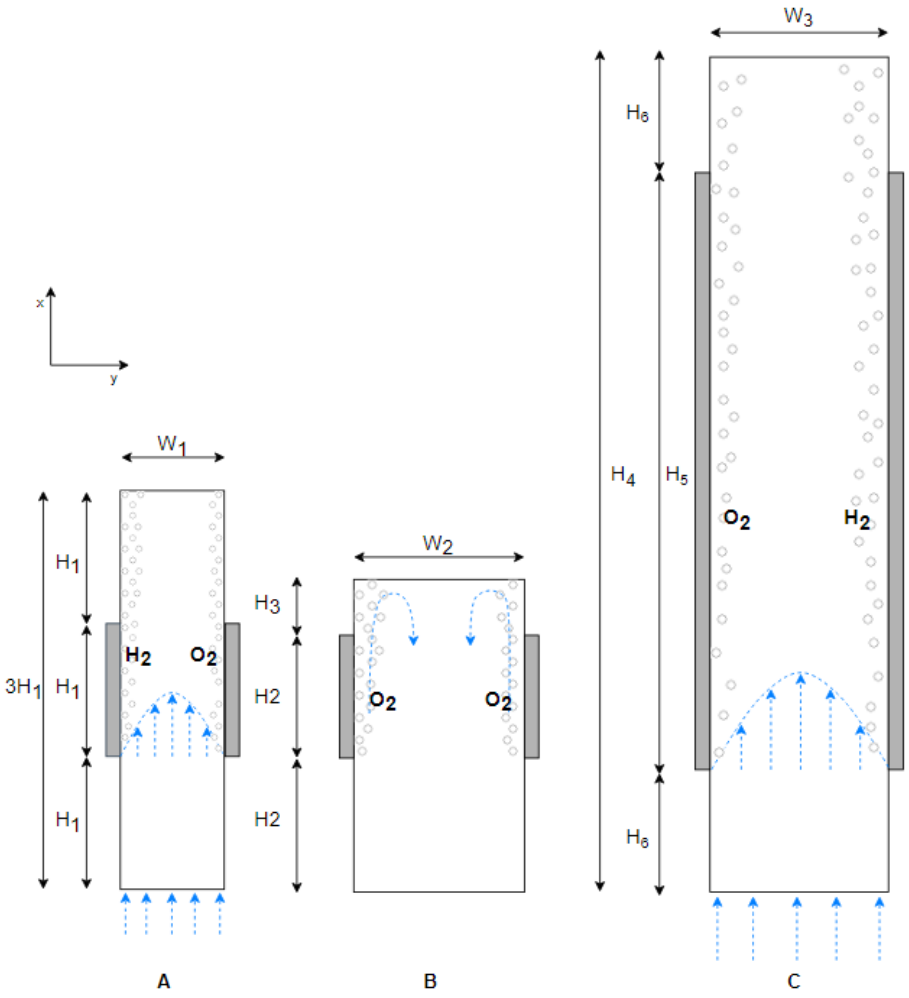

Figure 3.1: Three different geometries used in the simulations are based on the geometries reported by Schillings [43] (And Boissoneau and Byrne [5]), Hreiz [19] and Lee [31] respectively. It should be noted that these geometries are not drawn to scale.

Parameter	Value	Dimensions	Parameter	Value	Dimensions
H_1	40	mm	H_6	40	mm
H_2	38	mm	W_1	3	mm
H_3	10	mm	W_2	6	mm
H_4	220	mm	W_3	5	mm
H_5	180	mm			

Table 3.1: The dimensions of the different geometries.

3.2. Assumption bubble flow model

This section presents a range of assumptions and simplifications that can be applied to reduce the computational effort associated with the CFD analysis of water electrolysis. These assumptions are listed below:

- The flow is Newtonian and incompressible.
- The flow is considered isothermal (constant fluid properties).
- No correction of the gas fraction to the viscosity of the liquid.
- The flow is considered laminar since the Reynolds number is below the critical level (Re < 1200) [37].
- The current density distribution along the electrode is taken as uniform (except in the case of the experiments performed by Hreiz et al.).
- The vertical channel is modeled in 2D.
- Bubble coalescence is neglected.

3.3. Boundary conditions Bubbly flow model

When solving the momentum and continuity equation, the appropriate initial conditions and boundary conditions must be applied. These conditions are inflow conditions, wall boundary conditions, outflow conditions, etc. In the case of the first geometry (shown in figure 3.1a). The boundary conditions for the two other geometries can be found in appendix A.7. The inlet boundary condition was set to a normal inlet velocity:

$$\begin{array}{ll} u_{lx} = 0.06\ \mathrm{m/s} & \text{for } 0 \le y \le W_1, \quad \text{and } x = 0 \\ u_{ly} = 0\ \mathrm{m/s} & \text{for } 0 \le y \le W_1, \quad \text{and } x = 0 \end{array} \tag{3.1}$$

The outlet boundary condition describes the conditions at the boundaries where the fluid exits the domain. In this case a pressure outlet condition was used:

$$p_{out} = 0 \quad \text{for } 0 \le y \le W_1, \quad \text{and } x = 3H_1 \tag{3.2}$$

Wall boundary conditions are used to describe the fluid-solid interface. In viscous flows, the no-slip boundary condition is enforced at walls, meaning the tangential is zero. This results in the following wall boundary conditions:

$$\begin{array}{lll} \mathbf{u}_l(x,y) = 0\ \mathrm{m/s} & \text{for } 0 \le x \le H_1 \text{ and } 2H_1 \le x \le 3H_1, & \text{and } y = 0 \\ \mathbf{u}_g(x,y) = 0\ \mathrm{m/s} & \text{for } 0 \le x \le H_1 \text{ and } 2H_1 \le x \le 3H_1, & \text{and } y = 0 \end{array} \tag{3.3}$$

$$\begin{array}{lll} \mathbf{u}_l(x,y) = 0\ \mathrm{m/s} & \text{for } 0 \le x \le H_1 \text{ and } 2H_1 \le x \le 3H_1, & \text{and } y = W_1 \\ \mathbf{u}_g(x,y) = 0\ \mathrm{m/s} & \text{for } 0 \le x \le H_1 \text{ and } 2H_1 \le x \le 3H_1, & \text{and } y = W_1 \end{array} \tag{3.4}$$

Based on Faraday's law, the gas flux leaving the electrodes can be determined. The gas flux on the cathode side can be calculated with equation (A.22). For the anode side, the gas flux is determined with equation (A.23). The symbols used in equations (A.22) and (A.23) are listed in table A.4

$$N_{H2}(x, y = 0) = \frac{1}{2}\frac{R_{\text{universal}}Tj}{PF} \text{ for } H_1 \leq x \leq 2H_1 \tag{3.5}$$

$$N_{O2}(x, y = W_1) = \frac{1}{4}\frac{R_{\text{universal}}Tj}{PF} \text{ for } H_1 \leq x \leq 2H_1 \tag{3.6}$$

Parameter	Properties	Dimensions
$R_{\text{universal}}$	Universal gas constant	$\frac{J}{mol \cdot K}$
p	Pressure	Pa
F	Faraday's constant	$\frac{C}{mol}$
T	Temperature	K
j	Current density	$\frac{A}{m^2}$
$\mathbf{u}_l$	velocity vector liquid	$\frac{m}{s}$
$\mathbf{u}_g$	velocity vector gas	$\frac{m}{s}$

Table 3.2: Parameters used in the boundary conditions for the Bubble flow model.

3.4. Computational setup for the transport of diluted species

As mentioned previously, the electrolyte near the electrodes quickly becomes enriched with dissolved gases, which locally reaches supersaturation. This will affect the size of the bubbles since mass transport will take place. In order to account for this growth, transport of diluted species has been added to the simulations. The computational setup is schematically shown in figure 3.2.
The channel is divided into two sections, the adherence region, and the bulk region. In the adherence region, bubbles stick to the electrode. The fluid around these bubbles is in motion, also the bubble growth itself introduces advective transport. However, the advective transport introduced by bubble growth itself and the fluid around these bubbles is assumed to be small. Therefore, it was decided to simulate bubble growth in the adherence region by means of diffusion. Outside the adherence region, the bulk region begins, here the fluid is in motion. Since the fluid is in motion, two mechanisms for mass transport are at work. One of these is the convective transport of a species by the bulk motion of the fluid, and the other is the transport by diffusion. The different mass transfer coefficients are indicated in figure 3.2.
The electrodes are present on both sides of the channel, here (at the electrode surface) the dissolved gas is injected. The concentration of dissolved gas is set as a Dirichlet boundary condition, based on the experimental data from Shibata et al. [45], [47]. Together with the sinks in the adherence and bulk region, the concentration field could be established. This is indicated in figure 3.2, as the red line. Using the concentration field and the particle pathline, the bubble growth could be calculated using equation (2.13).

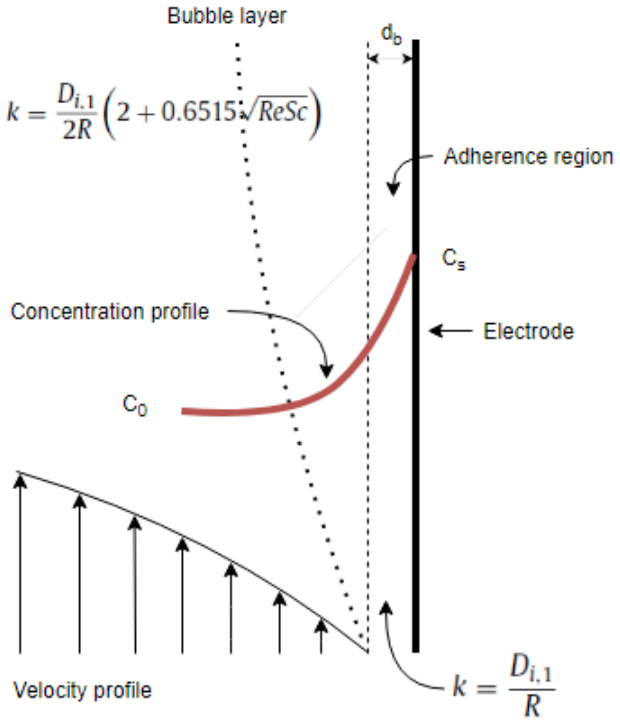

Figure 3.2: Computational setup for the transport of diluted species

3.5. Assumption transport of diluted species

To simplify the transport of diluted species model, several assumptionscan be made. These assumptions are listed below:

- The concentration of the diluted species on the electrode surface was determined from the experiments of Shibata et al. [47], [45] .
- In the adherence region the fluid is stagnant.
- 99% of the gas is injected in dissolved form at the surface of the electrode.
- 1% of the gas is injected in gaseous form at the surface of the electrode (results in faster simulation convergence).

3.6. Boundary conditions transport of diluted species

The boundary conditions used to compute the concentration field of dissolved gas are listed below. The concentration of dissolved gas can be simulated in two different ways. The first way is by applying a certain (depending on current density) flux to the electrode surface. The flux boundary condition can be described as follows:

$$-\mathbf{n} \cdot (-D\nabla c) = J_i \quad \text{for } H_2 \leq y \leq 2H_2, \quad \text{and } x = 0 \,\&\, W_2 \tag{3.7}$$

The second way is to impose a Dirichlet boundary condition on the surface of the electrode. This boundary condition is based on the experimental data of Shibata et al. During this thesis the Dirichlet boundary condition was used in the simulations.

$$c_i = c_{0,i} \quad \text{for } H_2 \leq y \leq 2H_2, \quad \text{and } x = 0 \,\&\, W_2 \tag{3.8}$$

No-flux boundary condition is used on boundaries over which there is no mass flux:

$$\begin{aligned} -\mathbf{n} \cdot \mathbf{J}_i &= 0 \quad \text{for } 0 \leq y \leq H_2 \text{ and } 2H_2 \leq y \leq (2H_2 + H_3), \quad \text{and } x = 0 \,\&\, W_2 \\ -\mathbf{n} \cdot \mathbf{J}_i &= 0 \quad \text{for } 0 \leq y \leq H_2 \text{ and } 2H_2 \leq y \leq (2H_2 + H_3), \quad \text{and } x = 0 \,\&\, W_2 \end{aligned} \tag{3.9}$$

Parameter	Properties	Dimensions
J	Inward flux	$\frac{mol}{m^2 \cdot s}$
$\mathbf{n}$	Normal vector	
$c_{0,i}$	Concentration of species	$\frac{mol}{m^3}$
D	Diffusion coefficient	$\frac{m^2}{s}$

Table 3.3: Parameters used in the boundary conditions for the transport of diluted species model.

3.7. Comparison between the bubbly flow, mixture and Euler-Euler model

The Bubbly flow, Mixture, and Euler-Euler model can all describe the behavior of multi-phase flows. The three models each have strengths and weaknesses. The Bubbly flow model for example, is suitable for gas bubbles in liquids (only for small gas fractions). However, the model is only valid when the dispersed phase has a density much smaller than the continuous phase.
The Mixture model is similar to the Bubbly flow model, but it takes into account the densities of both phases. It is often used for modeling solid particles, liquid droplets, or gas bubbles dispersed in a liquid phase. The Bubbly flow model is preferred over the Mixture model when it comes to gas bubbles in a liquid [10].
The Euler–Euler model is the most accurate dispersed multiphase flow model. Since it defines one set of Navier–Stokes equations for each phase. However, it is also relatively difficult to work with and requires good initial conditions to get convergence in the numerical solution.
The Bubbly flow model and the Mixture model both use the same slip velocities mentioned in chapter 2.3.7. The Euler-Euler model does not operate with slip velocities, therefore volume forces are used, which can be found in appendix A.4. The physical properties used in the three different models are shown in table 3.4. These parameters are consistent with the operating conditions reported in the work of Boissonneau et al.

Parameter	Properties	Value	Dimensions
ρ_l	Density	1040	$\frac{kg}{m^3}$
p	Pressure	100	kPa
ν_l	Kinematic viscosity	0.997	$\frac{m^2}{s}$
T	Temperature	298	K
j	Current density	1000	$\frac{A}{m^2}$
R_b	Bubble radius	22+10 $\frac{x-H_1}{H_1}$	μm

Table 3.4: Operating conditions based on the experiments of Boissonneau et al.

Figures 3.3 and 3.4 show the simulation results based on the experiment performed by Boissoneau. The blue dots represent the experimental data, the red line is the result of the simulation with the Euler-Euler model, the green line is the result of the simulation with the Bubbly flow model, and the cyan line is the result of the simulation with using the mixture model.

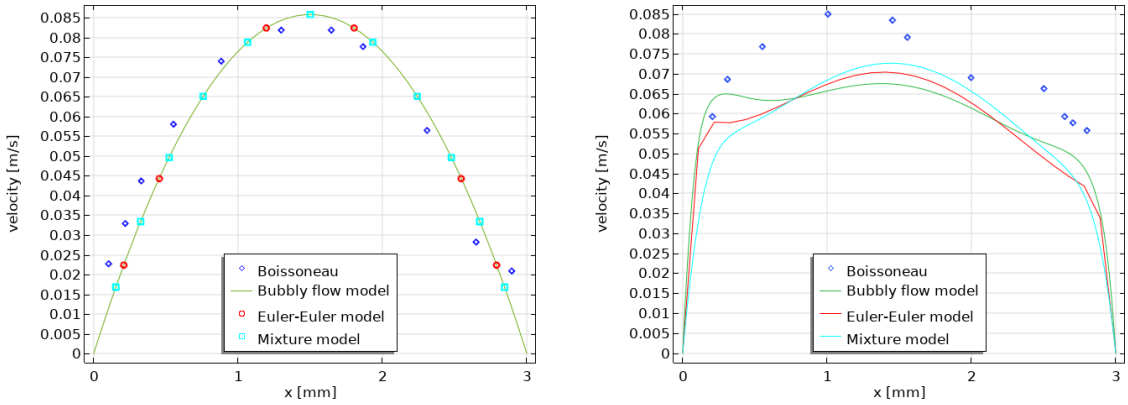

(a) Comparison of the liquid velocity profile at 35 mm

(b) Comparison of the liquid velocity profile at 60 mm

Figure 3.3: Simulation results of the different models based on the experiment performed by Boissoneau, at a current density of 1000 A/m^2. Hydrogen production takes place on the left and oxygen production on the right.

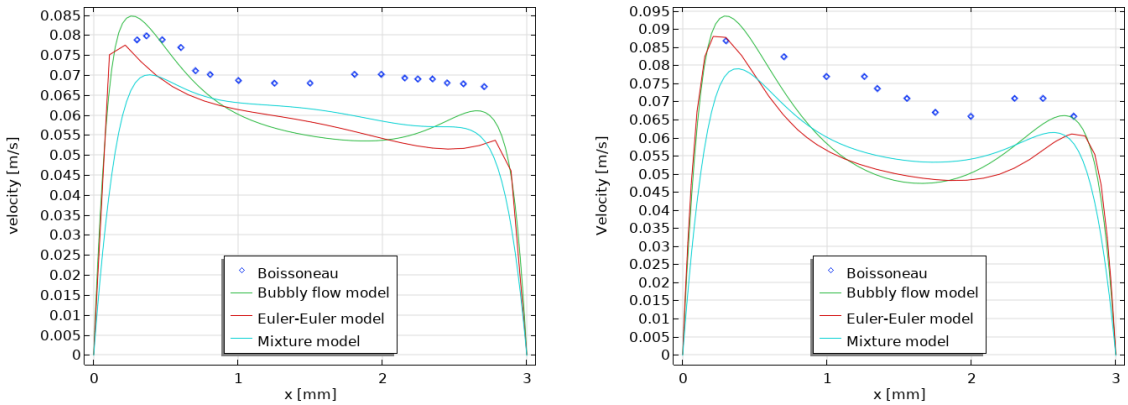

(a) Comparison of the liquid velocity profile at 70 mm

(b) Comparison of the liquid velocity profile at 85 mm

Figure 3.4: Simulation results of the different models based on the experiment performed by Boissoneau, at a current density of 1000 A/m^2. Hydrogen production takes place on the left and oxygen production on the right.

When comparing the Bubbly flow, Mixture, and Euler-Euler model the results are similar. However, there are some differences. Firstly, the Mixture model shows less accuracy near the walls in comparison with the other two models. This is because the Mixture model uses the density of the mixture based on the fraction of the local dispersed and continuous phase, affecting the momentum equation differently. While the Bubbly flow uses only the continuous phase for the fluid density and the Euler-Euler model uses each phase independently. Secondly, the Mixture model shows more accuracy in the middle part the channel. In table 3.5 a comparison is made between the computational cost of the different models.

Model	Computational cost	Mesh size	Study
Bubbly flow model	$\approx$ 14 min	150x200 elements (3mm x 40mm)	Time dependent study
Mixture mode	$\approx$ 19 min	150x200 elements (3mm x 40mm)	Time dependent study
Euler-Euler model	$\approx$ 5min	150x200 elements (3mm x 40mm)	Steady state study

Table 3.5: Overview of the computational cost for the different models.

One of the advantages of the Euler-Euler model is that it is possible to run the simulation in a steady state study, resulting in low computational costs. The Bubbly flow and mixture model do not converge to a solution in a steady-state study. Therefore, the Bubbly flow and mixture model must be performed in a time dependent study (simulation run until it has reached a steady state). This impacts the computational costs of both models, resulting in higher computational costs. One of the drawbacks of the Euler-Euler model is the convergence of the simulation when coupled with the transport of dilute species. Coupling the transport of dilute species with the Bubbly flow or Mixture model is not a problem. Several observations are listed below:

- In general, the Euler-Euler model is the most complete multi-phase model.
- The results of the Bubbly flow model and Euler-Euler model are quite identical.
- The Bubbly flow model is preferred over the Mixture model when it comes to gas bubbles in a liquid (according to COMSOL [10]). This is probably since that the Mixture model uses the average density of the mixture, which is determined based on the local gas and liquid fraction. As the gas fraction increases, the average density of the mixture decreases affecting the momentum equation. Therefore, under predicting the velocity of the bubbles.
- The Bubbly flow model and the Mixture model are the easiest to couple multiple extensions (called physics in COMSOL) such as particle trajectories and/or the transport of dilute species. Coupling multiple extensions to the Euler-Euler model caused convergence problems.
- Usually, the Euler-Euler model has the highest computational cost. This is because the Euler-Euler model solves two equations (one for each phase), while the other models solve one equation. Resulting in a higher computational cost. In this case, the Euler-Euler model has the lowest computational cost. This is because the Euler-Euler model can be run in a steady state.

Based on the above observations, the Bubbly flow model was best suitable during this thesis. This is because the Bubbly Flow model allowed the coupling of multiple extensions (also possible in the Mixture model). In addition, the computational cost of the Bubbly flow model is about 35% less than the Mixture model. Moreover, COMSOL recommends using the Bubbly flow model over the Mixture model in a gas-liquid mixture [10].

3.8. Mesh dependency study

To establish the accuracy of the CFD solution, and to keep the computational costs low, the vertical channel was analyzed using the Bubbly flow model. The grid convergence study is performed by developing three different meshes: with a coarse, medium, and fine grid. In figure 3.5 the comparison between the different meshes is shown. The figure shows that the mesh is independent of the solution. Therefore, the coarse mesh is chosen, which keeps the computational cost low.

Mesh type	Mesh size	Computational cost
Coarse mesh	75x100 elements (3mm x 40mm)	≈ 7 min
Medium mesh	100x150 elements (3mm x 40mm)	≈ 11 min
Fine mesh	150x200 elements (3mm x 40mm)	≈ 14 min

Table 3.6: Overview of the computational cost for the three different models.

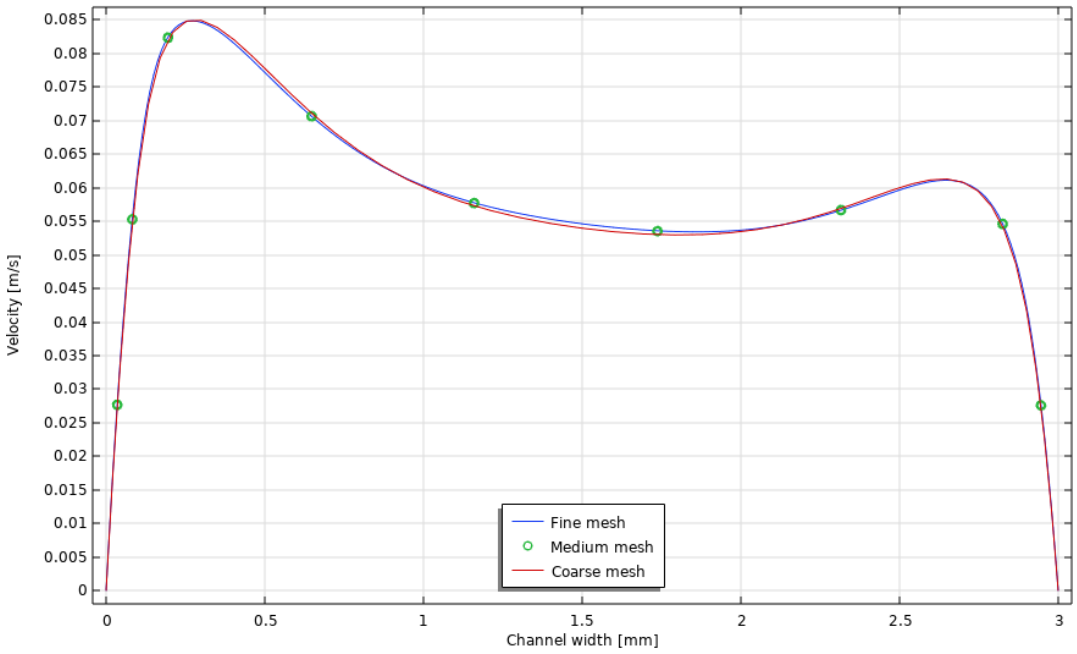

Figure 3.5: Mesh dependence study for the three different meshes

A mapped mesh was used as it is particularly powerful for 2D simulations. The greatest advantage of the mapped mesh is the control it provides over the element size, quality, and growth rate. The mapped mesh has been refined on the wall so that finer elements are obtained close to the walls. The refined mesh at the walls is needed because of the boundary layers that typically form a no-slip boundary condition. The anisotropic mesh is obtained by using distribution nodes, which controls the number of elements and their distribution along the wall. All elements have 90° angles, which means that the elements have no skewness, as shown in figure 3.6. The disadvantage of highly skewed elements (not the same as mesh size) is a decrease in accuracy and thus destabilization of the solution.

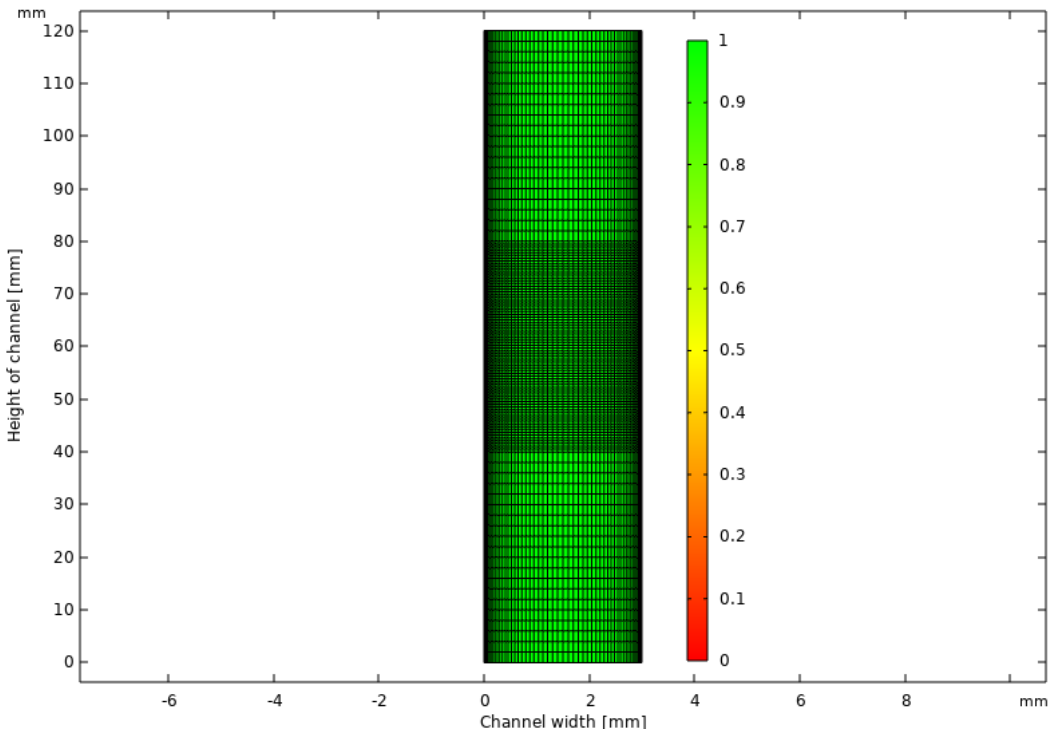

Figure 3.6: Skewness of the coarse mesh

4

Results

In this chapter, the results of the simulations will be discussed and analyzed. The Bubbly flow model is used for these simulations and is based on the experimental set-ups mentioned in chapter 3. The videos of the experiments performed by Hreiz, were used to analyze the behavior of the bubbles [19]. The experiments performed by Lee et al. are used to verify the shape and thickness of the bubble layer [31].

4.1. Results bubble layer fixed bubble diameter

To simulate the bubble layer, the Bubbly flow model was used together with the slip velocities mentioned in chapter 2.3.7. The computational geometry and boundary conditions are described in chapter 3.1 and 3.3. For the first case, the experimental work of Lee et al. was used. He performed these experiments in a potassium hydroxide solution (0.833 wt %) with an Ir/Ru alloy (Iridium-Ruthenium) for the electrodes. The electrode surface conditions are unknown. The physical properties are listed in table 4.1 and correspond to the operating conditions in the work of Lee et al.

Parameter	Properties	Value	Dimensions
ρ_l	Density	1040	$\frac{kg}{m^3}$
P	Pressure	100	kPa
ν_l	Kinematic viscosity	0.997	$\frac{m^2}{s}$
T	Temperature	298	K
R_b	Bubble radius	25	μm

Table 4.1: Operating conditions based on the experiments of Lee et al.

The simulation was performed with a forced electrolyte flow. The inlet boundary condition was applied as a uniform velocity profile of 0.18 m/s (Re = 900). The operating current density was set to 800 A/m^2 and the bubble size remains constant along the electrode. The size of the bubble was determined by taking the critical bubble diameter found by Zhang et al. [67]. He performed experiments in a 1 molar potassium hydroxide solution at a current density of 600 A/m^2. Which is slightly below the current density used in the simulations. Therefore, the critical bubble diameter will deviate slightly.
Figure 4.1 shows the simulation result of the development of the oxygen bubble layer along a vertical electrode. The orange dots are Lee's experimental data, and the blue line is the result of the simulation.

Lee determined the thickness of the bubble layer by averaging multiple images (reducing the fluctuating movement of the bubbles), then a reference image (just the water flow without the presence of bubbles) is subtracted from the obtained average image, resulting in the thickness of the bubble layer. The result of the simulation is compared with Lee's experimental data. In both cases, the thickness of the bubble layer increases along the vertical electrode. However, there are some noticeable differences, such as the thickness and shape of the layer. As can be observed in figure 4.1, the simulation predicts a larger dispersion of bubbles between 0 and 125 mm, while between 125 and 180 mm the dispersion of bubbles is underestimated. The criterion used to determine the thickness of the bubble layer in the simulation is explained in appendix A.6.

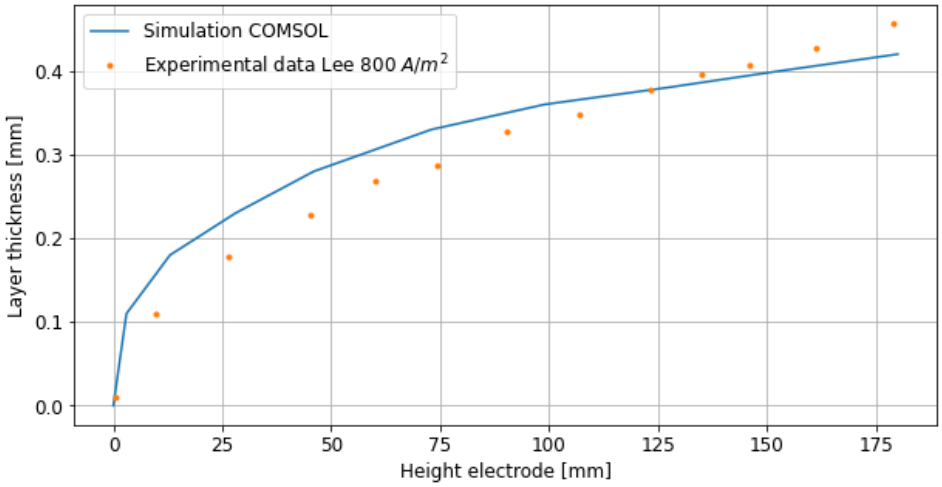

Figure 4.1: Development of the oxygen bubble layer thickness for a forced flow (Re = 900, 0.18 m/s), current density = 800 A/m^2 in a 0.833 wt% potassium hydroxide solution.

When both lines are plotted on a log-log plot, they appear as straight lines. This means that the lines have a relationship of the form $y = Ax^b$. The power corresponds to the slope of the line. Figure 4.2 shows both lines on a log-log plot, it becomes apparent that the shape of the simulated bubble layer does not match the shape of the bubble layer found in experiments. The simulated bubble layer scales with a power of about 0.3, while the bubble layer found in the experiments scales with a power of 0.5.

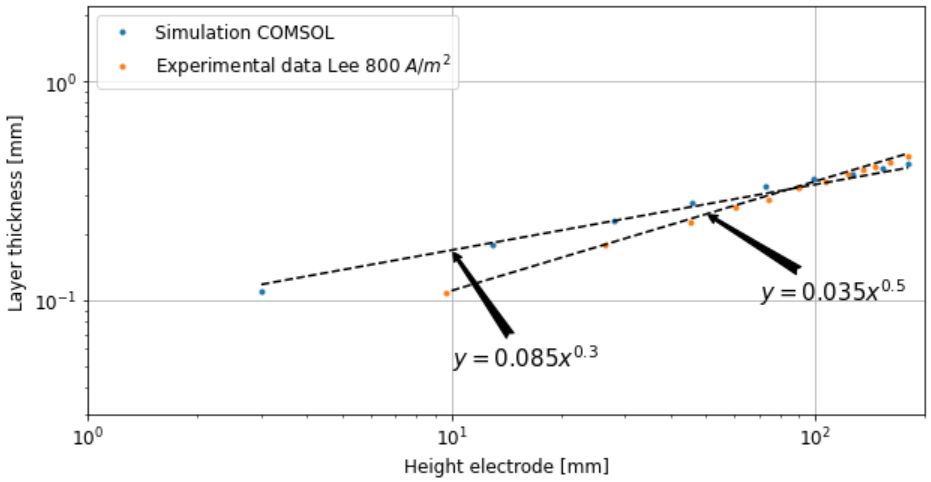

Figure 4.2: Development of the oxygen bubble layer thickness on a log-log plot for a forced flow (Re = 900, 0.18 m/s), current density = 800 A/m^2 in a 0.833 wt% potassium hydroxide solution.

The two graphs above show the dispersion of bubbles is not simulated properly. A possible cause could be that a constant bubble diameter cannot accurately describe the spread of a bubble. As re-

ported in chapter 2.3.3, the bubble size in the flow direction undergoes a significant increase in diameter. Therefore, it makes sense that the model cannot simulate the dispersion of bubbles correctly when using a constant bubble diameter.

4.2. Visualization of bubble behavior

4.2.1. Mean bubble size along with the height of the electrode

No experiments were conducted during this thesis. Therefore, the videos of the experiments performed by Hreiz were used to analyze bubble behavior. These experiments were conducted in a 0.5 molar a sodium hydroxide solution. The geometry of the channel is shown in figure 3.1. The physical properties are listed in table 4.2 and correspond to the operating conditions reported in the work of Heinz et al. The measurements and simulations covered in this section (4.2.1) all use the conditions described below.

Parameter	Properties	Value	Dimensions
ρ_l	Density	1022	$\frac{kg}{m^3}$
p	Pressure	100	kPa
μ_l	Dynamic viscosity	1.11	$mPa \cdot s$
T	Temperature	293	K

Table 4.2: Operating conditions based on the experiments of Heinz et al.

The experiment was conducted at an average current density of 130 A/m^2, with a no net flow configuration. It is worth noting that the anode is divided into segments, shown in figure 4.3.

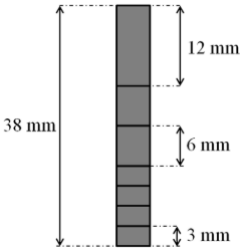

Figure 4.3: Composition of the segmented anode.

Each anode consisted in seven nickel pieces. As mentioned before, oxygen production takes place on both sides of the channel, the hydrogen evolving electrodes are placed outside the vertical channel. This setup will lead to an inhomogeneous current distribution, as ions must travel a longer path to the top of the anode. The current for each segment is shown in table 4.3.

Segment number	1	2	3	4	5	6	7
Current (mA)	84.04	38.3	9.98	6.47	4.94	2.55	4.13

Table 4.3: Experimentally measured average current at each anode segment under a 130 A/m^2 current density on the anodes. The width of each section is 30 mm.

The video used to analyze the average bubble size is split into two parts, the upper part, and the lower part. First, the video was split into a sequence of images. To extract data from these images, they were converted to grayscale images. A grayscale image is an image in which the value of each pixel represents an amount of brightness. Since the bubbles in this sequence of images are dark, the algorithm was set to recognize dark features instead of light features. Next, the grayscale images shown in figure 4.4a were cropped to analyze the region of interest, corresponding to the red rectangle shown in 4.4b located right next to the electrodes. Using the Trackpy algorithm (Python package), the dark features are tagged, shown in figure 4.4c. The tagged bubbles are then stored in a DataFrame (extension of Pandas a Python package). In this DataFrame the size of the feature, frame number, brightness, roundness, x and y coordinates are stored.

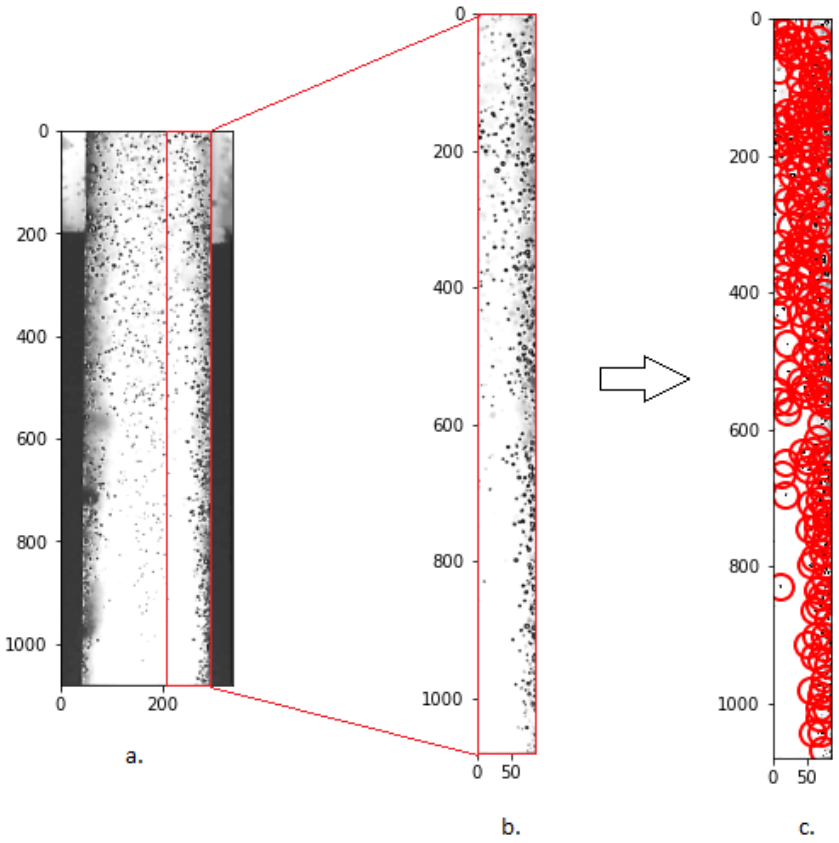

Figure 4.4: As an example, the upper part of the channel (the top 200 px no electrode is present) is used to visualize the algorithm. The first step is to select the region of interest, the second step is to detect all features and the last step is to tag all features and store them in a Dataframe. The scale of each pixel about 0.025 mm x 0.025 mm.

After filtering out the noise (such as extremely large bubbles), the algorithm will run over all the frames. In the case of Hreiz's video, a total of 120 frames were analyzed (10 frames per second). This resulted in more than 15000 features. It should be noted that the videos provided by Hreiz are 6 times slower than reality. Figure 4.5 represents the upper half of the channel while figure 4.6 represents the lower half of the channel. Figure 4.5 and 4.6 shows the size distribution along the vertical plane. Here each red dot represents a bubble. Since the spread in bubble size is large along the entire length of the electrode, a moving average is included. A moving average will smooth out short-term fluctuations and highlight longer-term trends, this is indicated by the blue line. It should be noted that the y-axis is inverted, so 0 px is the top of the channel and 1100 px is the bottom of the channel. From figure 4.5 and 4.6 the average bubble diameter increases in the flow direction. Which could be a verification of the observations made from flow visualizations mentioned in chapter 2.3.3. Another explanation could be the decrease in current density along with the height of the electrode. It has often been reported

that an increase in current density leads to smaller bubbles [17], [49]. However, the opposite has also been reported [23], [5], [19].

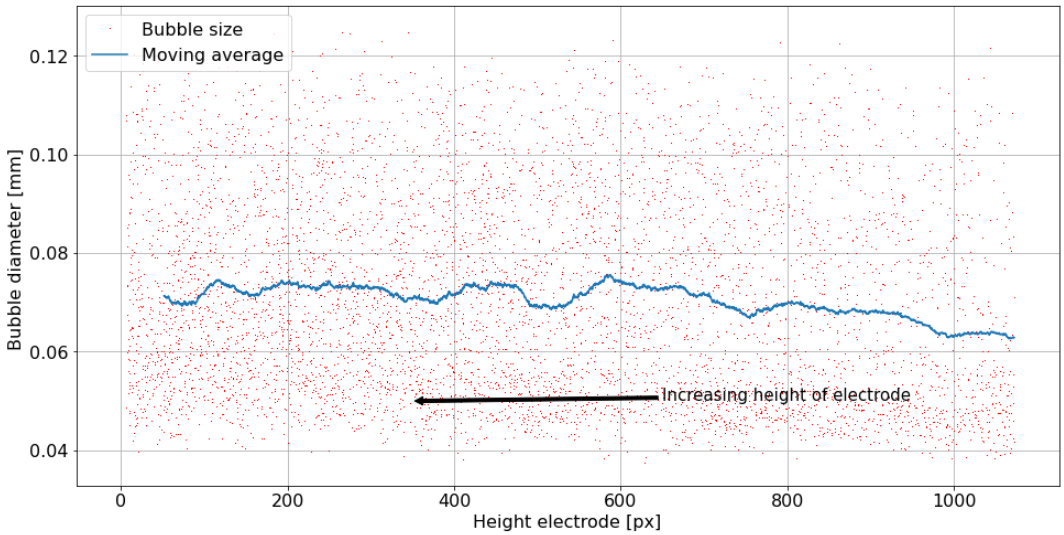

Figure 4.5: Result of the bubble size measurement for the upper half of the channel. The length of the upper part of the channel is approximately 1100 pixels, of which the first 200 pixels are without electrodes. The remaining 900 pixels correspond to 22.5 mm (15.5-38 mm).

The length of the lower half of the channel was shorted due to an obstruction affecting the algorithm.

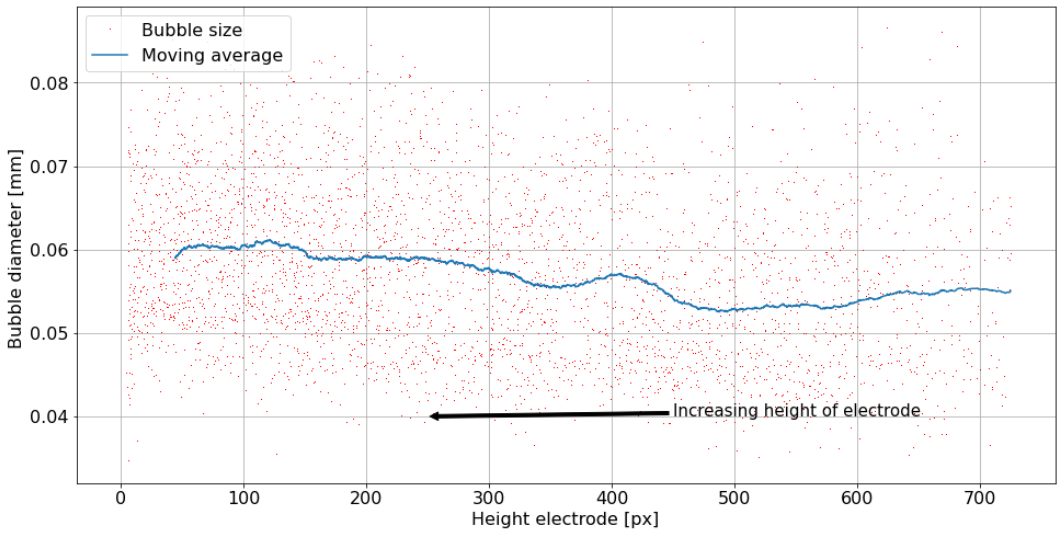

Figure 4.6: Result of the bubble size measurement for the lower half of the channel. The length of the lower part of the channel is approximately 1100 pixels and corresponds to 25 mm (0-25 mm). However, due to obstacles, the last 300 pixels are not included, which corresponds to the first 7.5 mm of the channel.

As shown in the figures above, the average bubble diameter starts at about 50 μm and ends at about 80 μm. This means about a 60% increase in size. It should be noted that there is a slight overlap in the videos made available by Hreiz. In the next section, individual bubbles were tracked to determine where this change in bubble size occurs.

4.2.2. Tracing individual bubbles

In the previous section, it was verified that the mean bubble size is not a constant along with the height of the electrode. According to several studies, this change in mean bubble size is due to mass transfer of dissolved gas [5], [19], [57]. To identify where in the channel the bubbles grow, individual bubbles were tracked. This was done at various locations in the channel. The images from the experiment conducted by Hreiz mention in section 4.2.1 were used to track bubbles. Multiple regions are discussed in this section to indicate where the tracked bubbles are located. These regions are the adherence region, the diffusion region, and the bulk region. The adherence region is the area adjacent to the electrode, which is approximately the thickness of a bubble diameter. Next is the diffusion region, which is located between the adherence region and the bulk region. The diffusion region has a thickness of approximately the bubble layer. Last is the bulk region, which is the area outside the bubble layer. Figure 4.7 shows the particle pathline of two different bubbles located at the lower part of the vertical channel. Here the green line corresponds to a bubble tracked in the bulk region and the blue line corresponds to a bubble tracked in the diffusion region.

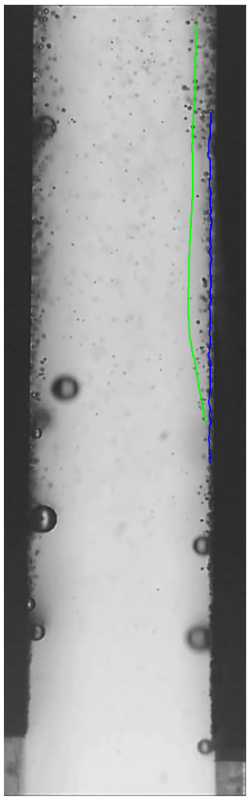

(a) Particle pathlines overlaid on the video.

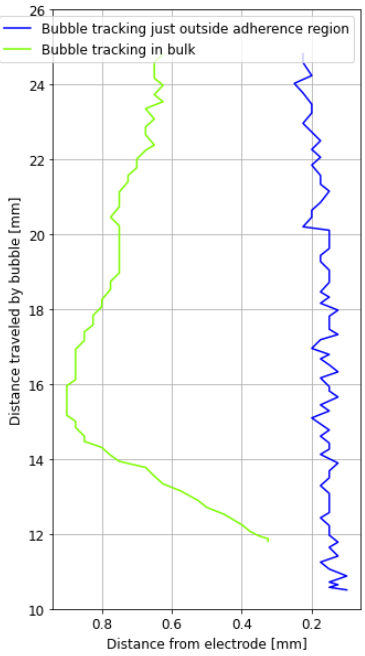

(b) Particle pathlines plotted in a graph. The sudden change of direction of the green bubble is probably due to the internal recirculation caused by the configuration of the cell (figure 2.2c).

Figure 4.7: The particle pathlines at two different locations for the lower half of the channel. The green line represents a bubble in the bulk region and the blue line represents a bubble in the diffusion region

Bubbles were also tracked in the upper part of the vertical channel, as shown in figure 4.8. As in the previous figure, the green line corresponds to a bubble being tracked in the bulk region and the blue line corresponds to a bubble being tracked in the diffusion region. All tracked particles show a dispersion away from the electrode.

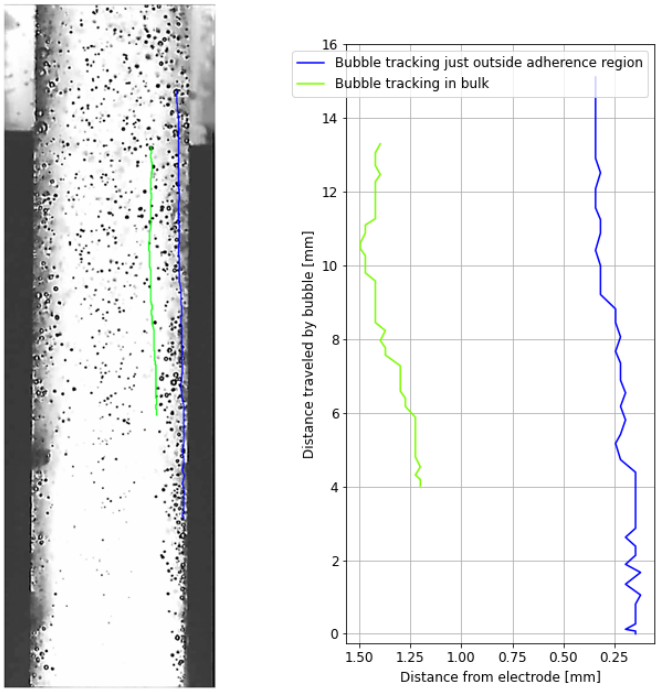

(a) Particle pathlines overlaid on the video.

(b) Particle pathlines plotted in a graph.

Figure 4.8: The particle pathlines at two different locations for the upper half of the channel. The green line represents a bubble in the bulk region and the blue line represents a bubble in the diffusion region

In figure 4.9 and 4.10, the behavior of the tracked bubbles is examined in more detail. The figure consists of two y-axes, the left y-axis shows the growth of the bubble and the right-hand y-axis indicates the position of the bubble relative to the electrode. The measuring technique is briefly explained in appendix A.8.

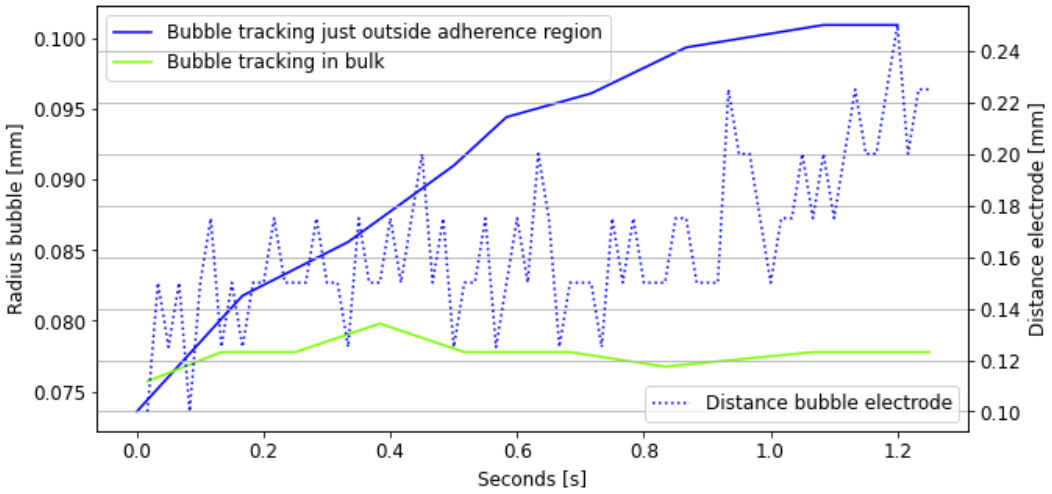

Figure 4.9: Change in bubble size corresponding to the two bubbles followed in figure 4.8. The secondary axis shows the position of the ”blue” bubble relative to the electrode.

The green and blue lines correspond to the same bubbles followed in figure 4.7, which is located in the lower part of the channel. As can be seen in the figure 4.9, the bubble closest to the electrode (blue line) undergoes significant growth due to mass transfer. I believe this growth spurt is due to the bubble’s proximity to the electrode. The bubble located in the bulk region (green line) does not change

significantly in size. This implies that the dissolved gas layer is quite thin and does not reach the bulk region, since no mass transfer takes place. To see a correlation between the change in bubble size and the proximity of the bubble to the electrode, both lines are plotted in figure 4.9. As can be observed, the rate of change in bubble radius strongly depends on its proximity. The closer the bubble is to the electrode, the more this bubble grows.
The behavior of the tracked bubbles for the upper part of the channel is shown in figure 4.10. The green and blue lines correspond to the same bubbles followed in figure 4.8. These bubbles have some similarities and differences with the bubbles tracked in the lower part of the channel. As illustrated in the figure 4.10, the bubble closest to the electrode (blue line) shows some growth. Although this bubble is in close proximity to the electrode, the growth rate is significantly lower than the growth rate observed in figure 4.9. This is probably due to the inhomogeneous current distribution caused by the electrode configuration. Therefore, the presence of dissolved gas in the upper part of the channel will be lower. The bubble located in the bulk region (green line) shows no growth. This reinforces our suspicion that the growth is due to the proximity of the bubble to the electrode.

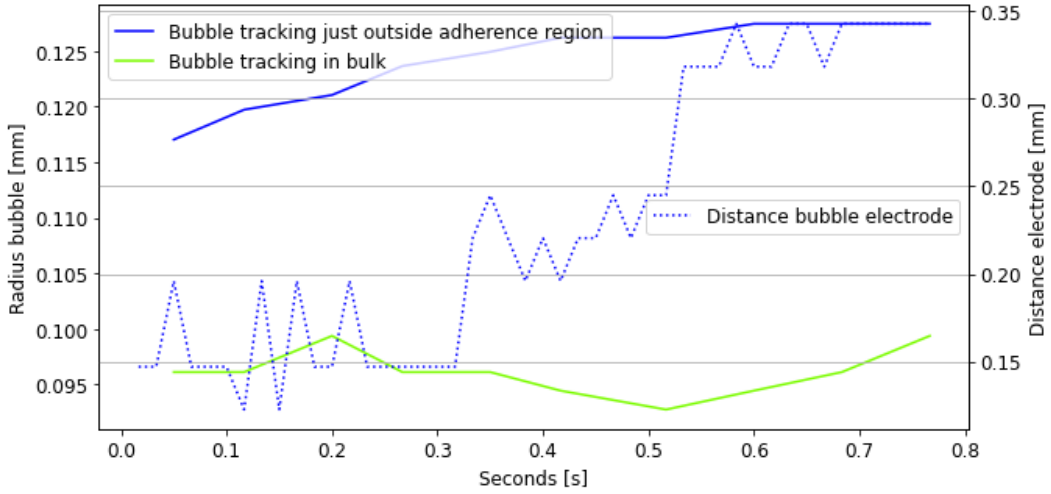

Figure 4.10: Change in bubble size corresponding to the two bubbles followed in figure 4.7. The secondary axis shows the position of the ”blue” bubble relative to the electrode.

The above measurements indicate that bubble growth only occurs in the vicinity of the electrode. Therefore, several more bubbles are evaluated in the vicinity of the electrode to give more strength to this hypothesis. The results of these measurements are shown in figure 4.11. Here each line is an individual bubble. The measurements of these bubbles were all made at a distance between 0.05 to 0.3 mm from the electrode surface. Several observations can be made from figure 4.11:

- All the bubbles show significant growth. However, the growth rate varies quite a bit. This has several causes, namely the variation in slip velocity of the bubbles, which are affected by neighboring bubbles. In addition, rising bubbles leave a wake of a lower concentration of dissolved gas. Which in turn affects the growth of the bubbles that follow/cross the wake of the previous bubble.

- Another observation is that bubble growth stops after it reaches a certain size. This is due to the dispersion forces, which are strongly dependent on the size of the bubble. As a result, a larger bubble will experience more dispersion, causing the bubble to exit the dissolved gas layer. Another explanation could be the inhomogeneous current density (decreases with height) along the height of the electrode. Therefore, the concentration of dissolved gas is expected to be lower, resulting in less growth as the bubble rises.

In appendix A.5, the bubble diameter versus distance from the electrode is plotted.

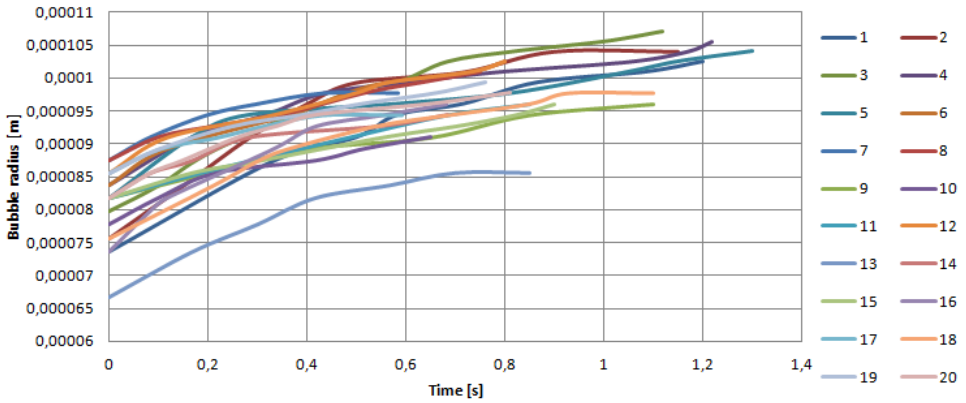

Figure 4.11: Change in bubble size over time for twenty randomly selected bubbles. The bubble measurements were taken from the video provided by Hreiz [19]

A correlation matrix is shown in figure 4.12, which is used to measure the correlation coefficients between variables. In this case, the correlation between the growth rate and the position of the bubbles is examined. The line of 1s running from top left to bottom right is the main diagonal, showing that each variable always correlates perfectly with itself. In addition, the matrix is symmetric and shows the same correlation above the main diagonal, which is a mirror image of the one below the main diagonal. The correlation between the Y-coordinate and growth rate is quite strong. There are several reasons for this:

- Depletion of dissolved gas.
- As the Y coordinate increases, so does the distance from the electrode and thus the concentration decreases, affecting the growth rate.

While the correlation between the X-coordinate and growth rate is rather weak. The weak correlation can also be attributed to the inhomogeneous current distribution.
As can be seen, the correlation coefficients between the position (X- and Y-coordinates) and the growth rate are negative. This means that as the X and Y coordinates increase, the growth rate will decrease.

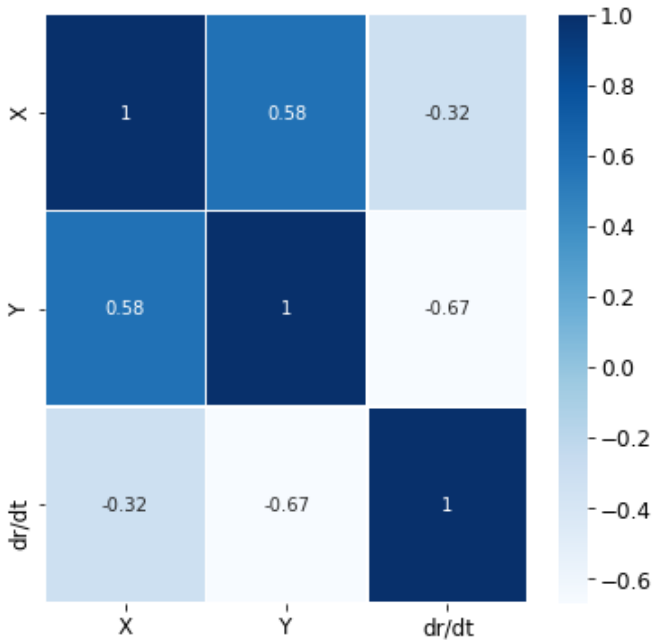

Figure 4.12: Correlation matrix for three different parameters, namely the x-position, the y-position and the change in bubble radius over time.

4.2.3. Concentration dissolved gas

The bubble growth curves, shown in figure 4.11, are used to determine the growth rate of each bubble. The growth rate is determined by dividing the change in bubble radius over a time interval. Figure 4.13 shows the change in bubble radius versus position relative to the electrode.

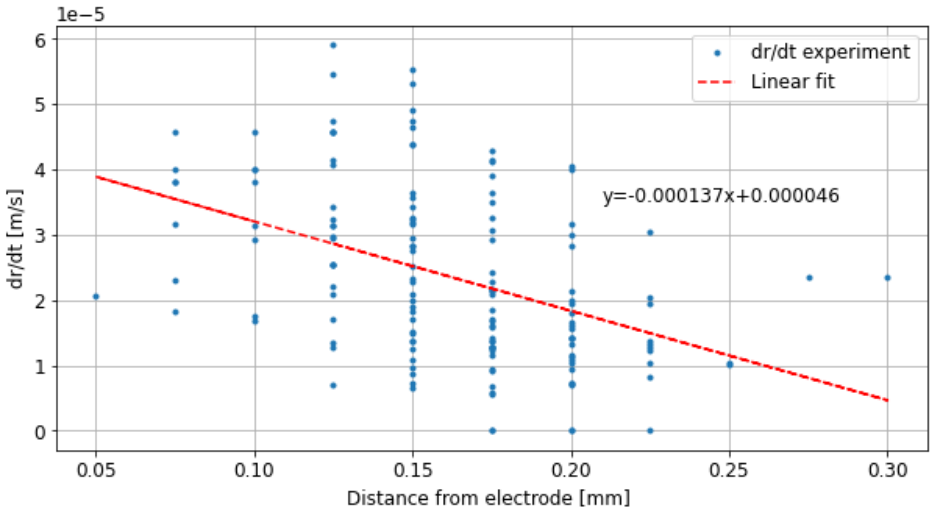

Figure 4.13: The change in bubble radius corresponding to the bubbles followed in figure 4.11. The equal distance between the measurements is due to the resolution of the images (the pixel size is 0.025 mm x 0.025 mm).

After the dr/dt has been determined together with the position of the corresponding bubble, the local concentration of dissolved gas can be calculated with equation (2.13) (for the mass transfer coefficient equation (2.14) was used). The following figure illustrates the concentration of dissolved gas based on the measured bubble growth. A total of 200 measuring points has been carried out, which are indicated by blue dots. The wide spread of the measured concentration levels is due to several reasons namely, the variation in slip velocity, the sharp decrease in current density along the electrode and depletion of dissolved gas by neighboring bubbles. In addition to the reasons mentioned above, measurement errors also play a role.

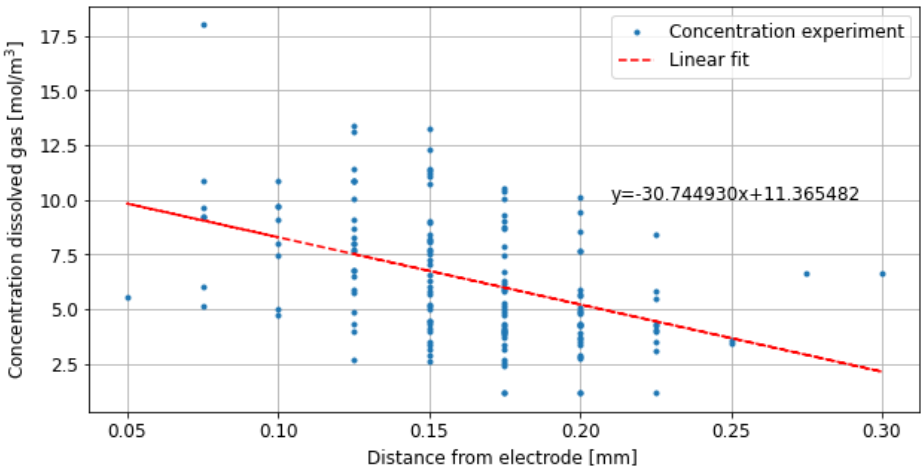

Figure 4.14: Concentration of dissolved gas corresponding to the bubbles followed in figure 4.11. The equal distance between because of the pixel size.

The concentration depicted in figure 4.14 shows a lot of scattering due to the reasons mentioned

above. For greater clarity, the upcoming figures are indicated by means of a color code. The figure below illustrates the coordinates where the measurements were taken. The color bar next to the figure indicates the concentration corresponding to those specific coordinates. It is clear from this figure that the concentration decreases sharply as the height increases. In addition, the concentration also seems to decrease as the distance from the electrode increases.

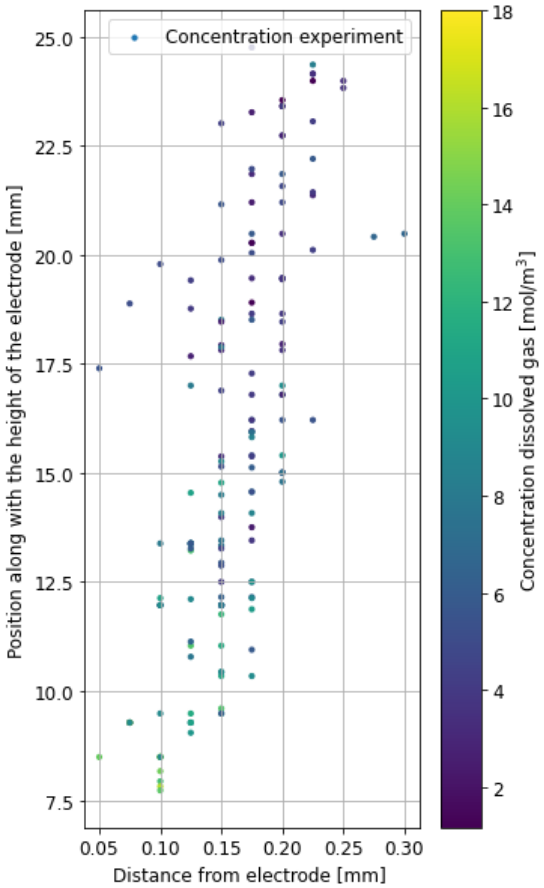

Figure 4.15: The location of the measurements, along with a color code for the dissolved gas concentration. The equal distance between because of the pixel size.

After the concentration of dissolved gas was determined by bubble growth measurements. Next, the concentration of dissolved gas is calculated by COMSOL. For this the convection-diffusion equation was used and is explained in chapter 2.4.2. It should be noted that the mass transport of the diluted species (sink term in the convection-diffusion equation) does not change the size of individual bubbles. However, it does increase the total gas fraction. The computational setup used in this simulation is described in chapter 3.4. For the wall boundary condition, the results of the experiments performed by Shibata et al. were used, which can be found in chapter 2.2. As mentioned before, the current density is not constant along the electrode, which affects the concentration of dissolved gas. Therefore, a different Dirichlet boundary condition is imposed on each segment, which is based on the measured current of each segment (table 4.3). The Dirichlet boundary condition along the electrode is shown in figure 4.16.

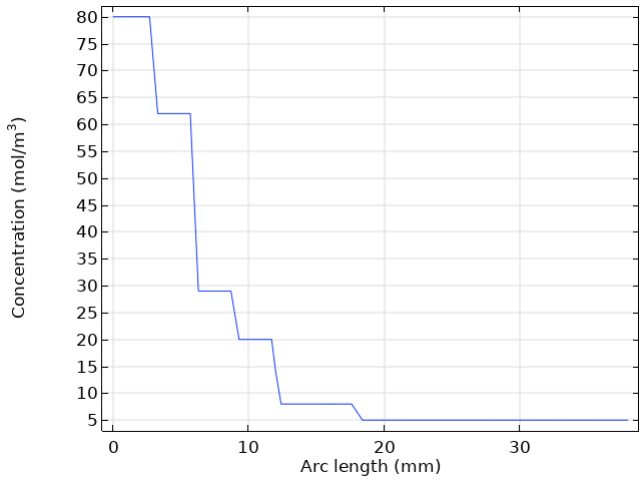

Figure 4.16: The Dirichlet boundary condition along the electrode is based on the experimental results of Hreiz [19].

The result of this simulation is shown in figure 4.17. Here the dashed lines indicate the concentration of dissolved gas and the blue solid line the gas fraction. The dashed line in red indicates the saturation level. From the graph it becomes clear that the dissolved gas layer is quite thin, also the concentration of dissolved gas changes along the height of the electrode due to the inhomogeneous current distribution. Another notable result is the increase in concentration as the distance from the electrode increases (for most of the heights). This is rather strange because it would mean that the dc/dy has a positive value, meaning the current density becomes negative as equation (4.1) shows. The reason for this is an artifact of the boundary condition used and is caused by advection of higher concentration electrolyte from below.

$$\frac{dc}{dy} = -\frac{j(x)}{2FD} \tag{4.1}$$

Moreover, according to the simulated concentration profile, the bulk region also becomes slightly oversaturated. This phenomenon was also reported by Vogt et al. [57]. The fact that the bulk also becomes slightly oversaturated is probably due to the internal recirculation, which is caused by the configuration of the channel. In a forced convection configuration, this phenomenon will be absent in simulations, due to the constant supply of ”clean” electrolyte. In reality, the forced convection configuration, will probably also become (over)saturated since the electrolyte will be recycled. In appendix A.9, the concentration results of Hreiz’s experiment are available.

Parameter	Properties	Dimensions
y	Distance	m
c	Concentration	$\frac{mol}{m^3}$
D	Diffusion coefficient	$\frac{m^2}{s}$
F	Faraday constant	$\frac{A \cdot s}{mol}$
j	Current density	$\frac{A}{m^2}$

Table 4.4: Parameters used in the equation (4.1).

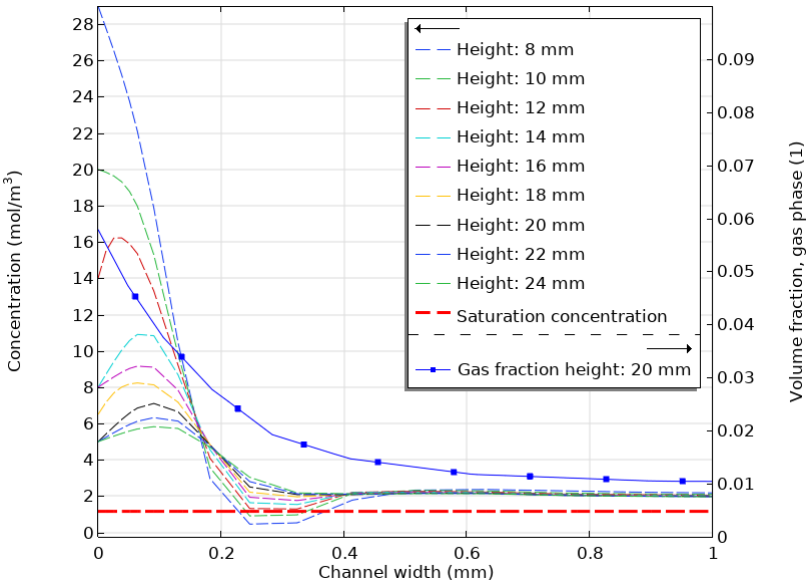

Figure 4.17: The simulated concentration profiles (dashed lines) for different heights based on the current distribution shown in table 4.3. The dip visible for the 0.35 mm is again due to the internal recirculation of the electrolyte. The gas fraction in indicated on the secondary y-axis.

Next, the concentration field of dissolved gas shown in figure 4.14 and figure 4.15 is compared with the concentration field simulated by COMSOL. Figure 4.18 shows this comparison. Here the blue and orange dotted lines are the simulated concentration profiles for two different heights and the red dashed line is the linear fit of the measured concentration. Knowing that the measurements are not 100% accurate, the dissolved gas concentration will therefore deviate from that of COMSOL. Another issue is the low number of measuring points before 0.05 and after 0.25 mm. Nevertheless, the concentration field found by COMSOL is quite close to the concentration field found in the measurements.

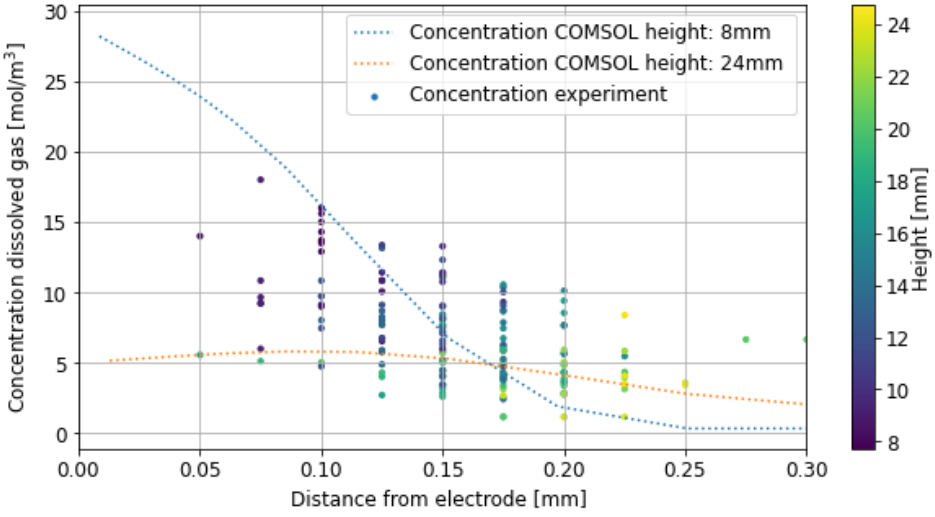

Figure 4.18: The concentration of dissolved gas found in the measurements is overlaid with the simulated concentration profiles (dotted lines) for two different heights.

Figure 4.19 shows a zoomed-in version of figure 4.17. Here the solid lines are the simulated concentration profile for different heights and the red dotted line is a polynomial fit of these solid lines. To simplify the calculations, the polynomial fit is used to approximate the concentration along the electrode.

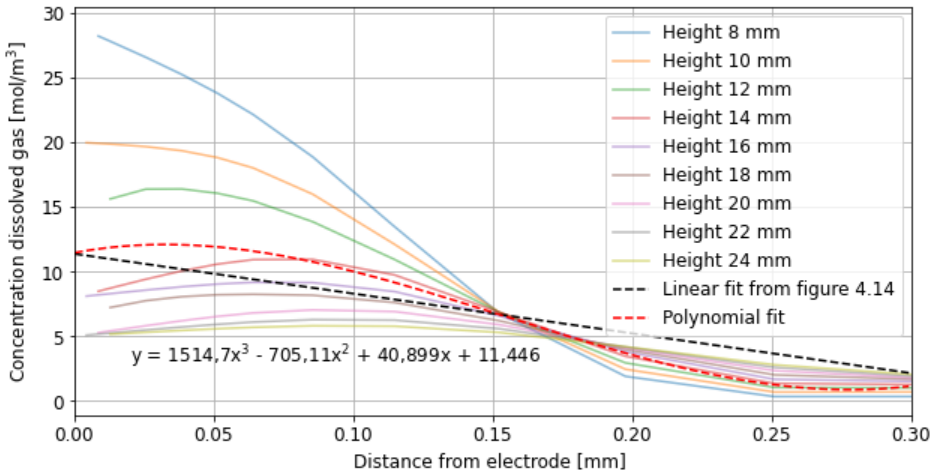

Figure 4.19: The simulated concentration profiles, between a height of 8 mm to 24 mm. The red dashed line is a polynomial fit of the simulated concentration profiles. The black dashed line is a linear fit from the measured concentration (figure 4.14).

4.2.4. Bubble growth

To calculate the bubble growth, the method discussed in chapter 2.3.6 is used. However, some adjustments have been made. Since the bubble rises in a non-uniform solution, the position of the bubble is important. Therefore, the particle pathline is needed to calculate the growth of the bubble. Figure 4.20 shows the pathline of 12 bubbles indicated with the dotted lines. The black solid line is the average path the bubbles travel and will be used as 'the average particle pathline' in the calculations. From the graph below, it becomes clear that the average pathline of the particles is rather unpredictable. Therefore, a linear fit is used to describe the average particle pathline. The position of the bubble relative to the electrode is described in equation (4.2).

$$x(t) = 0.0494t + 0.1285 \tag{4.2}$$

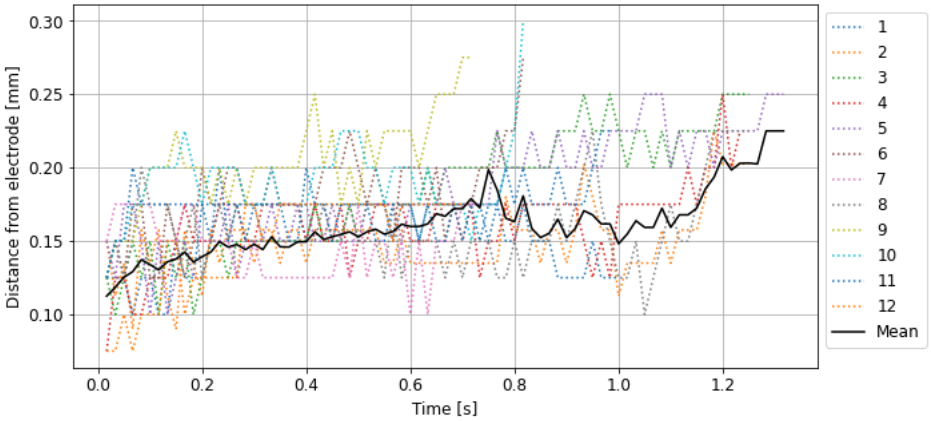

Figure 4.20: Particle pathline associated with the bubbles in figure 4.11 (the bubbles were tracked using the video provided by Hreiz [19]).

Figure 4.20 is re-plotted without the particle path lines of the individual bubbles. The red dashed line is the linear fit corresponding to the average particle pathline.

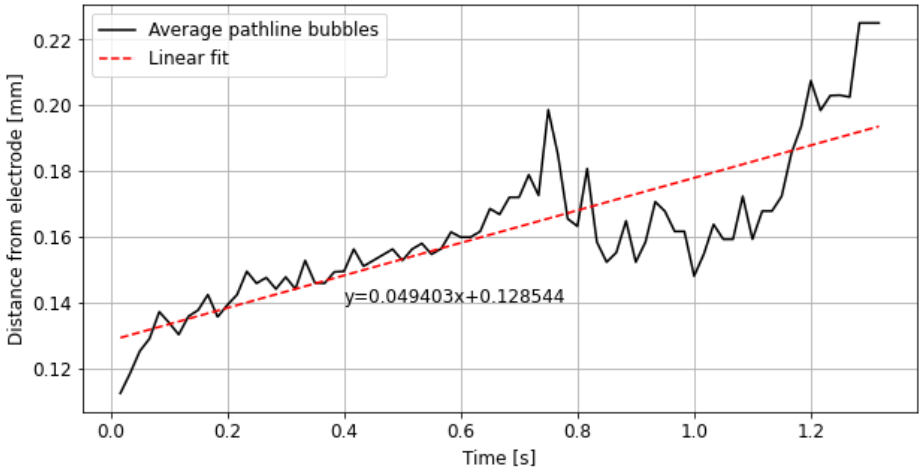

Figure 4.21: Linear fit corresponding to the average particle pathline.

Knowing the average particle pathline, which is a function of time, the next step is to determine the concentration at that particular position. This is done by taking the average concentration over a certain height (between 8-24 mm along the electrode). The average concentration can be described with equation (4.3) (polynomial fit from figure 4.19). Here the variable x stands for the distance to the electrode. Substituting equation (4.2) into equation (4.3) gives the concentration of dissolved gas as a function of time associated with the average particle pathline.

$$C(x(t)) = 1514.7x(t)^3 - 705.11x(t)^2 + 40.899x(t) + 11.446 \tag{4.3}$$

Next, the concentration of dissolved gas associated with the average particle pathline can be substituted in equation (4.4).

$$\frac{dR}{dt} = \frac{M_i}{\rho_g} k(C(x(t)) - C_s) \tag{4.4}$$

The k stands for the mass transfer coefficient, which can be determined using equation (4.5). As can be seen from the equation, the mass transfer is dependent on the slip velocity (difference between the velocity of the gas bubble and the liquid). However, the slip velocity is not known, but the velocity of the gas bubble itself is known. This is determined using PIV (Particle image velocimetry). The velocity of the gas bubbles was about 0.01 m/s. The velocity of the gas bubble is used as an indication of the slip velocity (assuming that the slip velocity is less than the velocity of the bubble itself). For the slip velocity, two velocities have been used, a ”low” slip velocity and a ”high” slip velocity (20% and 80% of the measured velocity obtained by the PIV).

$$k = \frac{D}{2R}(2 + 0.6515\sqrt{ReSc}) \tag{4.5}$$

The differential equation (4.4) has been solved and the result is shown in figure 4.22. The two red lines are the calculated bubble radii for two different slip velocities. The transparent lines are the measured bubble radii associated with figure 4.11. When comparing the red lines with the transparent lines, it is noticeable that the calculated bubble radii correspond reasonably well with the measured bubble radii. However, the growth rate of the measured bubbles between 0 and 0.2 seconds seems to deviate slightly from the calculated bubble radius. After the 0.2 seconds the calculated bubbles radius fits well with the measured bubble radii.

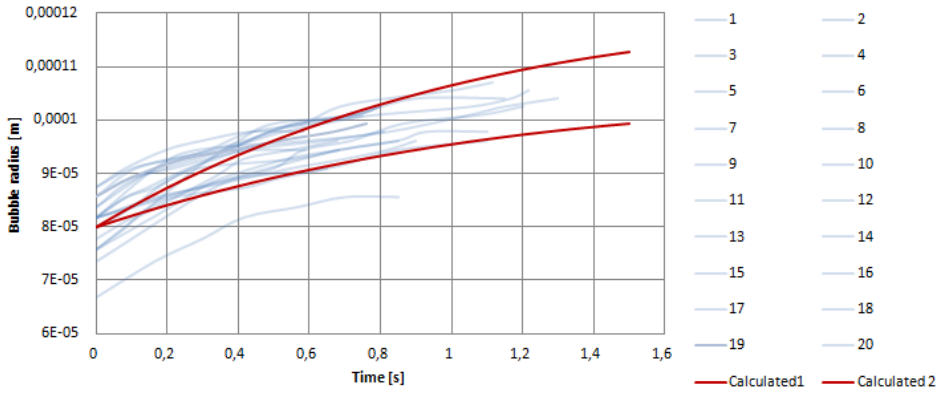

Figure 4.22: Calculated bubble radii, along with bubbles associated with figure 4.11.

4.2.5. Modeling bubble layer

In this subsection, the bubble layer will be simulated using a bubble diameter that increases with the height of the electrode. Using the information collected from figure 4.5, figure 4.6 and figure 4.11 along with the calculated bubble radius 4.22, it was determined that the average bubble increases approximately 50% after the bubble is released from the electrode. The bubble diameter before release is according to the experiments mentioned in chapter 2.3.3, between 30 to 50 μm. In addition, Zhang et al. reported similar detachment diameters [67]. However, it is not possible to include bubble growth in COMSOL. Therefore, a piecewise function is applied to change the bubble diameter along with the height of the electrode. A piecewise function can describe a function on different intervals. The piecewise function used in this simulation is shown in figure 4.23. Here the bubble radius starts at 20 μm and goes up to 30 μm. It was chosen to mimic the growth of the bubble by a faster growth at the beginning and slower growth at the end of the electrode.

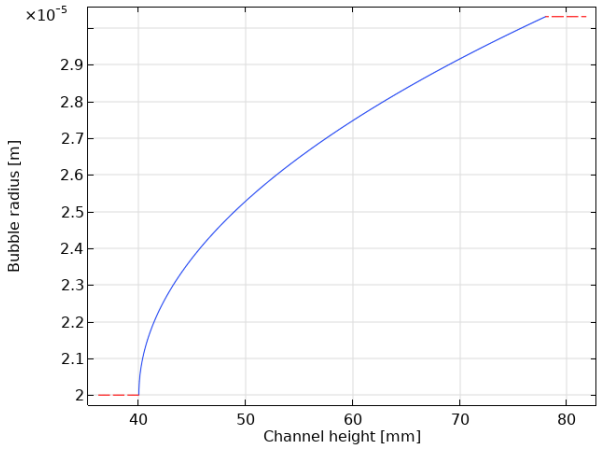

Figure 4.23: Piecewise function to account for the change in bubble size along the electrode.

To simulate the bubble layer, the Bubbly flow model was used together with the slip velocities mentioned in chapter 2.3.7. The computational geometry and boundary conditions are described in chapter 3.1 and 3.3. In figure 4.24, the result of the simulation is shown. The red dots are the data points of the experiment performed by Hreiz and the blue line is the simulated bubble layer. As can be seen in figure 4.24, the simulation captures the shape and thickness of the bubble layer very well. The same technique has been used for two different cases, namely at a current density of 65 and 260 A/m^2 and is shown in the appendix A.10.

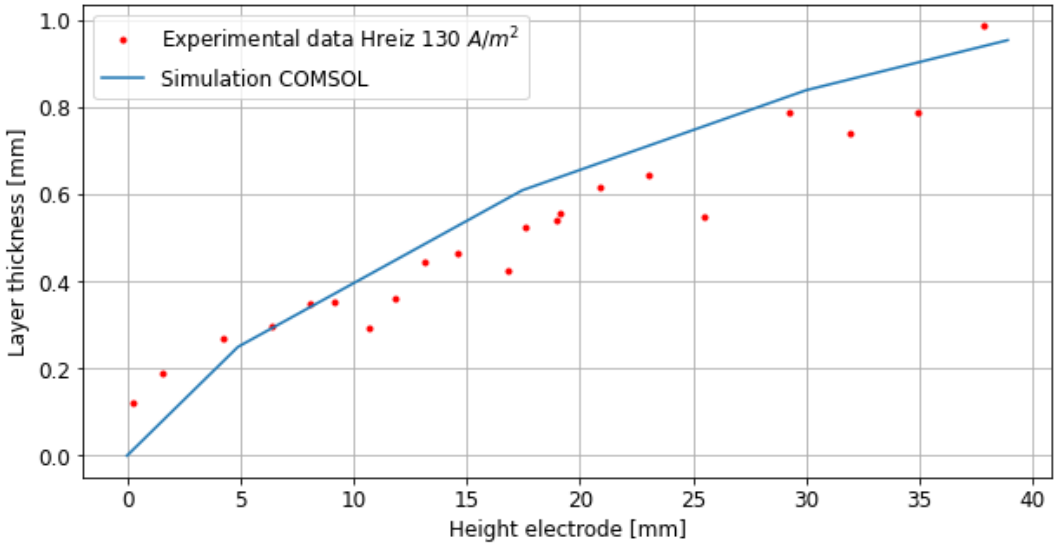

Figure 4.24: Development of the oxygen bubble layer thickness along the electrode in a 0.5 molar a sodium hydroxide solution.

4.3. Modeling bubble layer forced convection configuration

In this section, we return to the case discussed in section 4.1, in which a fixed bubble diameter is applied. The experiment was performed using a forced electrolyte flow (Re = 900) at a current density of 800 A/m^2[31]. The bubble layer thickness on the oxygen side is used as a comparison for the simulation. However, the simulated bubble layer did not match the bubble layer thickness found in the experiment. As proved in the previous section, by including bubble growth, the bubble layer can be accurately simulated. Therefore, the increase in bubble diameter along with the height of the electrode is now considered. To determine the bubble growth, the method used in paragraph 4.2.2 is applied. First, using the computational setup in section 3.4, the dissolved gas layer will be simulated. The result of this simulation is shown in figure 4.25. When comparing the dissolved gas layer from the previous section (4.17), it is noticeable that the layers are approximately equal in thickness while the current density is more than 6x higher. This has to do with the forced electrolyte flow, the dissolved gas has less time to diffuse into the bulk of the electrolyte.

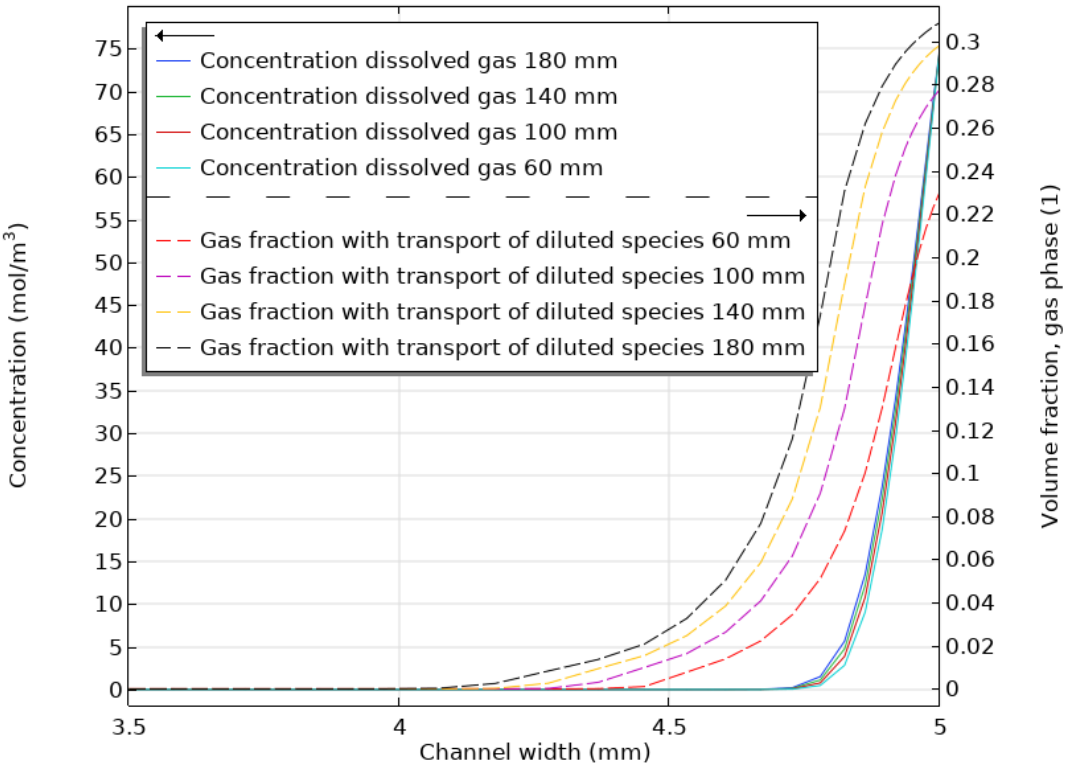

Figure 4.25: The concentration profiles (solid lines) for different heights in a 0.833 wt% potassium hydroxide solution, at a current density of 800 A/m^2 and a forced flow (Re = 900, 0.18 m/s). The secondary axis indicates the gas fraction (dashed lines) for the different heights.

4.3.1. Particle pathlines

Since there are no videos available of the experiments performed by Lee, the particle pathlines had to be tracked in a different way. Fortunately, COMSOL can help us with this by adding particle trajectories. With this tool the particle pathlines can be calculated by releasing particles in the geometry. Once the particles are released, they are coupled with the velocity of the gas bubbles, which is calculated by the Bubbly flow model. As shown in figure 4.26, the particle pathlines corresponding to conditions of the experiment mentioned above. Here 15 particles (gas bubbles) are evenly distributed over the electrode and released at the same time. The colored bar on the right side indicated the velocity of the particle

(gas bubbles).

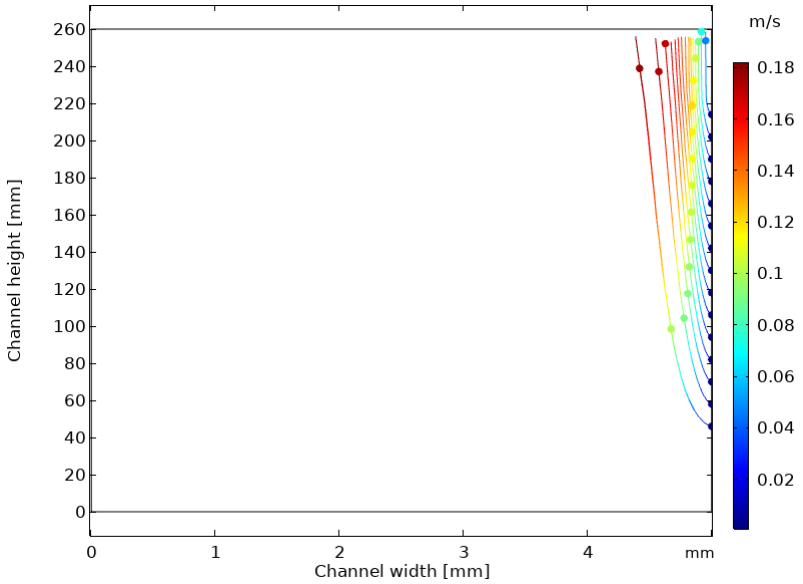

Figure 4.26: Fifteen particles (gas bubbles) evenly distributed over the electrode along with their trajectories. The dots/circles represent the particles (gas bubbles).

Based on the data from COMSOL, the zoomed-in particle path lines are plotted in figure 4.27. Remarkably, the trajectory of the particle depends on where the particle is released into the channel. This is because the electrolyte experiences an upward flow caused by the bubbles, which changes the velocity profile along the electrode.

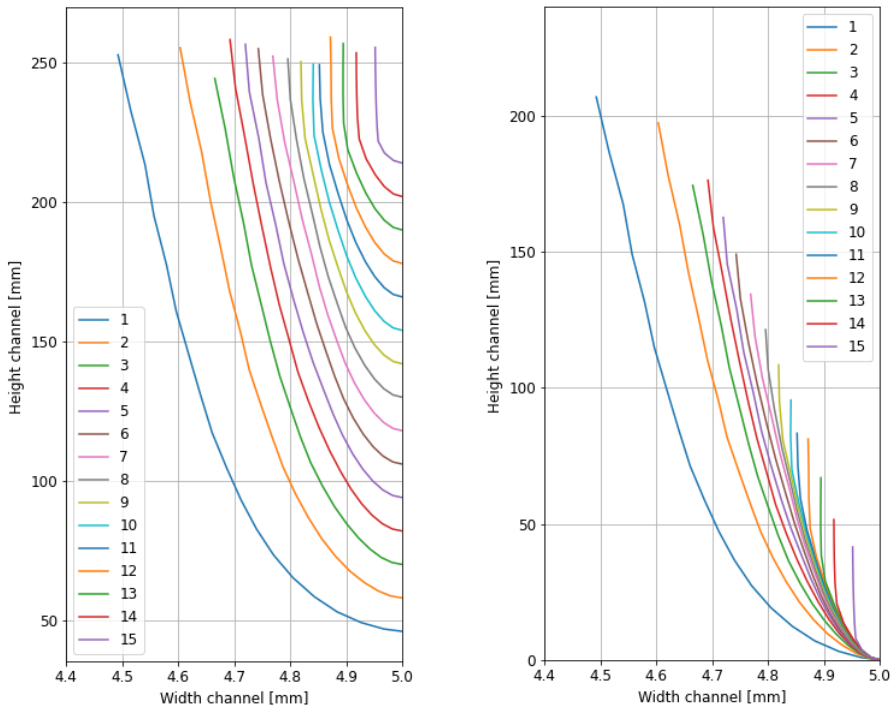

(a) Particle trajectories.

(b) Particle trajectories shifted vertically.

Figure 4.27: Zoomed in particle trajectories associated with the particle pathlines in figure 4.26.

The velocity profile along the electrode is shown in figure 4.28. As shown in the figure below, the velocity along the electrode increases. Thereby influencing the behavior of the particle, resulting in a different pathline.

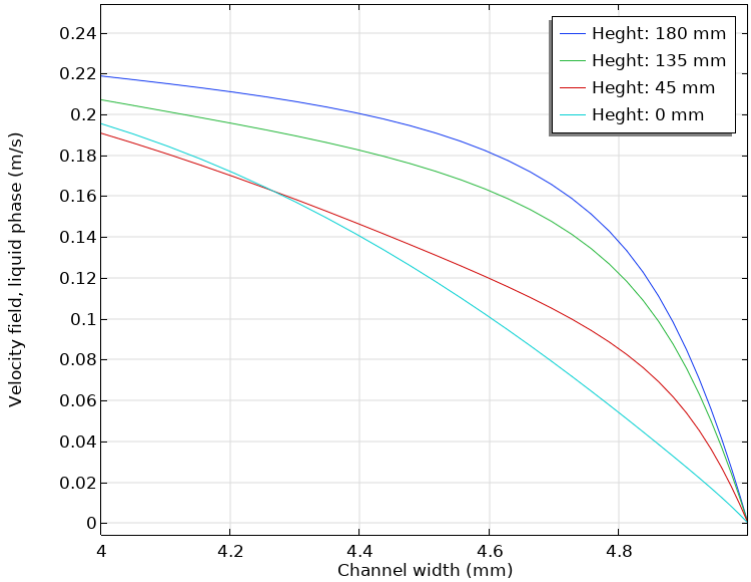

Figure 4.28: Liquid velocity profiles for the different heights.

4.3.2. Bubble growth

Now that each particle pathline is known, along with the concentration of dissolved gas, the bubble growth could be determined. This is done by solving the differential equation (4.4) for each bubble, so that the average bubble radius can be calculated. The result is shown in figure 4.29, the solid blue line represents the average bubble radius along the electrode. The blue dots represent the bubble radius based on the interval given by the particle pathline. As can be seen in figure 4.26 the bubble moves rapidly out of the layer of dissolved gas, which causes a short growth spurt.

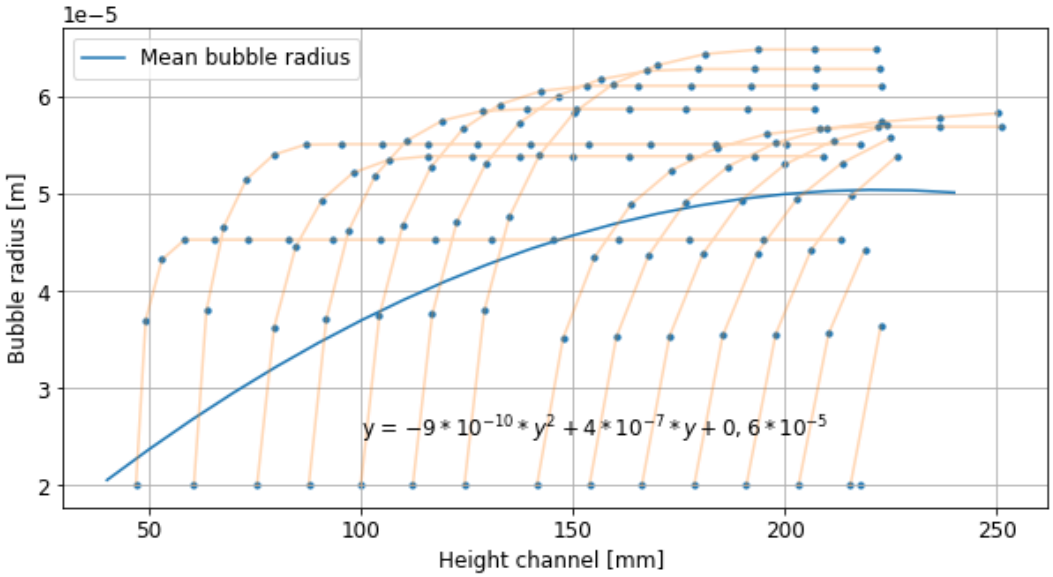

Figure 4.29: Calculated bubble radii associated with the particle pathlines shown in figure 4.26.

4.3.3. Simulation bubble layer

As explained in section 4.2.5 COMSOL cannot account bubble growth due to mass transfer. Therefore, a piecewise function shown in figure 4.30 is used to account for this growth. As can be seen in figure 4.29 the average bubble grows gradually; this has been imitated in the piecewise function.

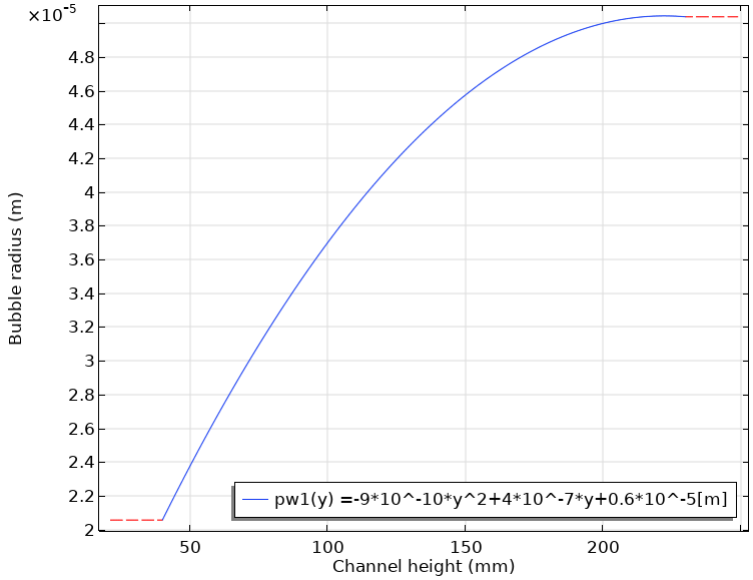

Figure 4.30: Piecewise function to account for the change in bubble size along the electrode based on the calculated average bubble size.

Figure 4.31 illustrates the development of the oxygen bubble layer indicated as the orange line. The green dots are the data points from the experiment performed by Lee. If we compare the simulated bubble layer with the bubble layer found in the experiments, it can be said that they match very well. The thickness is nicely captured as well as the growth of the layer.

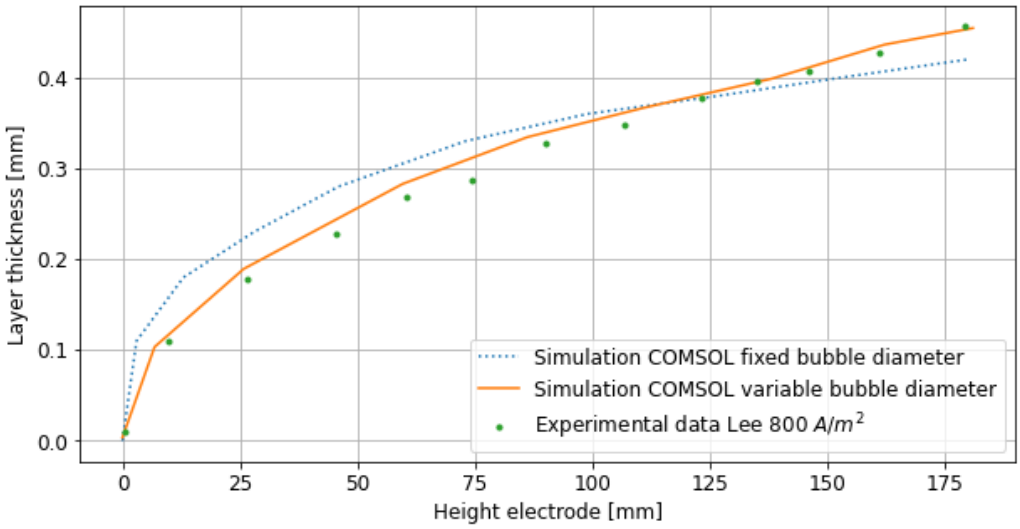

Figure 4.31: Development of the oxygen bubble layer thickness along the electrode, taking into account the increase in bubble size.

When comparing both lines on a log-log plot, it becomes clear that the shape of the simulated bubble layer is quite close to that of the experiment. The simulated bubble layer scales closely with a power

of 0.5, which was also found in the experiments. In short, modeling the bubble layer with an average bubble diameter will not yield the correct bubble layer. The bubble layer differs in bubble dispersion and bubble layer shape. When the increase in bubble diameter due to mass transfer is taken into account, the bubble layer can be simulated well. In both bubble dispersion and bubble layer form, the simulation will calculate the correct bubble layer.

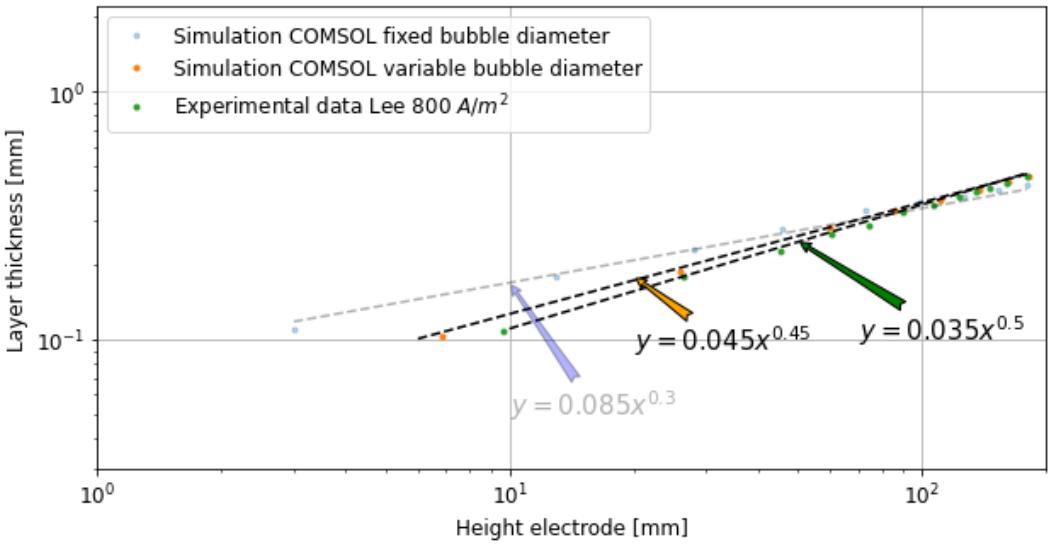

Figure 4.32: Development of the oxygen bubble layer thickness on a log-log plot, taking into account the increase in bubble size.

In appendix A.11 a comparison between the simulated bubble layers and the bubble layers found in the experiments is displayed. The general trend is that the bubble layer can be simulated well at a Reynolds number below the critical Reynolds (Re = 1200) [37]. Above the critical Reynolds, the experiments show more (turbulent) dispersion, therefore the thickness of the bubble layer is underestimated. This is because we end up in the turbulence regime. An example is given in figure 4.33. This is where the fluid flow enters the turbulent regime. As can be seen from the figure, the dispersion of the bubble is underestimated.

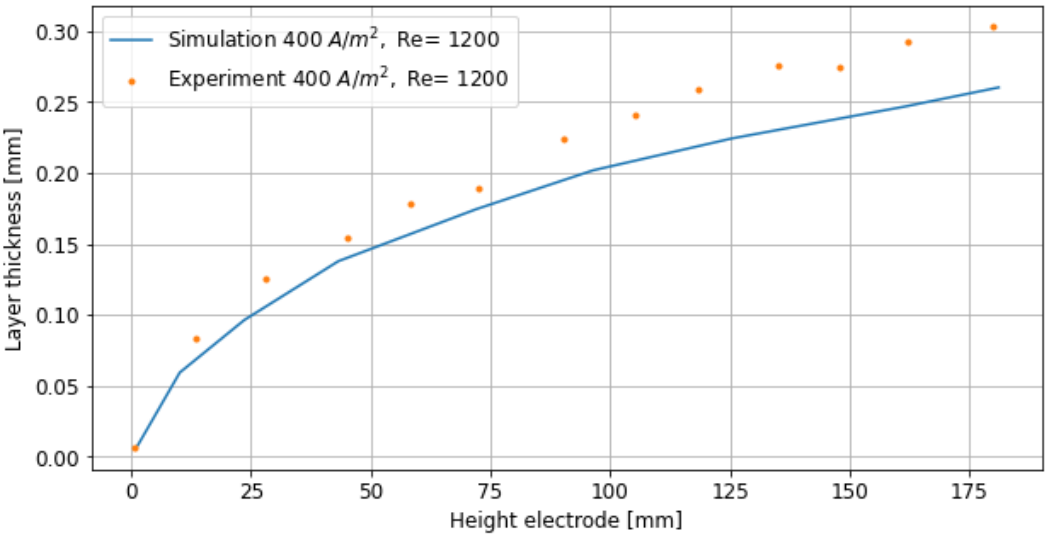

Figure 4.33: Development of the oxygen bubble layer thickness along the electrode, in the turbulent regime.

5

Conclusion

The aim of this thesis was to identify the behavior of the bubbles and their relationship to the shape and thickness of the bubble plume. For this, the Bubbly flow model together with the transport of diluted species was used. The simulation results are then compared with the experimental data. The main findings of this are summarized below.

- First, a simulation was performed in COMSOL using the Bubble flow model to model the bubble plume found by Lee et al. This resulted in a bubble plume that differed in thickness and shape from the bubble plume found in the experiments. Notably, the shape of the bubble plume deviated, the plume simulated by COMSOL scales with a power of 0.3 while the plume found in the experiments scales with a power of 0.5. As mentioned in chapter 2.3.3, the bubble undergoes a significant change in size in the direction of the flow. Since the slip velocities are strongly dependent on the bubble size, it is likely that the bubble size influences the shape and thickness of the bubble plume.
- Several experimental studies have shown that there are four major phenomena that can change bubble size, e.g., bubble coalescence, change in hydrostatic pressure, water vapor, and mass transfer. In chapter 2.3.3 the above reasons are explained, concluding that most of the bubble growth is probably due to mass transfer. To strengthen this hypothesis, we first investigated whether the bubble size indeed increases in the flow direction. The videos made available by Hreiz were used for this. Using the Trackpy algorithm (Python package), the bubbles in the video are tagged and measured, the results are shown in figure 4.5 and figure 4.6. This indeed shows that the mean bubble size increases considerably in the flow direction.
- The Trackpy algorithm has verified that the mean bubble size is not constant along the height of the electrode. To determine where in the channel the bubbles grow, individual bubbles were tracked. This shows that bubbles grow in size close to the electrode and bubbles that are multiple bubble diameters away from the electrode do not or hardly grow. This implies that no mass transfer takes place multiple bubble diameters away from the electrode, therefore the layer of dissolved gas is quite thin.
- Twenty bubbles were tracked to determine the concentration field of dissolved gas in the vicinity of the electrode. The size of these bubbles is accurately recorded and was used to determine the growth rate of each bubble. Based on these growth rates, the local concentration of dissolved gas can be determined. This is compared to the concentration field calculated by COMSOL, which corresponds reasonably well to the measured concentration field.
- The concentration field calculated by COMSOL is then used to determine bubble growth using differential equation 2.13. The differential equation appears to be able to describe the bubble growth well.
- By correcting for this bubble growth in the simulation, it was possible to accurately simulate the bubble plume found by Hreiz's experiment. This has been verified by applying the same technique to simulate the bubble plume reported by Lee.

There are some notable conclusions that can be drawn: when using a fixed bubble diameter, the simulation does not show the correct bubble layer shape and thickness. Flow visualizations have shown significant bubble growth after the bubbles are released from the electrode. In addition, several experiments have also shown that the bubbles significantly increase in diameter in the flow directions. This bubble growth depends on four main phenomena, e.g., bubble coalescence, change in hydrostatic pressure, presence of water vapor, and mass transfer of dissolved gas. Of these, the mass transfer of dissolved gas contributes the most to bubble growth. This means that the electrolyte in the vicinity of the electrode becomes enriched with dissolved gases. By including mass transfer of dissolved gas in the simulations, the growth of the bubbles could be calculated. This bubble growth could then be related to the average bubble diameter along the height of the electrode. Using the calculated average bubble diameter along the electrode height, the bubble layer can be accurately simulated (both in thickness and shape), over a wide range of different operating conditions. Therefore, bubble growth must be included in the simulations to determine the correct bubble layer.

6

Recommendations

In this final chapter, recommendations are made to improve or extend the work of this thesis.

- A major obstacle was the availability of good and reliable information about plume thickness. The available data varies widely in terms of cell arrangement, electrolyte, flow conditions, surface conditions of the electrode (rough or smooth), and electrode material. All this affects the production of the bubbles and the concentration of dissolved gas. It would be helpful to do these experiments in-house to be able to control those variables.
- COMSOL is very user-friendly but has some shortcomings, i.e., it is not possible to include bubble growth. Perhaps another program such as OpenFOAM or Fluent can include this in the simulations.
- The simulations and bubble growth calculations were done in 2D, it might be interesting to see the outcome of the simulations and calculations in 3D.
- Include the adherence region in the simulation.
- Change Dirichlet boundary condition (concentration obtain from the experiment from Shibata) to:

$$j = -NFD\frac{dc}{dy} \tag{6.1}$$

A

Appendix

A.1. Sechenov equation

As mentioned before, the Sechenov equation relates the concentration of the salt solution to that of pure water. The equation is shown below:

$$\log\left(\frac{H_0}{H_{\text{salt}}}\right) = k_{\text{salt}} b \tag{A.1}$$

Parameter	Properties	Dimensions
H_0	Henry's constant for pure water	$\frac{Pa \cdot m^3}{mol}$
H_{salt}	Henry's constant for salt solution	$\frac{Pa \cdot m^3}{mol}$
k_{salt}	Constant of Sechenov	M
b	Molality of the salt	$\frac{mol}{kg}$

Table A.1: Parameters used in the equation of Sechenov.

A.2. Bubble layers of the different experiments.

This section provides an overview of the bubble layers from various experiments. The first three figures show the thickness of the bubble layer. The last three figures show the same bubble layers on a log-log scale.

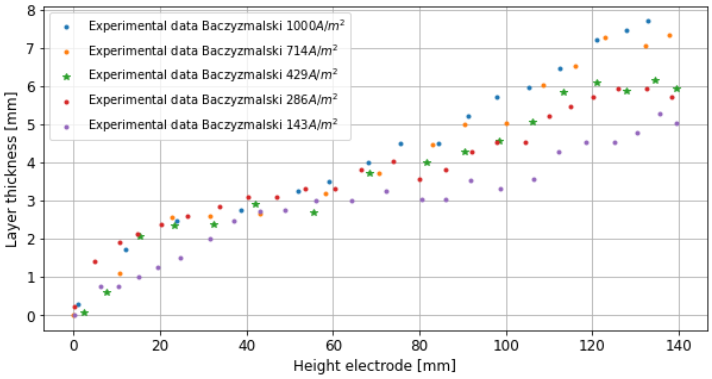

Figure A.1: Experiment preformed by Baczymalski for a wide range of current densities.

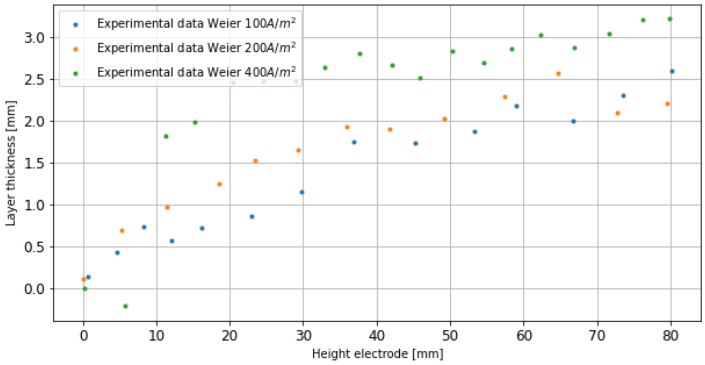

Figure A.2: Experiment preformed by Weier for three different current densities.

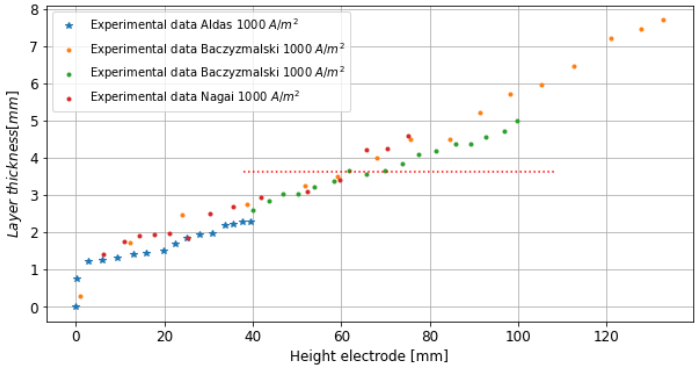

Figure A.3: Various experiment data preformed at a current density of 1000 A/m^2.

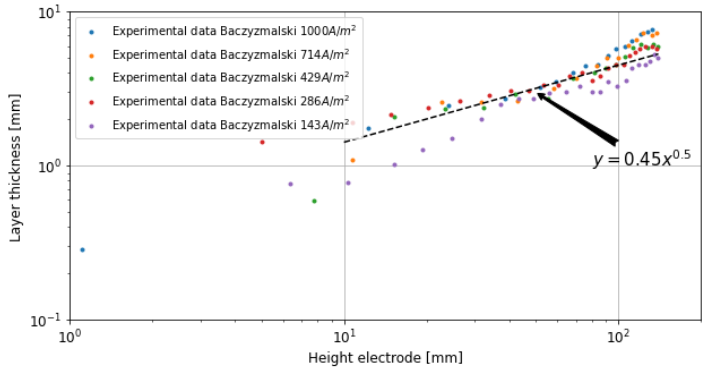

Figure A.4: Experiment preformed by Baczymalski for a wide range of current densities.

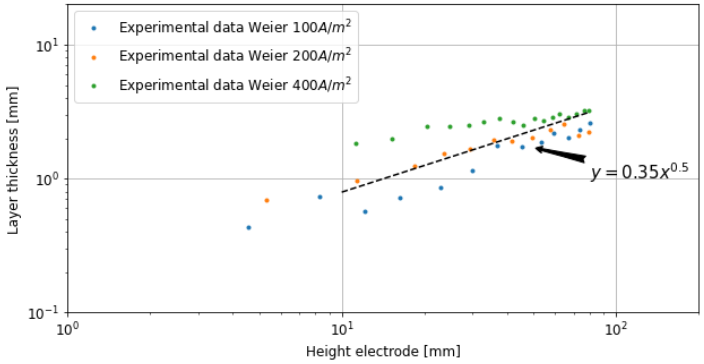

Figure A.5: Experiment preformed by Weier for three different current densities.

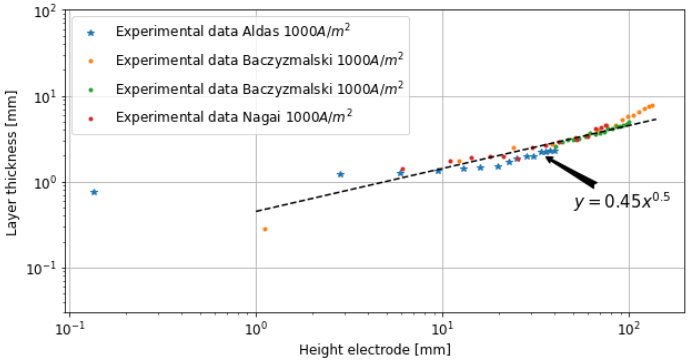

Figure A.6: Various experiment data preformed at a current density of 1000 A/m².

A.3. Derivation real slip velocities

To convert the relative motion of the dispersed phase to the real slip velocities, $\mathbf{U}_r$ is divided by $\alpha(1-\alpha)$. The following set of equations is used to show that if we divide by $\alpha(1-\alpha)$, we do indeed get the real slip velocities.

$$\mathbf{U}_g = \alpha \mathbf{u}_g \tag{A.2}$$

$$\mathbf{U}_l = (1-\alpha)\mathbf{u}_l \tag{A.3}$$

$$\mathbf{U} = \mathbf{U}_g + \mathbf{U}_l \tag{A.4}$$

$$\mathbf{U}_r = \mathbf{U}_g - \alpha \mathbf{U} \tag{A.5}$$

By substituting equation A.2 and A.3 into equation A.4, we end up with the following equation:

$$\mathbf{U} = \alpha \mathbf{u}_g + (1-\alpha)\mathbf{u}_l \tag{A.6}$$

Next, substituting equation A.6 and equation A.2 into equation A.5. This results in the equation shown below:

$$\mathbf{U}_r = \alpha \mathbf{u}_g - \alpha(\alpha \mathbf{u}_g + (1-\alpha)\mathbf{u}_l) \tag{A.7}$$

Dividing both sides by α and rearranging the equation gives the following equation:

$$\frac{\mathbf{U}_r}{\alpha(1-\alpha)} = \mathbf{u}_g - \mathbf{u}_l \tag{A.8}$$

Equation A.8 indeed shows that dividing the ”relative superficial velocity” $\mathbf{U}_r$ by $\alpha(1-\alpha)$, we get the real slip velocities.

Parameter	Properties	Dimensions
$\mathbf{U}_g$	Superficial velocity gas	$\frac{m}{s}$
$\mathbf{U}_l$	Superficial velocity liquid	$\frac{m}{s}$
$\mathbf{U}_r$	Relative velocity gas phase	$\frac{m}{s}$
$\mathbf{u}_l$	Phase velocity	$\frac{m}{s}$
$\mathbf{u}_g$	Phase velocity	$\frac{m}{s}$
$\mathbf{U}$	Superficial velocity	$\frac{m}{s}$
α	Gas fraction	

Table A.2: Parameters used to derive the true slip velocities.

A.4. Volume forces used in the Euler-Euler model

In addition to the slip velocities, it is also possible to describe the movement of the bubble via volume forces. These volume forces listed below are based on the two-phase model reported by Le Bideau et al. [30]. The first volume force is the drag force:

$$\mathbf{F}_D = -\frac{3}{4}\alpha\rho\frac{C_D}{d_b}|\mathbf{u}_g - \mathbf{u}_l|\mathbf{u}_g - \mathbf{u}_l \tag{A.9}$$

The second volume force is the lift force:

$$\mathbf{F}_{\text{lift}} = -C_{\text{lift}}\rho|\mathbf{u}_g - \mathbf{u}_l|\text{rot}(\mathbf{u}_l) \tag{A.10}$$

The last volume force is the bubble dispersion force:

$$\mathbf{F}_{BD} = -\alpha\rho\frac{K_g}{d_b}|\mathbf{u}_g - \mathbf{u}_l|\nabla\alpha \tag{A.11}$$

The slip velocities can be converted into volume forces with:

$$\mathbf{F} = 18\alpha\mu_l\mathbf{u}_{\text{slip}}d^2 \tag{A.12}$$

Parameter	Properties	Dimensions
$\mathbf{u}_l$	Phase velocity	$\frac{m}{s}$
$\mathbf{u}_g$	Phase velocity	$\frac{m}{s}$
d_b	bubble diameter	m
ρ	Density	$\frac{kg}{m^3}$
α	Gas fraction	
K_g	Fitting parameter	
C_D	Drag coefficient	
C_{lift}	Lift coefficient	
μ_l	Dynamic viscosity liquid	$Pa \cdot s$
$\mathbf{u}_{\text{slip}}$	Phase velocity	$\frac{m}{s}$
d	Bubble diameter	m

Table A.3: Parameters used in the volume forces equations.

A.5. Bubble diameter versus distance from the electrode

The bubbles tracked in figure 4.11 are plotted versus the distance from the electrode. It looks quite messy because the bubbles have an unpredictable particle pathline (sometimes jumping back and forth). However, it becomes apparent that as the bubble grows, the distance from the electrode also increases. This is believed to be the main reason that the bubble layer shape and thickness are not simulated well when using a fixed bubble diameter. Therefore, the bubble growth must be included in the simulations.

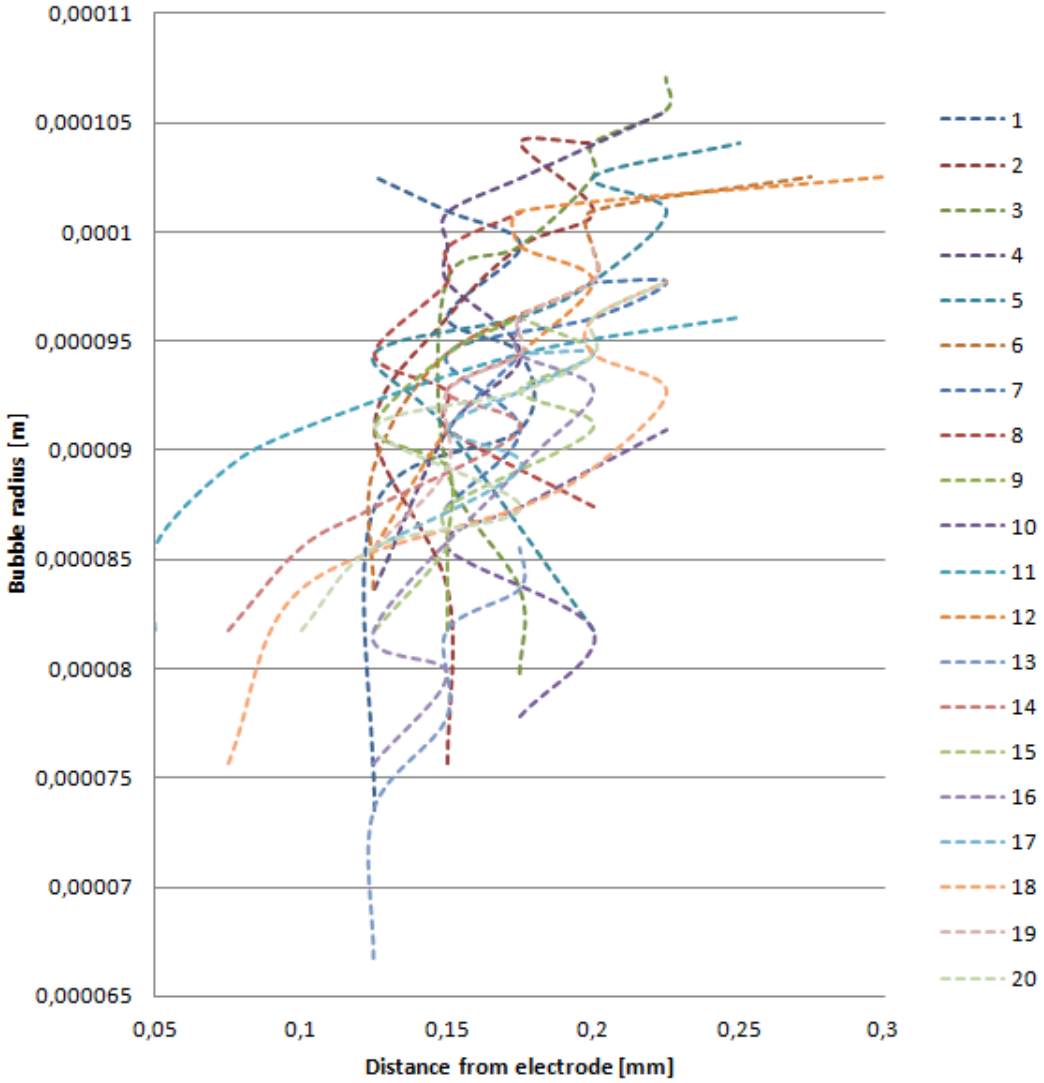

Figure A.7: Oxygen bubble diameter versus distance from the electrode. The bubble measurements were taken from the video provided by Hreiz [19].

A.6. Determination of the bubble layer thickness

The thickness of the bubble layer is determined by drawing two straight lines (by hand). The first line is drawn where the gas fraction decreases sharply with increasing distance from the electrode. The second line is drawn where there is only a small decrease in the gas fraction with increasing distance from the electrode. The intersection of these lines is assumed to indicate the thickness of the bubble layer.
In figure A.8 an example is given how the thickness of the bubble layer is determined. Here the experiment performed by Lee is used [31]. The experiment was conducted using a forced electrolyte flow (Re = 900) at a current density of 800 A/m^2. As can be seen in the figure A.8, the gas fraction decreases sharply with increasing distance from the electrode (up to ≈0.3 mm). After the sharp drop in the gas fraction, the gas fraction decreases slightly until it reaches zero. By drawing two lines corresponding to the slope of the change in the gas fraction. Two distinct slopes can be seen, the intersection of these lines indicates the thickness of the bubble layer.

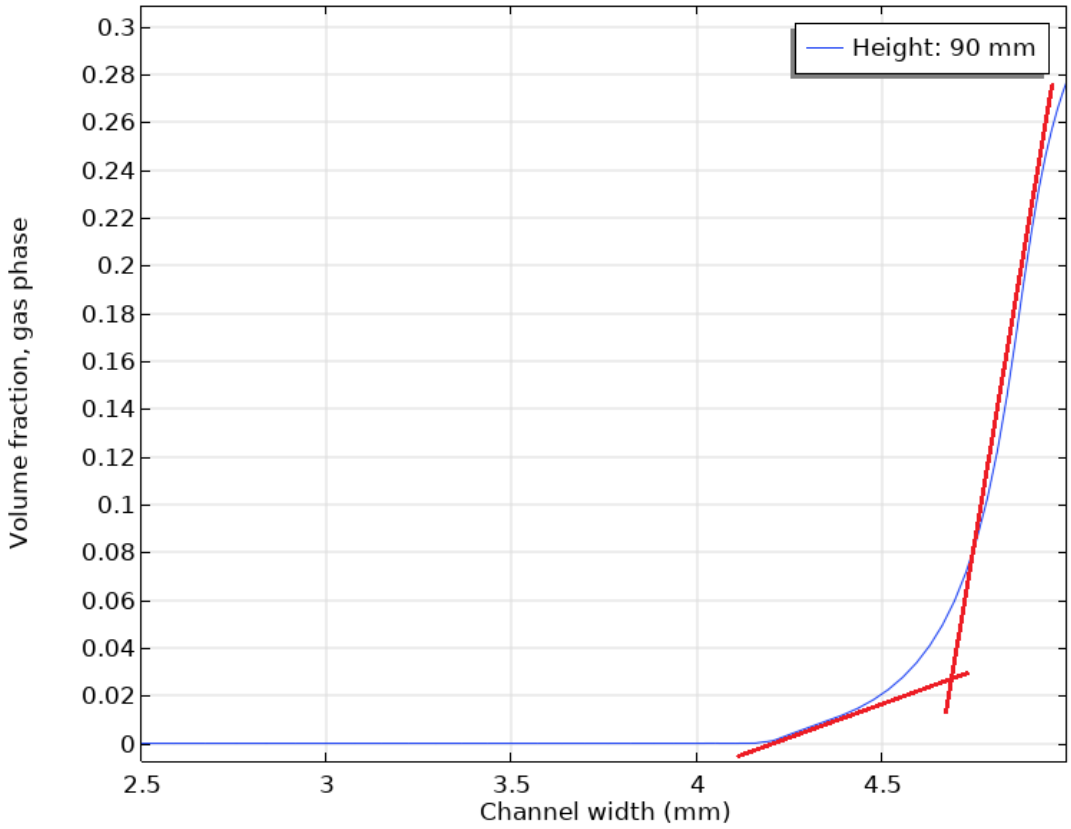

Figure A.8: Determination of the bubble layer thickness.

A.7. Boundary conditions Bubbly flow model

The boundary conditions for the second and third geometry are listed below. For the second geometry (shown in figure 3.1b), the initial and boundary conditions are briefly summarized below. Note that on both sides of the channel oxygen evolution takes place, the working electrodes are places outside of the channel. The inlet and outlet boundary conditions are:

$$\begin{array}{ll} u_{lx} = 0\ \mathrm{m/s} & \text{for } 0 \le y \le W_2, \quad \text{and } x = 0 \\ u_{ly} = 0\ \mathrm{m/s} & \text{for } 0 \le y \le W_2, \quad \text{and } x = 0 \end{array} \tag{A.13}$$

$$\begin{array}{ll} P_{out} = 0 & \text{for } 0 \le y \le W_2, \quad \text{and } x = (2H_2 + H_3) \\ \text{Slip condition for liquid} & \text{for } 0 \le y \le W_2, \quad \text{and } x = (2H_2 + H_3) \end{array} \tag{A.14}$$

The no-slip boundary condition is enforced at walls:

$$\begin{array}{lll} \mathbf{u}_l(x,y) = 0\ \mathrm{m/s} & \text{for } 0 \le x \le H_2 \text{ and } 2H_2 \le x \le (2H_2 + H_3), & \text{and } y = 0 \\ \mathbf{u}_g(x,y) = 0\ \mathrm{m/s} & \text{for } 0 \le x \le H_2 \text{ and } 2H_2 \le x \le (2H_2 + H_3), & \text{and } y = 0 \end{array} \tag{A.15}$$

$$\begin{array}{lll} \mathbf{u}_l(x,y) = 0\ \mathrm{m/s} & \text{for } 0 \le x \le H_2 \text{ and } 2H_2 \le x \le (2H_2 + H_3), & \text{and } y = W_2 \\ \mathbf{u}_g(x,y) = 0\ \mathrm{m/s} & \text{for } 0 \le x \le H_2 \text{ and } 2H_2 \le x \le (2H_2 + H_3), & \text{and } y = W_2 \end{array} \tag{A.16}$$

The gas flux leaving the electrodes:

$$N_{O2}(x, y = 0\ \&\ x, y = W_2) = \frac{1}{4}\frac{RTj}{PF} \text{ for } H_2 \le x \le 2H_2 \tag{A.17}$$

In the third geometry (shown in figure 3.1c), the initial and boundary conditions are briefly summarized below. The inlet and outlet boundary conditions are:

$$\begin{array}{ll} u_{lx} = 0.18\ \mathrm{m/s} & \text{for } 0 \le y \le W_3, \quad \text{and } x = 0 \\ u_{ly} = 0\ \mathrm{m/s} & \text{for } 0 \le y \le W_3, \quad \text{and } x = 0 \end{array} \tag{A.18}$$

$$P_{out}(x) = 0 \quad \text{for } 0 \le y \le W_3, \quad \text{and } x = H_4 \tag{A.19}$$

The no-slip boundary condition is enforced at walls:

$$\begin{array}{lll} \mathbf{u}_l(x,y) = 0\ \mathrm{m/s} & \text{for } 0 \le x \le H_6 \text{ and } (H_6 + H_5) \le x \le H_4, & \text{and } y = 0 \\ \mathbf{u}_g(x,y) = 0\ \mathrm{m/s} & \text{for } 0 \le x \le H_6 \text{ and } (H_6 + H_5) \le x \le H_4, & \text{and } y = 0 \end{array} \tag{A.20}$$

$$\begin{array}{lll} \mathbf{u}_l(x,y) = 0\ \mathrm{m/s} & \text{for } 0 \le x \le H_6 \text{ and } (H_6 + H_5) \le x \le H_4, & \text{and } y = W_3 \\ \mathbf{u}_g(x,y) = 0\ \mathrm{m/s} & \text{for } 0 \le x \le H_6 \text{ and } (H_6 + H_5) \le x \le H_4, & \text{and } y = W_3 \end{array} \tag{A.21}$$

The gas flux leaving the electrodes:

$$N_{H2}(x, y = 0) = \frac{1}{2}\frac{RTj}{PF} \text{ for } H_6 \le x \le (H_6 + H_5) \tag{A.22}$$

$$N_{O2}(x, y = W_3) = \frac{1}{4}\frac{RTj}{PF} \text{ for } H_6 \leq x \leq (H_6 + H_5) \tag{A.23}$$

Parameter	Properties	Dimensions
$R_{\text{universal}}$	Universal gas constant	$\frac{J}{mol \cdot K}$
P	Pressure	Pa
F	Faraday's constant	$\frac{C}{mol}$
T	Temperature	K
j	Current density	$\frac{A}{m^2}$
$\mathbf{u}_l$	Liquid velocity	$\frac{m}{s}$
$\mathbf{u}_g$	Gas velocity	$\frac{m}{s}$

Table A.4: Parameters used in the boundary conditions

A.8. Measuring technique

The measuring technique is quite straightforward. The videos made available by Heinz are divided into a sequence of images (.TIFF stack, .PNG or any other format), with each image representing a frame. Once divided, you can scroll through the images and zoom in. The width of the channel is about 240 pixels and the height of the channel is about 1000 pixels. Which means that each pixel is approximately 0.025x0.025 mm.
The accuracy for bubble tracking is 1 pixel, that's why the measurements are equally distributed in figures 4.14, 4.15, 4.18, 4.20, 4.21. In the case of measuring the bubble radius, a circle can be drawn around the bubble of interest (using a Python package called OpenCV). An example of an area measurement is given in figure A.9. Then the area is calculated by the number of pixels enclosed by the yellow circle. The accuracy of measuring the bubble radius is ≈ 0.001 mm^2.

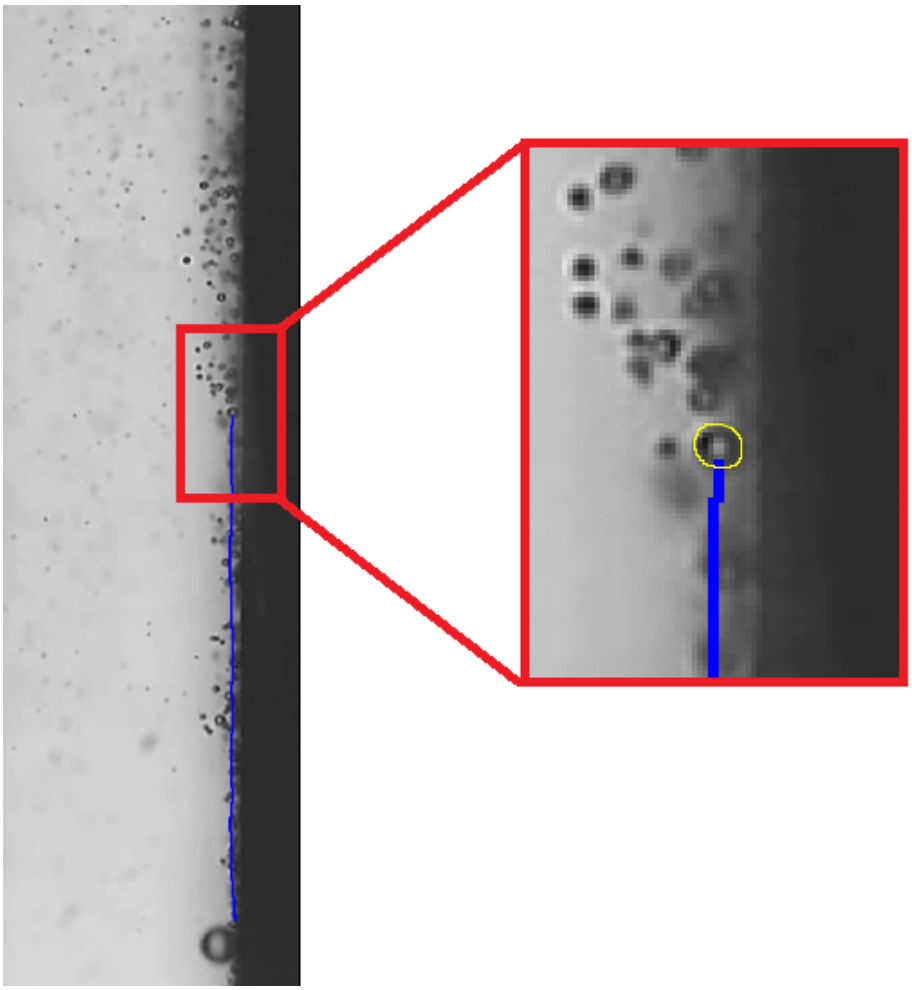

Figure A.9: Measuring technique bubble size.

A.9. Simulation results experiment Hreiz

In this section, the results of the simulation based on Hreiz's experiment are briefly discussed. First the concentration of dissolved gas is plotted over the entire domain. As shown in the figure, the steps in the Dirichlet boundary condition are clearly visible. An improvement would be to use a piecewise function so that the steps in concentration are smoothed out.

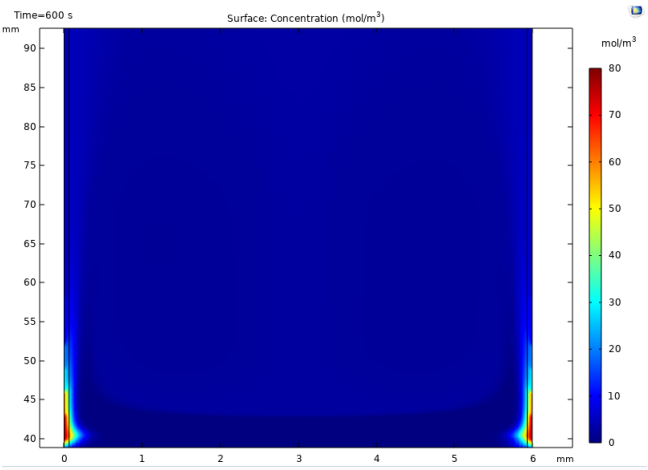

Figure A.10: Concentration of dissolved gas over the entire domain based on the conditions reported by Hreiz.

The zoomed in version of figure A.10 is shown in figure A.11. The faint lines are the contour lines of the concentration.

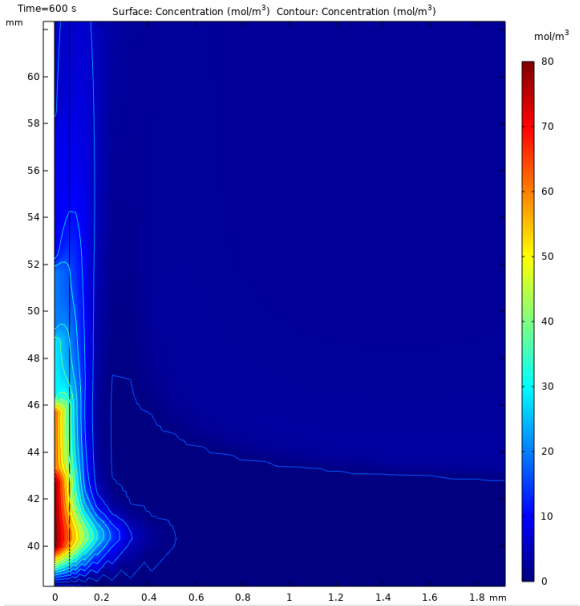

Figure A.11: The zoomed in version of figure A.10.

A.10. Bubble layer Hreiz

The red dots are the data points of the experiment performed by Hreiz and the blue line is the simulated bubble layer. As can be seen in figure A.12, the simulation captures the shape and thickness of the bubble layer very well. The thickness of the oxygen bubble layer was determined by analyzing the videos of Hreiz [19]. The experiment was performed in room temperature, i.e. around 20 °C. The electrolyte was a 0.5 M NaOH solution with nickel for the electrode.

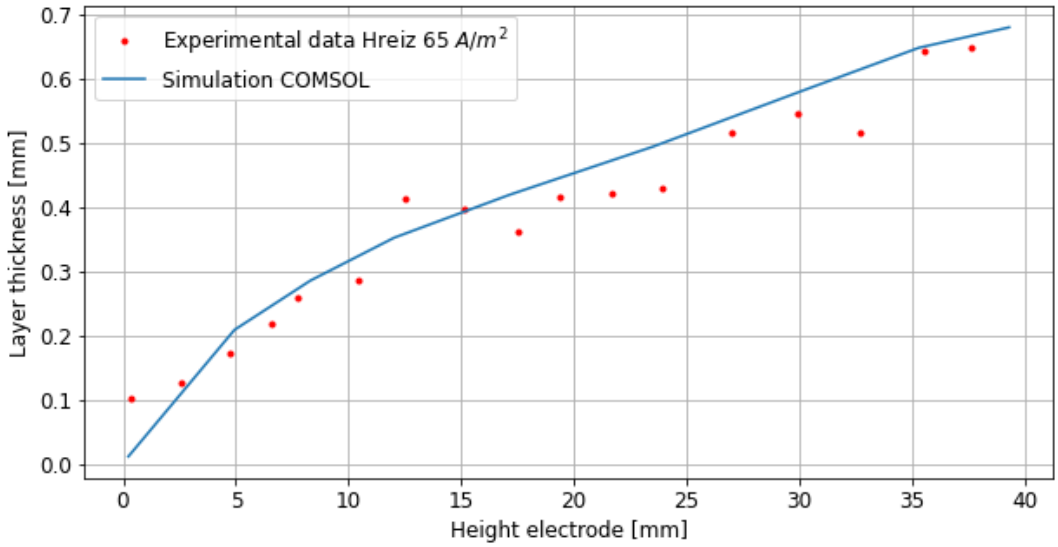

(a) Development of the oxygen bubble layer thickness along the electrode in a 0.5 molar a sodium hydroxide solution at a current density of 65 A/m^2

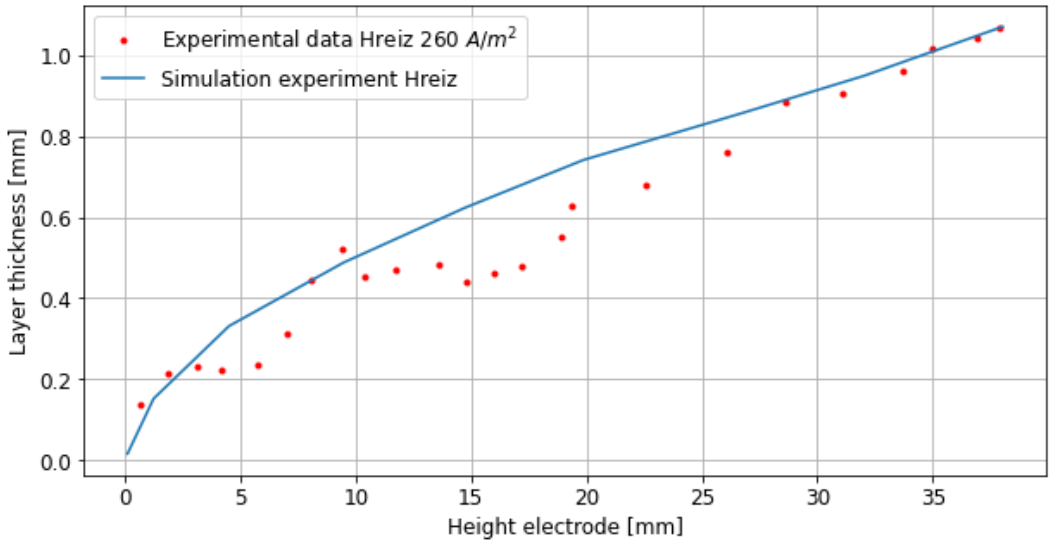

(b) Development of the oxygen bubble layer thickness along the electrode in a 0.5 molar a sodium hydroxide solution at a current density of 260 A/m^2

Figure A.12: Simulation results of the oxygen bubble layer for different current densities.

A.11. Bubble layer simulation Lee

The method explained in section 4.3 has been applied to various operating conditions (different current densities and flow rates). He performed these experiments in a potassium hydroxide solution (0.833 wt %) with an Ir/Ru alloy (Iridium-Ruthenium) for the electrodes. As can be seen from the figure A.13, the thickness and shape of the simulated bubble layers are nicely simulated of a wide range of different operating conditions.
Lee determined the thickness of the bubble layer by averaging multiple images (reducing the fluctuating movement of the bubbles), then a reference image (just the water flow without the presence of bubbles) is subtracted from the obtained average image, resulting in the thickness of the bubble layer.

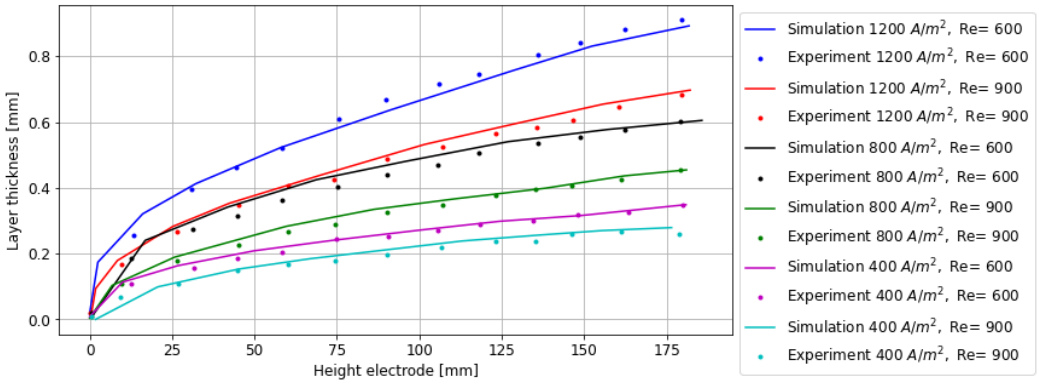

(a) Development of the oxygen bubble layer thickness, taking into account the increase in bubble size.

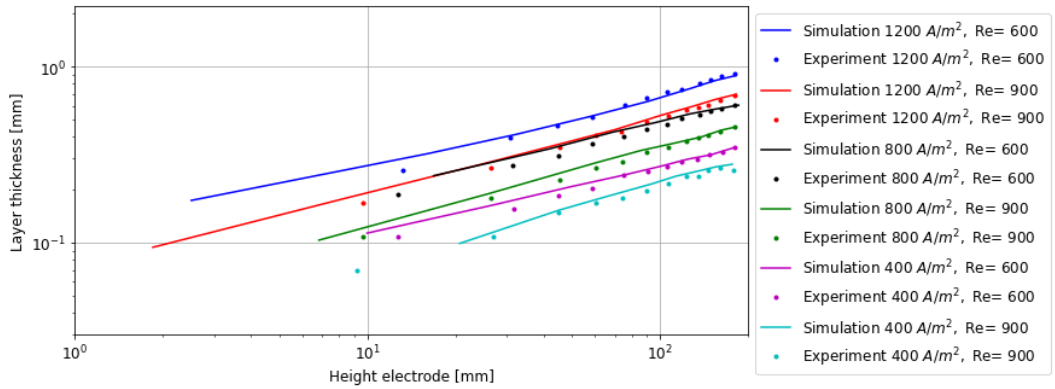

(b) Development of the oxygen bubble layer thickness on a log-log plot, taking into account the increase in bubble size.

Figure A.13: Simulation results of the oxygen bubble layer for different operating conditions.

Bibliography

[1] Lokmane Abdelouahed et al. “Hydrodynamics of gas bubbles in the gap of lantern blade electrodes without forced flow of electrolyte: Experiments and CFD modelling”. In: *Chemical Engineering Science* 111 (2014), pp. 255–265.

[2] Dominik Baczyzmalski et al. “Near-wall measurements of the bubble-and Lorentz-force-driven convection at gas-evolving electrodes”. In: *Experiments in Fluids* 56.8 (2015), pp. 1–13.

[3] RJ Balzer and H Vogt. “Effect of electrolyte flow on the bubble coverage of vertical gas-evolving electrodes”. In: *Journal of the Electrochemical Society* 150.1 (2002), E11.

[4] R Byron Bird, Warren E Stewart, and Edwin N Lightfoot. *Transport Phenomena, revised 2 nd edition*. 2006.

[5] Patrick Boissonneau and Philip Byrne. “An experimental investigation of bubble-induced free convection in a small electrochemical cell”. In: *Journal of Applied Electrochemistry* 30.7 (2000), pp. 767–775.

[6] Wannes Bollens. “Experimental and theoretical study of a small scale chlorate electrolyzer”. In: (2010).

[7] BE Bongenaar-Schlenter et al. “The effect of the gas void distribution on the ohmic resistance during water electrolytes”. In: *Journal of applied electrochemistry* 15.4 (1985), pp. 537–548.

[8] H Cheng, K Scott, and C Ramshaw. “Intensification of water electrolysis in a centrifugal field”. In: *Journal of The Electrochemical Society* 149.11 (2002), p. D172.

[9] European Commission et al. *2030 energy strategy*. 2014.

[10] COMSOL. *CFD Module User’s Guide*. 2018. URL: `https://doc.comsol.com/5.4/doc/com.comsol.help.cfd/CFDModuleUsersGuide.pdf` (visited on 06/18/2021).

[11] Christophe Coutanceau, Stève Baranton, and Thomas Audichon. *Hydrogen electrochemical production*. Academic Press, 2017.

[12] Anders A Dahlkild. “Modelling the two-phase flow and current distribution along a vertical gas-evolving electrode”. In: *Journal of Fluid Mechanics* 428 (2001), pp. 249–272.

[13] John Eigeldinger and Helmut Vogt. “The bubble coverage of gas-evolving electrodes in a flowing electrolyte”. In: *Electrochimica Acta* 45.27 (2000), pp. 4449–4456.

[14] Paul S Epstein and Milton S Plesset. “On the stability of gas bubbles in liquid-gas solutions”. In: *The Journal of Chemical Physics* 18.11 (1950), pp. 1505–1509.

[15] Bjørn Gaudernack. “Hydrogen production from fossil fuels”. In: *Hydrogen power: Theoretical and engineering solutions*. Springer, 1998, pp. 75–89.

[16] JP Glas and JW Westwater. “Measurements of the growth of electrolytic bubbles”. In: *International Journal of Heat and Mass Transfer* 7.12 (1964), pp. 1427–1443.

[17] Philipp Haug et al. “Process modelling of an alkaline water electrolyzer”. In: *International Journal of Hydrogen Energy* 42.24 (2017), pp. 15689–15707.

[18] Fumio Hine and Koichi Murakami. “Bubble effects on the solution IR drop in a vertical electrolyzer under free and forced convection”. In: *Journal of the Electrochemical Society* 127.2 (1980), p. 292.

[19] Rainier Hreiz et al. “Electrogenerated bubbles induced convection in narrow vertical cells: PIV measurements and Euler–Lagrange CFD simulation”. In: *Chemical Engineering Science* 134 (2015), pp. 138–152.

[20] Von N Ibl and J_ Venczel. “Untersuchung des Stofftransports an gasentwickelnden Elektronden”. In: *Metalloberfläche* 24 (1970), pp. 365–374.

[21] MBI Janjua and RL Le Roy. “Electrocatalyst performance in industrial water electrolysers”. In: *International Journal of Hydrogen Energy* 10.1 (1985), pp. 11–19.

[22] LJJ Janssen. “Behaviour of and mass transfer at gas-evolving electrodes”. In: *Electrochimica acta* 34.2 (1989), pp. 161–169.

[23] LJJ Janssen and JG Hoogland. “The effect of electrolytically evolved gas bubbles on the thickness of the diffusion layer—II”. In: *Electrochimica Acta* 18.8 (1973), pp. 543–550.

[24] LJJ Janssen and SJD Van Stralen. “Bubble behaviour on and mass transfer to an oxygen-evolving transparent nickel electrode in alkaline solution”. In: *Electrochimica Acta* 26.8 (1981), pp. 1011–1022.

[25] Klans Jüttner. “Technical scale of electrochemistry”. In: *Encyclopedia of Electrochemistry: Online* (2007).

[26] R Kumar and NK Kuloor. “The formation of bubbles and drops”. In: *Advances in chemical engineering*. Vol. 8. Elsevier, 1970, pp. 255–368.

[27] S Shiva Kumar and V Himabindu. “Hydrogen production by PEM water electrolysis–A review”. In: *Materials Science for Energy Technologies* 2.3 (2019), pp. 442–454.

[28] Dieter Landolt et al. “An Optical Study of Cathodic Hydrogen Evolution in High-Rate Electrolysis”. In: *Journal of the Electrochemical Society* 117.6 (1970), p. 839.

[29] Werner Lang and Rolf Zander. “Salting-out of oxygen from aqueous electrolyte solutions: prediction and measurement”. In: *Industrial & engineering chemistry fundamentals* 25.4 (1986), pp. 775–782.

[30] Damien Le Bideau et al. “Eulerian two-fluid model of alkaline water electrolysis for hydrogen production”. In: *Energies* 13.13 (2020), p. 3394.

[31] Jae Won Lee, Dong Kee Sohn, and Han Seo Ko. “Study on bubble visualization of gas-evolving electrolysis in forced convective electrolyte”. In: *Experiments in Fluids* 60.10 (2019), pp. 1–11.

[32] Daniel Lumanauw. “Hydrogen bubble characterization in alkaline water electrolysis”. In: *Mster Thesis. University of Toronto* (2000).

[33] Pierre Millet and Sergey Grigoriev. “Water electrolysis technologies”. In: *Renewable Hydrogen Technologies: Production, Purification, Storage, Applications and Safety* (2013), pp. 19–41.

[34] Niro Nagai, Masanori Takeuchi, and MT Furuta. “Effects of bubbles between electrodes on alkaline water electrolysis efficiency under forced convection of electrolyte”. In: *Proceedings of 16th world hydrogen energy conference, Lyon*. 2006, pp. 1–10.

[35] H Nicolai et al. “Particle velocity fluctuations and hydrodynamic self-diffusion of sedimenting non-Brownian spheres”. In: *Physics of Fluids* 7.1 (1995), pp. 12–23.

[36] Hasan N Oguz and Andrea Prosperetti. “Dynamics of bubble growth and detachment from a needle”. In: *Journal of Fluid Mechanics* 257 (1993), pp. 111–145.

[37] Xueqi Pang et al. “Framework for evaluating the performance limits of membraneless electrolyzers”. In: *Energy & Environmental Science* 13.10 (2020), pp. 3663–3678.

[38] Alka Pareek et al. “Insights into renewable hydrogen energy: Recent advances and prospects”. In: *Materials Science for Energy Technologies* 3 (2020), pp. 319–327.

[39] Robert Phillips and Charles W Dunnill. “Zero gap alkaline electrolysis cell design for renewable energy storage as hydrogen gas”. In: *RSC advances* 6.102 (2016), pp. 100643–100651.

[40] Derek Pletcher and Xiaohong Li. “Prospects for alkaline zero gap water electrolysers for hydrogen production”. In: *International Journal of Hydrogen Energy* 36.23 (2011), pp. 15089–15104.

[41] William E Ranz. “Evaporation from drops, Parts I & II”. In: *Chem Eng Prog.* 48 (1952), pp. 141–146.

[42] H Riegel, J Mitrovic, and K Stephan. “Role of mass transfer on hydrogen evolution in aqueous media”. In: *Journal of applied electrochemistry* 28.1 (1998), pp. 10–17.

[43] Jonathan Schillings, Olivier Doche, and Jonathan Deseure. “Modeling of electrochemically generated bubbly flow under buoyancy-driven and forced convection”. In: *International Journal of Heat and Mass Transfer* 85 (2015), pp. 292–299.

[44] LE Scriven. “On the dynamics of phase growth”. In: *Chemical engineering science* 10.1-2 (1959), pp. 1–13.

[45] S Shibata. “Supersaturation of oxygen in acidic solution in the vicinity of an oxygen-evolving platinum anode”. In: *Electrochimica Acta* 23.7 (1978), pp. 619–623.

[46] Shigeo SHIBATA. “Supersolubility of hydyogen in acidic solution in the vicinity of hydrogen-evolving platinum cathodes in different surface states”. In: *Denki Kagaku oyobi Kogyo Butsuri Kagaku* 44.11 (1976), pp. 709–712.

[47] Shigeo Shibata. “The concentration of molecular hydrogen on the platinum cathode”. In: *Bulletin of the Chemical Society of Japan* 36.1 (1963), pp. 53–57.

[48] Kurian J Vachaparambil and Kristian Etienne Einarsrud. “Numerical simulation of bubble growth in a supersaturated solution”. In: *Applied Mathematical Modelling* 81 (2020), pp. 690–710.

[49] J Venczel. “Über den gasblasen bei elektrochemischen prozessen”. In: *Electrochimica Acta* 15.12 (1970), pp. 1909–1920.

[50] Jozsef Venczel. “Ueber den Stofftransport an gasentwickelnden Elektroden”. PhD thesis. ETH Zurich, 1961.

[51] HFA Verhaart, RM De Jonge, and SJD Van Stralen. “Growth rate of a gas bubble during electrolysis in supersaturated liquid”. In: *International Journal of Heat and Mass Transfer* 23.3 (1980), pp. 293–299.

[52] John Villadsen, Jens Nielsen, and Gunnar Lidén. *Bioreaction engineering principles*. Springer Science & Business Media, 2011.

[53] H Vogt. “Interfacial supersaturation at gas evolving electrodes”. In: *Journal of applied electrochemistry* 23.12 (1993), pp. 1323–1325.

[54] H Vogt. “On the gas-evolution efficiency of electrodes. II–Numerical analysis”. In: *Electrochimica Acta* 56.5 (2011), pp. 2404–2410.

[55] H Vogt. “On the supersaturation of gas in the concentration boundary layer of gas evolving electrodes”. In: *Electrochimica Acta* 25.5 (1980), pp. 527–531.

[56] H Vogt. “On the various types of uncontrolled potential increase in electrochemical reactors—The anode effect”. In: *Electrochimica acta* 87 (2013), pp. 611–618.

[57] H Vogt. “Studies on gas-evolving electrodes: The concentration of dissolved gas in electrolyte bulk”. In: *Electrochimica acta* 30.2 (1985), pp. 265–270.

[58] H Vogt. “The concentration overpotential of gas evolving electrodes as a multiple problem of mass transfer”. In: *Journal of The Electrochemical Society* 137.4 (1990), p. 1179.

[59] H Vogt. “The quantities affecting the bubble coverage of gas-evolving electrodes”. In: *Electrochimica Acta* 235 (2017), pp. 495–499.

[60] H Vogt. “The rate of gas evolution at electrodes—II. An estimate of the efficiency of gas evolution on the basis of bubble growth data”. In: *Electrochimica acta* 29.2 (1984), pp. 175–180.

[61] Helmut Vogt. “The rate of gas evolution of electrodes—I. An estimate of the efficiency of gas evolution from the supersaturation of electrolyte adjacent to a gas-evolving electrode”. In: *Electrochimica acta* 29.2 (1984), pp. 167–173.

[62] Cheng-Chien Wang, Chuh-Yung Chen, et al. “Water electrolysis in the presence of an ultrasonic field”. In: *Electrochimica Acta* 54.15 (2009), pp. 3877–3883.

[63] Ruben Wedin and Anders A Dahlkild. “On the transport of small bubbles under developing channel flow in a buoyant gas-evolving electrochemical cell”. In: *Industrial & engineering chemistry research* 40.23 (2001), pp. 5228–5233.

[64] T Weier and S Landgraf. “The two-phase flow at gas-evolving electrodes: bubble-driven and Lorentz-force-driven convection”. In: *The European Physical Journal Special Topics* 220.1 (2013), pp. 313–322.

[65] A Zarghami, NG Deen, and AW Vreman. “CFD modeling of multiphase flow in an alkaline water electrolyzer”. In: *Chemical Engineering Science* 227 (2020), p. 115926.

[66] Kai Zeng and Dongke Zhang. “Recent progress in alkaline water electrolysis for hydrogen production and applications”. In: *Progress in energy and combustion science* 36.3 (2010), pp. 307–326.

[67] Dongke Zhang and Kai Zeng. “Evaluating the behavior of electrolytic gas bubbles and their effect on the cell voltage in alkaline water electrolysis”. In: *Industrial & Engineering Chemistry Research* 51.42 (2012), pp. 13825–13832.